

Tailoring thermal properties of functional materials

Thèse N° 9143

Présentée le 15 février 2019

à la Faculté des sciences de base

Laboratoire de physique de la matière complexe

Programme doctoral en physique

pour l'obtention du grade de Docteur ès Sciences

par

XAVIER FRANÇOIS METTAN

Acceptée sur proposition du jury

Prof. C. Hébert, présidente du jury

Prof. L. Forró, directeur de thèse

Prof. S. Hébert, rapporteuse

Dr O. S. Barišić, rapporteur

Prof. V. Tileli, rapporteuse

2019

To Pauline and Sarah
and to Elina

“J’aime les panoramas. Celui-ci est magnifique.”

— Hubert Bonisseur de La Bath (Jean Dujardin) in *OSS 117 : le Caire, nid d’espions*

Acknowledgements

The preparation and achievements of my PhD Thesis would not have been possible without the valued contributions of many people. First, I feel a sense of sincere gratitude towards my supervisor Prof. Forró for welcoming me in his Group and trusting me all along my PhD and before. His vision and open-mindedness have prompted very stimulating and interesting research.

I have to give a special mention to Dr. Jaćimović, Dr. Pisoni and Dr. Gaal, because they welcomed me warmly when I joined LPMC and taught me many of the secrets of the transport labs. I still use to be nostalgic about this “good old times”, and I hope we will be able to collaborate again in a near future. I am also very grateful to Dr. Horvath, who always encouraged me to be curious, and who was a real *motivator*.

I sincerely appreciated the support, useful discussions and *easy* debriefings with my colleagues from LPMC and neighbours: Péter M., Péter S., Balint, Edoardo, Pavao, Luka, Konstantin M, Konstantin S, Lidia, Andrea, Gaëtan, Endre, Trpimir, Anastasiia, Iness, Eric, Massimo, Samy, Sergiy, Raphaël, Davor, Maryam M., Marton, Dunja, Milica, Alex. Learning from the experience and (not only scientific) advice of “seniors” was highly rewarding and motivational and for that I would like to thank Prof. Pavuna, Prof. Mila, Dr. Zivkovic, Dr. Magrez, Prof. Holzcer, Dr. Grimaldi, Dr. Sienkiewicz., Dr. Arakcheeva, Dr. Babcsan, Prof. Kaptay, Dr. O. Barišić and Prof. N. Barišić.

The experimental achievements would not have been possible without the technical and proficient help I received from: the staff of CMI, the electronicians, the IT intervention team, in particular Baptiste, and the staff from the mechanical workshop, in particular Gilles, Daniel, Claude, Adrien et Gérald. I sincerely thank Nicole, Anh and Evelyn for their help with the administrative work, and for their kindness.

As I probably learnt more from the students I supervised than they could learn from me: thanks to Becky, Samuel, Maryam, Coralie and Morgan.

In addition, I would like to thank the members of the jury of my Thesis: Dr. O. Barišić, Prof. V. Tileli, Prof. S. Hébert and Prof. C. Hébert.

The last four years would have been very different without the great times spent together with the “team Planta”. I am very grateful towards Jérôme, Valentin, Gaëlle, Sébastien, Marie, Bertrand, Jérémie, Fred, Maïk not only for never blaming me for my long stays away from Valais, but also for constantly heartening me. I also had great times with my “old” mates from EPFL: Thibaud, Csaba, Luca, Zeno, Clément, Freya: I wish them all bright careers as

Acknowledgements

physicists. Because playing the violin with friends became more and more important as I was navigating through my thesis, I owe huge thanks to my musician fellows, who faced many wrong notes and sharp criticism from me: the talented pianists, the OChE's members and friends, in particular Giuseppe, Florian, Nicolas, Thomas, Lila, Isabelle, Lucien and Francesca.

Finally, I would like to warmly thank my Family for their encouragements. It always felt wonderful to spend a moment in Sion in our warm home. I felt challenged by the recurrent questions on the essence of my PhD: I am grateful to my parents, sisters, aunts for their endless curiosity. Elina was the best lover and best friend, and I cannot imagine what these last years would have been without her and her unconditional support.

Lausanne, 16 December 2018

Xavier

Abstract

Thermal conductivity (κ) plays an essential role in functional devices. In some cases, high value is required to transfer heat efficiently. In others, low κ assists in maintaining a temperature gradient necessary for device operation. It is profitable to design materials where one can tune κ in a broad range according to its function. Beyond functionality, κ is a fundamental property of matter, and a fantastic probe to assess vibrational dynamics and electronic structure in condensed matter. In conjunction with other transport properties such as electrical resistivity and thermoelectric power, κ promotes a deeper understanding of the electronic and vibrational structure of materials.

In the present Thesis, careful experimental determination of the transport coefficients of a variety of systems over a broad temperature range (4 – 300 K) let me unveil subtle interactions between phonons and/or electrons. The insights gained from an accurate interpretation of these properties empowers us to engineer and fine-tune the functionality of materials for applications.

I first investigate the thermoelectric properties of nickel-based high-entropy alloys (HEAs), believed to host unconventional effects arising from the high level of site-disorder in their crystalline structure. Anomalous resistivity with a low temperature coefficient validates the disordered nature of HEAs. The Seebeck coefficient, reported for the first time for HEAs, is surprisingly low. In the quest to understand transport in HEA, I have discovered that iron-nickel alloys exhibit a promising thermoelectric figure of merit (ZT) of 0.1 at room temperature.

One way to further increase ZT is to decrease κ (in FeNi alloys or other materials) is by texturing the material. Aluminium foams are systems of choice to observe the effect of a modified structure on the thermoelectric properties. Tailoring of the bubbles' size is demonstrated by applying an external acoustic force in the foaming process. Moreover, the influence of the macro- and micro- structure of the foams on thermoelectric properties is discussed.

The best example for tuning κ by texturing is anatase titanium dioxide (TiO_2). κ was varied over three orders of magnitude by adjusting its oxygen contents and by texturing it into a foam, aerogel-like structure. I identified a new, strong diffusion mechanism of heat by polarons, created as a consequence of oxygen vacancies. Furthermore, anatase nanowires organized into foams result in an unprecedented low $\kappa = 0.014 \text{ W/Km}$ at room-temperature. Doping this anatase foam heralds promising applications, in particular in thermoelectricity.

An oxide which has an intrinsically nanoporous structure reminding that of a foam, is

Acknowledgements

Mayenite ($\text{Ca}_{12}\text{Al}_{14}\text{O}_{33}$). The thermal conductivity of such system is verified to be intrinsically low. The peculiar cage structure could host atomic or molecular species to tune its electrical conductivity, with bright prospects for thermoelectric applications.

Finally, the thermoelectric properties of hybrid halide perovskites, cheap and easy-to-synthesise compounds, were studied. Three materials of this family have ultra-low κ , due to the vibrational degrees of freedom of their organic cations. Notably, a tin-based organic-inorganic compound delivers $ZT = 0.13$ at room temperature. The thermoelectric conversion efficiency of this material was measured directly and is believed to yield promising thermoelectric applications.

Keywords Thermal conductivity, transport coefficients, thermoelectricity, metallic alloys, metal foams, titanium dioxide, oxygen vacancies, nanowires, perovskites, phonon scattering.

Résumé

Concevoir des matériaux pour lesquels la conductivité thermique (κ) peut être contrôlée dans une large mesure a de nombreux avantages car κ occupe un rôle essentiel dans les dispositifs fonctionnels. D'une part, des valeurs élevées sont requises pour évacuer la chaleur de manière efficace ; d'autre part, une faible conductivité thermique aide à maintenir la différence de température nécessaire au bon fonctionnement de certains dispositifs. Au-delà de son utilité fonctionnelle, κ est une propriété fondamentale de la matière et un excellent outil pour comprendre la dynamique vibrationnelle et la structure électronique de la matière condensée. Combinée à d'autres propriétés de transport comme la résistivité ou le pouvoir thermoélectrique, κ permet une compréhension plus approfondie de la structure électronique et vibrationnelle des matériaux.

Dans cette Thèse, la détermination expérimentale minutieuse des coefficients de transport dans une large gamme de températures (4 – 300 K) permet de dévoiler de subtiles interactions entre phonons et/ou électrons. De leur interprétation résulte une compréhension qui donne des clés pour ajuster précisément la fonctionnalité des matériaux en vue de leurs applications.

Des alliages à haute entropie (HEAs) sont pressentis pour abriter des phénomènes non-conventionnels, en vue du degré élevé de désordre de sites dans leur structure cristalline. On a en effet validé que leur résistivité anormale, liée à un faible coefficient de température, provient du désordre. Leur pouvoir thermoélectrique, reporté pour la première fois, est étonnamment bas. Dans ma recherche pour comprendre les phénomènes de transport dans les HEAs, j'ai découvert que des alliages fer-nickel (FeNi) exhibent un facteur de qualité thermoélectrique (ZT) très encourageant de 0.1 à température ambiante.

Une manière d'élever ZT consiste à réduire κ (pour le FeNi ou d'autres matériaux) en modifiant la texture d'un matériau. Les mousses d'aluminium sont un système de choix pour observer les effets de telles modifications sur les propriétés thermoélectriques. Le contrôle de la taille des bulles est rendu possible grâce à l'application d'une force acoustique lors du processus de création de la mousse. En outre, l'influence de la micro- et macro- structure des mousses sur leurs propriétés thermoélectriques est analysée.

Le meilleur exemple de régulation de κ suite à un changement de texture est l'anatase de dioxyde de titane (TiO_2). κ a été modulé sur trois ordres de grandeurs grâce à la variation du contenu en oxygène et au sculptage en forme de mousse, similaire à un aérogel. J'ai identifié un nouveau mécanisme de forte diffusion de la chaleur par des polarons, provenant des

Acknowledgements

lacunes d'oxygène. D'autre part, des nanofils d'anatase arrangés en mousse ont donné lieu à une conductivité thermique de 0.014 W/Km à température ambiante, une valeur très basse sans précédent. Un dopage chimique de cette mousse d'anatase pourrait donner lieu à des applications prometteuses, en particulier en thermoélectricité.

Un oxyde à la structure nanoporeuse rappelant celle d'une mousse est la mayenite ($\text{Ca}_{12}\text{Al}_{14}\text{O}_{33}$). La conductivité thermique intrinsèquement basse d'un tel système est vérifiée par nos mesures. La structure particulière en forme de cage pourrait accueillir des espèces atomiques ou moléculaires dans le but d'ajuster la conductivité électrique, avec des applications attrayantes pour la thermoélectricité.

Finalement, les propriétés thermoélectriques de perovskites hybrides, des composés peu coûteux et faciles à synthétiser, ont été étudiées. Trois matériaux de cette famille ont des valeurs de κ ultra basses, provenant de degrés de libertés rotationnels de leurs cations organiques. De manière notable, le composé organique-inorganique à base d'étain donne $ZT = 0.13$ à température ambiante. L'efficacité de conversion thermoélectrique de ce matériau a en outre été mesurée de manière directe et implique des applications séduisantes en thermoélectricité.

Mots-clés Conductivité thermique, coefficients de transport, thermoélectricité, alliages métalliques, mousses métalliques, dioxyde de titane, lacunes d'oxygène, nanofils, perovskites, diffusion de phonons.

Contents

Acknowledgements	iii
Abstract	v
Résumé	vii
List of figures	xiv
List of tables	xv
Notation	xvii
Introduction	1
1 Transport coefficients in condensed matter	5
1.1 Theory of transport	5
1.1.1 Phenomenological equations	5
1.1.2 Boltzmann equations	6
1.1.3 Electrons	7
Wiedemann-Franz law	9
Electrical conductivity in metals	9
Matthiessen's rule	10
Bloch-Grüneisen formula for electrons	10
1.1.4 Seebeck coefficient	10
Mott's formula	11
1.1.5 Thermal conductivity	12
Peierls-Boltzmann transport equation	12
The Callaway formula	13
Extensions of the Callaway formula	14
1.2 Thermoelectricity	14
1.2.1 Thermoelectric generator	14
1.2.2 Thermoelectric figure of merit	15
1.2.3 Strategies to optimise ZT	17
Minimising the lattice thermal conductivity	17
Maximising the power factor	18

Contents

2	Transport in selected high-entropy alloys	19
2.1	High-entropy alloys	19
2.1.1	Synthesis of high-entropy alloys	20
2.2	Thermoelectric properties	21
2.3	FeNi alloys	25
2.4	Conclusions	29
3	Charge and heat transport in metal foams	31
3.1	Metal foams	31
3.2	Aluminium foams	32
3.2.1	Preparation of the foams	33
3.2.2	Control of the bubble's size	35
	Formation of a gas bubble	35
	Acoustic pressure	36
	Experimental realisation	37
3.3	Microstructure	40
3.4	Transport properties	43
3.4.1	Electrical and thermal conductivities	43
3.4.2	Seebeck coefficient	45
3.4.3	Effect of the porosity	46
3.5	Conclusions	46
4	Heat transport in functional oxides	49
4.1	Titanium dioxide	49
4.2	Anatase single-crystals	51
4.2.1	Synthesis	51
4.2.2	Oxygen vacancies	51
4.3	Thermal conductivity	54
4.3.1	Low intrinsic thermal conductivity	54
4.3.2	Polaronic defects coupled to crystalline phonons	56
4.3.3	Phonon scattering on polaronic defects	58
4.3.4	Dynamical phonon scattering in anatase titanium dioxide	60
4.4	Chemical doping with fluorine	60
4.5	Anatase foams and nanoparticles	62
4.5.1	Thermal conductivity of anatase foams and nanoparticles	63
4.6	Mayenite	65
4.6.1	Electronic properties	65
4.6.2	Electrical resistivity	66
4.6.3	Thermal conductivity	67
4.7	Conclusions	69

5 Thermoelectricity in hybrid-halide perovskites	71
5.1 Organic-inorganic metallic perovskites	71
5.1.1 Highly tunable structures	72
5.1.2 Beyond photovoltaic technologies	73
5.2 Thermoelectric properties	74
5.2.1 Electrical resistivity	74
5.2.2 Seebeck coefficient	75
5.2.3 Thermal transport	76
5.2.4 Thermoelectric figure of merit	78
5.2.5 Improving the thermoelectric figure of merit	79
5.3 Tin-based thermoelectric devices	80
5.3.1 Thermoelectric conversion efficiency	81
5.3.2 Preparation of the samples	81
5.3.3 Charge injection engineering	83
5.3.4 Energy-conversion efficiency	84
5.4 Conclusions	86
General conclusions and outlook	89
A Experimental methods	91
A.1 Control of the temperature	91
A.2 Transport coefficients	91
A.2.1 Resistance	91
A.2.2 Seebeck coefficient	93
A.2.3 Thermal conductivity	93
A.3 Thermoelectric devices	94
A.3.1 Engineering values	94
A.3.2 Correction factor	95
B Apparent surface tension at interfaces with solid particles	97
B.1 Spherical particles	98
B.2 Solid particles at a liquid-solid interface	99
Bibliography	119
Curriculum Vitae	121

List of Figures

1	From superinsulators to ultra-high thermal conductors	2
2	From single crystal to glass	3
1.1	Sample geometry	6
1.2	Influence of the density of state on thermopower	11
1.3	Thermoelectric generator (TEG)	15
1.4	Materials realising high ZT	16
1.5	Assessing thermoelectrics	17
2.1	Resistivity of Ni-based high-entropy alloys	21
2.2	Temperature coefficient of Ni-based high-entropy alloys	22
2.3	Thermopower of Ni-based high-entropy alloys	23
2.4	Thermal conductivity of NiFeCrCoCuAl _{0.5} Ti _{0.2}	24
2.5	Thermopower of FeNi alloys	25
2.6	Resistivity of FeNi alloys	26
2.7	Curie temperature and residual resistivity of FeNi alloys	27
2.8	Power factor of FeNi alloys	28
2.9	Thermal conductivity of two FeNi alloys	28
2.10	Thermoelectric figure of merit of two FeNi alloys	29
3.1	Experimental setup for foaming	36
3.2	Bubble diameter in Duralcan controlled by ultrasonic power	39
3.3	Foaming experiment	39
3.4	Microstructure and composition	41
3.5	X-ray diffraction patterns of aluminium foams	42
3.6	Electrical resistivity of aluminium foams	43
3.7	Thermal conductivity of aluminium foams	44
3.8	Thermoelectric power of aluminium foams	45
4.1	Polymorphs of titanium dioxide	50
4.2	Resistivity of conducting anatase TiO ₂	52
4.3	Defects in anatase single-crystals measured by ESR	53
4.4	Thermal conductivity of anatase TiO ₂ single-crystals	54
4.5	Fitting thermal conductivity of anatase with and without resonant scattering	56
4.6	Thermal and electrical conductivity of F-doped anatase TiO ₂	61

List of Figures

4.7	Thermoelectric power of F-doped anatase TiO_2	61
4.8	Anatase foams and nanoparticles	62
4.9	Thermal conductivity of anatase TiO_2 foams and nanoparticles	64
4.10	Crystal structure of mayenite	65
4.11	Schematic electronic structure of mayenite	66
4.12	Resistivity of mayenite single-crystals	67
4.13	Thermal conductivity of mayenite single-crystals	68
4.14	Tuning thermal conductivity of anatase TiO_2	70
5.1	Crystal structure of MAPbI_3 and layered-solar-cell architecture	72
5.2	Examples of organo-metallic perovskites	73
5.3	Electrical resistivity	75
5.4	Seebeck coefficient and thermal conductivity	76
5.5	Evolution of ZT	78
5.6	MASnI_3 -thermoelectric device and experimental setup	80
5.7	j - V characterisation of a thermoelectric device	82
5.8	Influence of pressure on the properties of a MASnI_3 pellet	83
5.9	Influence of ageing on the resistivity of a MASnI_3 pellet	83
5.10	Charge injection engineering	84
5.11	Thermoelectric properties of MASnI_3 devices	85
A.1	Experimental configuration for measurements of thermoelectric properties . .	92
A.2	Specimen prepared for a measurement of the thermal conductivity	93
A.3	Calibration of the heat current	96
B.1	Surface coverage of particles in a liquid	97
B.2	Apparent surface tension as a function of the contact angle	99

List of Tables

3.1	Physical properties of aluminium alloys	32
3.2	Production of metal foams	34
3.3	Composition and structure of aluminium foams	42
4.1	Model parameters for resonant dynamical scattering in anatase TiO_2	55
4.2	Model parameters for the thermal conductivity of mayenite	68
5.1	Model parameters for the thermal conductivity of MAPbI_3 and MAPbBr_3	77

Notation

The *standard* pressure and temperature conditions correspond to atmospheric pressure (1 Bar) and room temperature (20 °C).

Characterisation techniques

AFM	Atomic force microscopy (or microscope)
XRD	X-ray Diffraction
SEM	Scanning electron microscope
TEM	Tunneling electron microscope
EDX	Energy-dispersive X-ray spectroscopy

Materials

HEA(s)	High-entropy alloy(s)
MMC	Metal-matrix composite

Transport

σ	Electrical conductivity
ρ	Electrical resistivity
S	Seebeck coefficient or thermopower
κ	Total thermal conductivity
κ_{el}	Electronic contribution to the thermal conductivity
κ_{ph}	Lattice thermal conductivity
TE	Thermoelectric
TEG	Thermoelectric generator
ZT	Thermoelectric figure of merit
$(ZT)_{\text{eng}}$	Engineering figure of merit
k_B	Boltzmann constant
\hbar	Reduced Planck constant
η_c	Carnot efficiency

Miscellaneous

RT	Room temperature (20 °C)
UHV	Ultra-high vacuum ($p < 10^{-6}$ Torr)
ML	Monolayer
SC	Single crystal
VRH	Variable-range hopping
WFL	Wiedemann-Franz law

Introduction

Amongst the most challenging issues of our times is global warming which has already been in the focus of both political and scientific communities for several decades. In a broader picture, since the Industrial Revolution in the nineteenth century an ever-increasing consumption of natural resources for energy production has triggered a dramatic climate change threatening life on Earth. Hence there is an urge to find innovative, environmentally-friendly technologies to tackle the energy problem. Enhancing the harvesting, conversion, storage and distribution of energy should allow mankind to completely abandon non-renewable and polluting processes in the long run.[1]

In this chain of harvesting, conversion, storage and distribution, physics can contribute a lot since all are based on physical principles. Solar, nuclear, thermal, wind, chemical or kinetic powers, their conversion into mechanical or electrical energy, their storage by capacitor, super capacitor or batteries, their transmission by conducting wires or wirelessly by electromagnetic waves, etc. – all these themes represent challenges. In my PhD I have addressed a weak spot in the energy conversion, that is the energy loss in form of heat. This is a very serious issue, since on the one hand it heats up the environment and on the other hand, due to these losses, the primary energy sources are not used efficiently. For example, in the case of internal-combustion engines, only 25% of the chemical energy is converted into mechanical energy. Probably not to the same extent, but in nuclear power plants there are serious thermal losses as well. The task of a physicist could be here to find functional materials which isolate the system (not to radiate heat into the environment) and to use this thermal energy to convert it into electrical power. The materials which are good thermal insulator, either intrinsically or owing to their texture (e.g. foams) are of prime importance. The quantity characterising this property of a material is called thermal conductivity (κ), and it varies over a broad range (see Fig. 1).

The engine which can transform heat into electricity is the thermoelectric generator. The essential part of it are thermoelectric materials, which in a temperature gradient (difference between a hot and cold end) create electrical current in a circuit. The combination of three fundamental quantities enables us to assess the quality of thermoelectric materials in this energy conversion: the electrical conductivity, thermal conductivity and Seebeck coefficient (the three *transport coefficients*). While electrical and thermal conductivities reflect how well electricity (electric charges) and heat propagate through a medium, the Seebeck coefficient

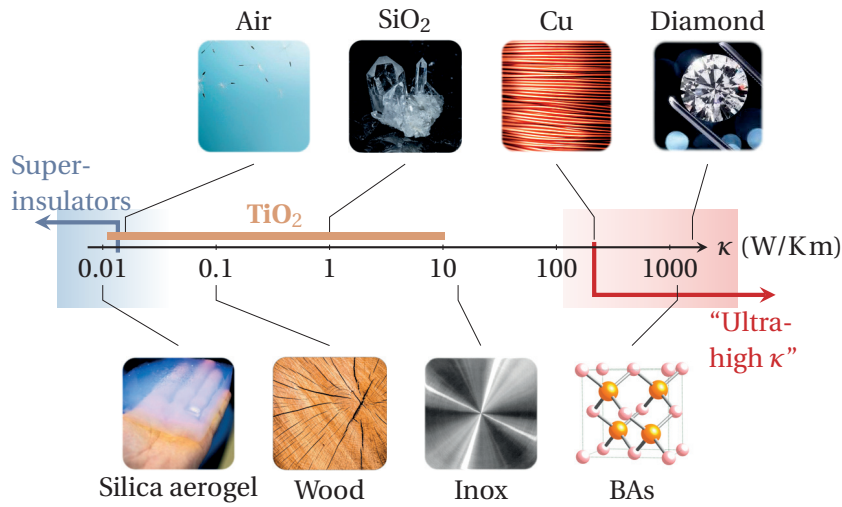


Figure 1 – Examples of materials spanning the whole scale of thermal conductivities, from superinsulators to “ultra-high” thermal conductors. Our work focuses on materials situated in the left side of this scale. Notably, the thermal conductivity of TiO₂, upon tuning its concentration of oxygen vacancies and texturing the material, could be varied over three orders of magnitude.

accounts for the intensity of the thermoelectric effect. Effective thermoelectric materials prove a compromise between these three quantities; admittedly, the Seebeck coefficient must be maximal, together with the electrical conductivity, whereas the thermal conductivity has to be minimised.[2] This last requirement joins the two strategies: thermal insulation and thermal generators.

The transport coefficients are not only relevant to thermoelectric materials. In fact, they are great tools for physicists to gain deeper understanding of the fundamental mechanisms governing properties of condensed matter. In particular, understanding electronic, magnetic and vibrational properties, and their mutual interactions is the key to synthesise and engineer novel functional materials. From the three transport coefficient, the thermal conductivity (κ) is especially in the focus of this Thesis.

Active and passive thermal management play a critical role in nearly every sector of engineering sciences. Alongside with developing strategies to optimise heat transfer in various devices, understanding and tuning the intrinsic ability of a material to propagate heat is an important issue. Materials with high thermal conductivities (κ) are sought for their capacity to transfer heat swiftly and evenly. Electronic packaging is one of the most important examples where the temperature of a circuit has to be limited to avoid overheating.[3–8] Mediums with high κ are also required in cars, rocket engines, or nuclear reactors, where heat has to be evacuated efficiently to prevent hazardous failure of the mechanical parts.[9–11] Conversely, other applications demand thermally insulating materials. Compounds with low values of κ (< 0.1 W/Km) are employed to prevent severe heat losses in buildings, heat pumps, car engines and power plants.[3] Moreover, thermal conductivity is one of the key parameters ruling the conversion of energy in thermoelectric materials.[2] Figure 1 illustrates the wide

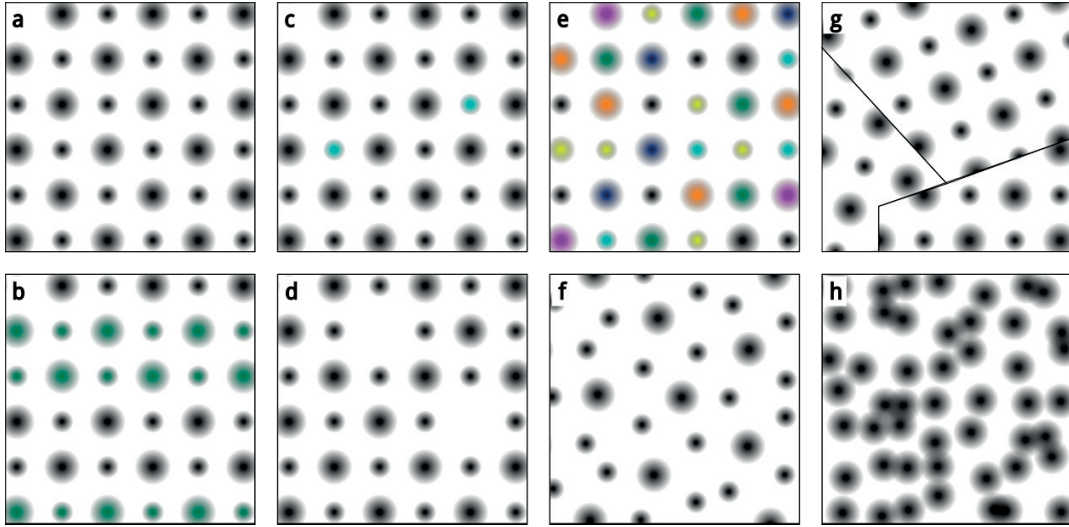


Figure 2 – From single crystal to glass. **a** Array of atoms perfectly ordered in two dimensions. Different types of disorder: **b** inclusions/heterostructure with two materials, **c** chemical doping of a single crystal or dilute alloying, **d** vacancies in the crystal structure, **e** multiple principal components alloying, **f** quasi crystal, **g** domain walls or grain boundaries or dislocations, and **h** amorphous matter.

range of thermal conductivities, from superinsulators to “ultra-high κ ” materials.

Tailoring thermal properties of functional materials

Throughout this Thesis, materials with versatile *structures* and *textures* are considered with very strong influences on their thermal properties. Here, the term “structure” encompasses notions of crystalline structure, electronic structure, nano, micro and macro structure. The schemes on Figure 2 present archetypal examples of different “structures” at the atomic level, from perfect crystalline lattice to amorphous matter.

I explore the thermo-electric properties of versatile systems by taking advantage of very accurate and sensitive measurement techniques, over a broad temperature range, from 3 to 850 K. The temperature-dependent quantities allows one, thanks to theoretical considerations and modelling, to better understand phenomena governing the functionality of these systems. In Chapter 1, the concepts used to describe the materials under consideration are exposed. Moreover, the frame to address thermoelectric conversion is given and discussed.

In Chapter 2, I first investigate the thermoelectric properties of nickel-based high-entropy alloys (HEAs), a system believed to host unconventional effects arising from the high level of disorder. The large entropy of mixing of its multiple principle elements (sketched on Fig. 2e) – in opposition to metallic alloys (Fig. 2c), where only one or two elements compose the major part of their atomic composition – entail local deformations of the lattice, an arrangement that could stimulate interesting phenomena. The hope to observe the mixing entropy translated to electronic entropy prompted evaluation of the Seebeck coefficient. I report it for the first

time for HEAs. In the quest to understand transport in HEA, my interest has been attracted by iron-nickel alloys. They are found to exhibit unexpected, very promising performance for thermoelectricity.

With the intention of tuning the thermoelectric properties of materials by texturing them, the thermoelectric properties of aluminium foams are investigated in Chapter 3. First I demonstrate a powerful yet simple technique to tailor the geometry of the foam. Second, the influence of the macro- and micro- structure of the foams on thermoelectric properties is discussed.

Keeping in mind that controlling the texture of a material can be the key to enhance its thermoelectric conversion efficiency, in Chapter 4 I reverse the strategy, inspecting the properties of mayenite, an oxide with an inherent-nanoporous structure. Looking for other materials with a simple composition, I report the thermal conductivity of anatase titanium dioxide (TiO_2) for the first time. Additionally and importantly, two paths to adjust thermal conductivity of this compound used in many applications are explained. First the crucial role of oxygen vacancies (Fig. 2d) or substitutional doping (Fig. 2c) is unveiled. Second, the strong effect of texturing the material into foams is assessed.

In the last Chapter, hybrid-halide perovskites – the compounds known for their applications in photovoltaics[12] – are the center of attention. Following a favourable forecast regarding their applications as thermoelectric generators,[13] I examine their interesting thermoelectric properties. In order to assess the real thermoelectric conversion efficiency of MASnI_3 , I present an experimental setup for their characterisation and discuss ways of easily improving their thermoelectric properties.

At the end, one could be under the impression that thermal conductivity is a simple quantity, easy to measure and straightforward to interpret. It is not at all the case: one has to employ extreme care in setting up the experiments, and to be very, very patient – a measurement of the whole temperature dependence usually takes days or even a week. On a personal note, I can say that it was worth the investment: I could address materials which nobody did before and I could explore my creativity.

1 Transport coefficients in condensed matter

1.1 Theory of transport

The study of *transport* phenomena is at the heart of understanding the complex behaviour of correlated systems. *Transport* phenomena regroup “any of the phenomena involving the movement of various entities, such as mass, momentum, or energy, through a medium, fluid or solid, by virtue of non-uniform conditions existing within the medium.”[14] This eventually applies for energy transfer in condensed matter, in the form of electrical charge and heat. In this section, the theoretical frame to study such phenomena is recalled. Important laws underlying the thermo-electric coefficients are explained. First, from a thermodynamics point of view, the phenomenological equations for heat and charge currents are recalled. The next sections are largely inspired and based on the works of Refs. 15, 16, 17, 18 and 19.

1.1.1 Phenomenological equations

At a macroscopic scale, transport stems from external forces driving irreversible currents (of heat, charge, mass, ...). In general, these forces can be related to currents from the first and second laws of thermodynamics.[20] Here, only small deviations to equilibrium-state are considered, so that the relations between forces and currents are linear.

The laws of thermodynamics can help us understanding important concepts related to transport, for macroscopic systems. Regarding charge and heat transport, one has to consider an electrical potential $\phi(\mathbf{r})$, where \mathbf{r} is a location in the system, and a temperature gradient ∇T , driving the system out of equilibrium. For small electric fields ($\mathbf{E} = -\nabla\phi$) and temperature gradients, conservation laws lead to equations for the energy currents. The current densities associated with charge transfer \mathbf{J} and with heat transfer \mathbf{Q} are related to the three transport coefficients σ , S and κ by the following relations:[16]

$$\mathbf{J}(\mathbf{r}) = \sigma (\mathbf{E} - S \nabla T) \tag{1.1a}$$

$$\mathbf{Q}(\mathbf{r}) = ST \cdot \mathbf{J}(\mathbf{r}) - \kappa \nabla T \tag{1.1b}$$

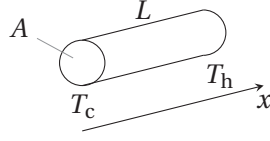


Figure 1.1 – Scheme of a simple geometry of the sample, of length L and constant cross-section A . In this case, the transport is measured along the x -axis, when a temperature difference $\Delta T = T_h - T_c$ is applied across the specimen.

In this set of equations, the coefficients σ , S and κ correspond to physical (measurable) quantities. In open-circuit conditions ($\mathbf{J} = 0$), one can observe that an electric field is proportional to the temperature gradient, and that the heat current \mathbf{Q} is proportional to the temperature gradient. Considering a homogeneous specimen with a temperature gradient along one dimension (as in Figure 1.1, $\nabla T = \frac{\Delta T}{L}$, $J(x) = J$ and $Q(x) = Q$) gives the intuition on how to probe experimentally the transport coefficients. Indeed, in absence of temperature gradients on the specimen, one can obtain the *electrical conductivity* σ from Equation (1.1a), which reduces to Ohm's law, $i = \sigma \cdot \Delta V$, where $i = LJ$ is the electrical current, and $V = LE$ the potential difference accross the sample of length L . When $i = 0$ and a finite temperature difference ΔT is applied across the sample of constant cross-section A , the *Seebeck coefficient* S and the *thermal conductivity* κ can be determined as follow:

$$S = \frac{\Delta V}{\Delta T} \quad (1.2)$$

$$\kappa = -\frac{LQ}{\Delta T}. \quad (1.3)$$

The former equation describes the Seebeck effect, and the latter is known as Fourier's law. Figure 1.1, Ohm's law and Equations 1.2 and 1.3 present the basic geometry and effects enabling experimental determination of the thermoelectric coefficients. More details about experimental determination of the transport coefficients is given in Appendix A.

Equations (1.1a) and (1.1b) are established from thermodynamic considérations and they provide a strong frame to study thermo-electric phenomena, but do not tell about the microscopic origin of the phenomena. In the next section, we introduce the Boltzmann equation, that sets a strong theoretical background for transport in condensed matter.

1.1.2 Boltzmann equations

Before the discovery of quantum mechanics, a microscopic, probabilistic theory was developed to account for transport coefficients in metals and semiconductors. Indeed the kinetic Drude theory and the Drude-Sommerfeld model failed to properly describe the transport of electrons. The semi-classical Boltzmann equation applies to different system, but at its core lies a distribution-density function of (quasi)particles. It can be, for example, the distribution density of electrons in a material, or the distribution density of phonons. To start with, we assume coarse-grained materials, with the “grain” at position \mathbf{r} sufficiently small but of finite

volume. Let the function $f(\mathbf{r}, \mathbf{k}, t)$ be the distribution density of a wave packet of momentum \mathbf{k} at position \mathbf{r} . Then the quantity $f(\mathbf{r}, \mathbf{k}, t) \frac{d^3r d^3k}{(2\pi)^3}$ is the amount of particles with wavevectors \mathbf{k} within d^3k at time t , at position \mathbf{r} . The generic Boltzmann equation is a balance equation and reads:

$$\frac{df}{dt} = \left. \frac{\partial f}{\partial t} \right|_{\text{drift}} + \left. \frac{\partial f}{\partial t} \right|_{\text{diff}} + \left. \frac{\partial f}{\partial t} \right|_{\text{coll}}, \quad (1.4)$$

where the “drift” term corresponds to a the drift caused by external forces, the “diff” term to diffusion of particles and the collision (“coll”) term accounts for scattering of the particles. In the steady-state, by definition, $\frac{\partial f}{\partial t} = 0$. A more explicit version of the Boltzmann equation of transport can be given, with $\mathbf{v}_{\mathbf{k}}$ the group velocity and \mathbf{F} the sum of external forces:

$$\mathbf{v}_{\mathbf{k}} \cdot \nabla_{\mathbf{r}} f + \frac{1}{\hbar} \mathbf{F} \cdot \nabla_{\mathbf{k}} f = \left. \frac{\partial f}{\partial t} \right|_{\text{coll}}. \quad (1.5)$$

Solutions of the Boltzmann equation are usually difficult to extract analytically, but approximations can be made to describe the collision term. In particular, the *time constant* approximation allows to obtain insightful results in some cases:

$$\left. \frac{\partial f}{\partial t} \right|_{\text{coll}} = \frac{1}{\tau(\mathbf{k})} (f(\mathbf{k}) - f^0(\mathbf{k})) \quad (1.6)$$

Here, $f^0(\mathbf{k})$ is the equilibrium distribution – i.e. that of the unperturbed system ($\mathbf{F} = 0$ and $\nabla T = 0$) – and $\tau(\mathbf{k})$ is a relaxation time of the collisions. In the next sections, general observations will be made on the Boltzmann equations for both electrons and phonons.

1.1.3 Electrons

In this section we consider the distribution of electrons $f(\mathbf{k})$ in a homogeneous material. In this case the equilibrium distribution function is the Fermi-Dirac function:

$$f^0(\epsilon_{\mathbf{k}}) = \frac{1}{\exp\left[\frac{\epsilon_{\mathbf{k}} - \mu}{k_B T}\right] + 1}, \quad (1.7)$$

where k_B is Boltzmann’s constant, $\epsilon_{\mathbf{k}}$ is the energy-dispersion relation and μ the chemical potential of the electrons. For a weak electric field \mathbf{E} ($\mathbf{F} = -e\mathbf{E}$) and a small thermal gradient ∇T , the left-hand terms of Eq. (1.5) can be linearised:

$$-\frac{e\mathbf{E}}{\hbar} \nabla_{\mathbf{k}} f(\mathbf{k}) + \mathbf{v}_{\mathbf{k}} \nabla_{\mathbf{r}} f(\mathbf{k}) \approx -e\mathbf{E} \cdot \mathbf{v}_{\mathbf{k}} \cdot \frac{\partial f^0}{\partial \epsilon_{\mathbf{k}}} + \mathbf{v}_{\mathbf{k}} \frac{\partial f^0}{\partial T} \nabla T = \mathbf{v}_{\mathbf{k}} \left(-\frac{\partial f^0}{\partial \epsilon_{\mathbf{k}}} \right) \cdot \left(e\mathbf{E} - \frac{\epsilon_{\mathbf{k}} - \mu}{T} \nabla T \right). \quad (1.8)$$

Under the relaxation-time approximation, Equation (1.5) simplifies to:

$$f(\mathbf{k}) = f^0(\mathbf{k}) + \tau(\mathbf{k}) \cdot \mathbf{v}_{\mathbf{k}} \cdot \left(-\frac{\partial f^0}{\partial \epsilon_{\mathbf{k}}} \right) \cdot \left(e\mathbf{E} + \frac{\epsilon_{\mathbf{k}} - \mu}{T} \nabla T \right) \quad (1.9)$$

which is the solution of the linearised Boltzmann equation for the distribution density of electrons in presence of a weak electrical potential and small temperature gradient. From this last equation, one can observe that the deviation of the equilibrium distribution function has two distinct contributions, one from the the electric field and one from the temperature gradient.

The charge and heat current can be written in terms of energy integrals involving the solution of Eq. (1.9):[15]

$$\mathbf{J} = \int \frac{d\mathbf{k}}{(2\pi)^3} e \mathbf{v}_{\mathbf{k}} f(\mathbf{k}) \quad (1.10)$$

$$\mathbf{Q} = \mathbf{J}^U - \mu \mathbf{J}^N = \int \frac{d\mathbf{k}}{(2\pi)^3} \mathbf{v}_{\mathbf{k}} (\epsilon_{\mathbf{k}} - \mu) f(\mathbf{k}). \quad (1.11)$$

By comparing Eq. (1.10) and (1.11) with Eq. (1.1a) and (1.1b) the transport coefficients σ , S and κ_{el} can be related to the distribution density:

$$\sigma = \frac{2e^2}{(2\pi)^3} \int d\mathbf{k} \cdot \mathbf{v}_{\mathbf{k}} \mathbf{v}_{\mathbf{k}} \cdot \tau(\mathbf{k}) \left(-\frac{\partial f^0}{\partial \epsilon_{\mathbf{k}}} \right) \quad (1.12)$$

$$\sigma S = \frac{e}{(2\pi)^3} \int d\mathbf{k} \cdot \mathbf{v}_{\mathbf{k}} \mathbf{v}_{\mathbf{k}} \cdot \tau(\mathbf{k}) \frac{\epsilon_{\mathbf{k}} - \mu}{T} \left(-\frac{\partial f^0}{\partial \epsilon_{\mathbf{k}}} \right) \quad (1.13)$$

$$\frac{\kappa_{\text{el}}}{T} = \frac{1}{(2\pi)^3} \int d\mathbf{k} \cdot \mathbf{v}_{\mathbf{k}} \mathbf{v}_{\mathbf{k}} \cdot \tau(\mathbf{k}) \frac{(\epsilon_{\mathbf{k}} - \mu)^2}{T^2} \left(-\frac{\partial f^0}{\partial \epsilon_{\mathbf{k}}} \right) \quad (1.14)$$

Here, one can observe that all the details of the physics are contained in the energy dispersion $\epsilon_{\mathbf{k}}$ ($\mathbf{v}_{\mathbf{k}} = \frac{1}{\hbar} \nabla_{\mathbf{k}} \epsilon_{\mathbf{k}}$) and the scattering time $\tau(\mathbf{k})$, and therefore the three transport coefficients are related to each others. At this point, it is useful to insist on the assumptions or conditions for these relations to hold. First, $\tau(\mathbf{k})$ accounts only for elastic collisions, that relax exponentially (relaxation-time approximation to solve the Boltzmann equation). This means that electron-electron interactions are not taken into account. Second, the body has been considered completely static, neglecting the effects of lattice vibrations.

At energies much lower than the Fermi energy, a Sommerfeld expansion enables us to transform the integrals in the last equations to development series in power of $\frac{k_B T}{\epsilon_F}$ (ϵ_F is the Fermi energy):

$$\sigma = \frac{2e^2}{h} \Phi(\epsilon_F) + \dots \quad (1.15)$$

$$\sigma S = \frac{2\pi^2 k_B e}{3h} k_B T \left. \frac{\partial \Phi(\epsilon_F)}{\partial \epsilon} \right|_{\epsilon=\epsilon_F} + \dots \quad (1.16)$$

$$\kappa_{\text{el}} = \frac{2\pi^2 k_B}{3h} k_B T \Phi(\epsilon_F) + \dots \quad (1.17)$$

Here, $\Phi(\epsilon) = \frac{\hbar}{2} g(\epsilon) \tau(\epsilon) \mathbf{v}_{\mathbf{k}} \mathbf{v}_{\mathbf{k}}$ and $g(\epsilon_{\mathbf{k}})$ is the electronic density of state. From these relations, it can be seen that the three transport coefficients in metals are intimately connected by $\Phi(\epsilon)$ at the Fermi level. In the next sections, explicit forms of these relations, known as the

Wiedemann-Franz law and the Mott formula will be reviewed.

Wiedemann-Franz law

Comparing $\Phi(\varepsilon_F)$ in Equations (1.15) and (1.17), one obtains a simple proportionality relation between σ and κ_{el} :

$$\kappa_{el} = \frac{\pi^2}{3} \left(\frac{k_B}{e} \right)^2 T \sigma. \quad (1.18)$$

This equation is known as the Wiedemann-Franz law (WFL). It implies that the ratio $\frac{\kappa_{el}}{\sigma T}$ is constant. This constant is often called the Sommerfeld value $L_0 = \frac{\pi^2}{3} \left(\frac{k_B}{e} \right)^2 = 2.44 \cdot 10^{-8} \text{ W}\Omega/\text{K}^2$. [21,22] This law is verified for several pure metals. In the previous derivation of the Boltzmann transport equation, neither electron-electron, electron-phonon interactions nor inelastic scattering have been taken into account, so that this law does not hold for many materials. [23] However, it can be useful to quantify the possible discrepancies by comparing L_0 with the Lorenz ratio L , defined as:

$$L = \frac{\rho \kappa}{T}. \quad (1.19)$$

For many materials, estimating κ_{el} from resistivity data using Eq. (1.18) proves very useful to compare the relative contribution of charge carriers in the total thermal conductivity.

Electrical conductivity in metals

The Boltzmann equation for electrons enables us to address the case of an isotropic metal in three dimensions explicitly. Here, $\mathbf{v}_k \mathbf{E} \mathbf{v}_k = v_k^2 \mathbf{E}/3$ and recalling Eq. (1.12), the electrical conductivity is

$$\sigma = \frac{2e^2}{3(2\pi)^3} \int d\mathbf{k} \cdot v_k^2 \cdot \tau(\mathbf{k}) \left(-\frac{df^0}{d\varepsilon_k} \right). \quad (1.20)$$

From this formula we can recover the Drude formula for an electron gas. For temperatures much smaller than the Fermi temperature, $-\frac{df^0}{d\varepsilon_k} \simeq \delta(\varepsilon_k - \varepsilon_F)$ and the integral in Eq. (1.20) is straightforward:

$$\sigma = \frac{2e^2}{3} \tau_F v_F^2 N(\varepsilon_F) = \frac{e^2 \tau_F n}{m^*}, \quad (1.21)$$

where, $N(\varepsilon_F)$ is the single-spin-electron density at the Fermi surface, m^* the carriers effective mass, v_F and τ_F the Fermi-velocity and relaxation-time, respectively.¹

¹We recalled $N(\varepsilon_F) = \int \frac{d\mathbf{k}}{(2\pi)^3} \delta(\varepsilon_{\mathbf{k}} - \varepsilon_F) = \frac{m^* k_F}{2\pi^2 \hbar^2}$ and $n = 2 \int \frac{d\mathbf{k}}{(2\pi)^3} \theta(\varepsilon_{\mathbf{k}} - \varepsilon_F) = \frac{k_F^3}{2\pi^2}$.

Matthiessen's rule

Matthiessen's rule states that the effect different sources i of scattering of electrons (and later phonons) add up independently (without interferences). For a scattering mechanism i with scattering times τ_i , the total scattering time is:

$$\tau^{-1} = \sum_i \tau_i^{-1}. \quad (1.22)$$

A situation where Matthiessen's rule applies is for metallic alloys, where an atomic percentage x of the principle metal is substituted with other metallic atoms. In this case, it was observed that the resistivity can be split in two contributions:

$$\rho = \rho_i(T) + \rho_0(x), \quad (1.23)$$

i.e. a temperature-independent resistivity due to scattering on impurities is always present and depends principally on the amount of impurities (x). Next to it, the “ideal” (to be understood as resistivity without impurities) resistivity is temperature dependent. This rule is valid if x is small, so that the impurities do not modify the lattice constants, electronic structure, etc. of the solid. For disordered binary alloys, $\rho_i(x) \propto x(1-x)$. However, when there is the creation of intermetallic phases, $\rho_i(x)$ can have minima at critical compositions x (e.g. $x = 0.25$). [24]

Bloch-Grüneisen formula for electrons

When the influence of electron-phonon interactions cannot be neglected, the Bloch-Grüneisen formula presents very good agreement with experimental data of metals and alloys. It can be derived from the Boltzmann equation, using variational techniques: [17]

$$\rho = \rho_0 + \alpha_{\text{el-ph}} \left(\frac{T}{\theta_D} \right)^5 \int_0^{\theta_D/T} \frac{x^5 e^x}{(e^x - 1)^2} dx, \quad (1.24)$$

where the two free parameters are $\alpha_{\text{el-ph}}$ an electron-phonon coupling parameter and θ_D the Debye temperature. ρ_0 the residual resistivity when the temperature tends to zero ($\rho_0 = \lim_{T \rightarrow 0} \rho(T)$). In the high temperature limit ($T \gg \theta_D$), the integrand can be simplified to x^3 thus $\rho - \rho_0 \propto \alpha_{\text{el-ph}} \frac{T}{\theta_D}$. On the contrary, when $T \ll \theta_D$, the value of the integral is a constant scalar so that $\rho - \rho_0 \propto \alpha_{\text{el-ph}} \left(\frac{T}{\theta_D} \right)^5$.

1.1.4 Seebeck coefficient

The Seebeck coefficient can be interpreted in two ways. First, as mentioned earlier in Equation (1.2), it is the proportionality factor between the built-in potential and the temperature

difference. Now, taking the entropy current $\mathbf{J}_S = \mathbf{Q}/T$ and Eq. 1.1b, one obtains:[15,25]

$$\mathbf{J}_S = S\mathbf{J} - \kappa \frac{\nabla T}{T}. \quad (1.25)$$

Thus the current of entropy has two contributions, one from the current of carriers and one from the thermal gradient. In absence of thermal gradients, $S = \mathbf{J}_S/\mathbf{J}$ is the ratio of the current of entropy and the (charge) carrier current, hence the alternative interpretation of S as the entropy per carrier.

Mott's formula

To assess the temperature dependence of S , an additional relation can be extracted from Eq. (1.15) and (1.16), by substituting $\Phi(\varepsilon_F)$:

$$S = \frac{\pi^2 k_B^2 T}{3e} \left. \frac{\partial \ln \sigma(\varepsilon)}{\partial \varepsilon} \right|_{\varepsilon=\varepsilon_F}, \quad (1.26)$$

where e is the charge of the electron, ε_F the Fermi energy and $\sigma(\varepsilon)$ the energy-dependent conductivity. Equation (1.26) is referred to as the Mott formula, and unveils the link between the Seebeck coefficient and the energy-dependent electrical conductivity.

Since $\sigma(\varepsilon) \propto g(\varepsilon)\tau(\varepsilon)$, with $g(\varepsilon)$ the electron-density of states, its derivative appearing in Equation (1.26) is the sum of two terms:

$$S = \frac{\pi^2 k_B^2 T}{3e} \left(\left. \frac{\partial \ln g(\varepsilon)}{\partial \varepsilon} \right|_{\varepsilon_F} + \left. \frac{\partial \ln \tau(\varepsilon)}{\partial \varepsilon} \right|_{\varepsilon_F} \right). \quad (1.27)$$

The first term tells us that the electron-density of state has a very important influence on S . Indeed, if $g(\varepsilon)$ strongly varies with ε or displays singularities, the position of the Fermi energy can completely modify S , e.g. by changing its magnitude or even its sign. This is illustrated on Figure 1.2. In other words, S is sensitive to any change in the g . In the particular case where τ does not depend on ε and $g(\varepsilon) \propto \varepsilon^{1/2}$ is the density of state of a free electron gas, S is inversely proportional to the Fermi energy ε_F :

$$S = \frac{\pi^2 k_B^2 T}{3e \varepsilon_F} \quad (1.28)$$

so that S/T should be temperature-independent for pure metals. In Equation (1.27), the second term can inform us about possible contributions of different scattering mechanism in

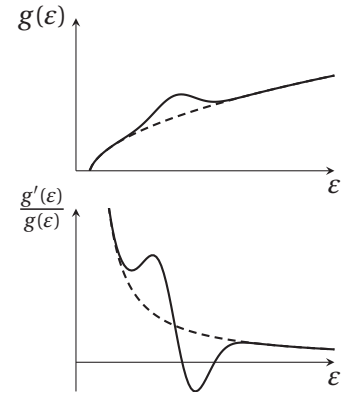


Figure 1.2 – Influence of the density of state on thermopower. When $g'(\varepsilon)$ crosses the x -axis, the thermopower changes sign. This happens when $g(\varepsilon)$ changes slope.

the thermopower, if they depend on ε .

For a conductor with independent groups of carriers p , with electrical conductivity σ_p and thermopower S_p (if the carrier were alone), the thermopower can be written as:

$$S = \frac{\sum_p \sigma_p S_p}{\sum_p \sigma_p}. \quad (1.29)$$

This formula is useful in the case of a two-band model, or when the same type of carriers have opposite spin (in a ferromagnet).

1.1.5 Thermal conductivity

We described in the last section how charge carriers can carry heat (κ_{el}). There, we omitted that vibrations of matter can propagate heat, adding their contribution to κ . We have addressed properties of the charge carriers: they have their own equilibrium wave-functions that are completely independent from other entities like phonons. Interactions between charge carriers and phonons are the result of transitions between unperturbed states.[19] As a result, the thermal conductivity κ is the sum of the different contributions, here of charge carriers and phonons, that can be treated independently:

$$\kappa = \kappa_{\text{el}} + \kappa_{\text{ph}}. \quad (1.30)$$

In this equation, κ_{ph} is the lattice thermal conductivity, or in other words the contribution of phonons to the total thermal conductivity. In this section, we will consider κ_{ph} only, for a dielectric material where $\mathbf{J} \approx 0$ ($\kappa_{\text{el}} \approx 0$).

Peierls-Boltzmann transport equation

For a dielectric crystal, the Boltzmann equation (1.4) can be applied with the phonon-mode distribution $n_j(\mathbf{q})$ of phonons with wave-vector \mathbf{q} in branch j :

$$\mathbf{v}_{\mathbf{q},j} \cdot \nabla T \frac{\partial n_j(\mathbf{q})}{\partial T} = \left. \frac{\partial n_j(\mathbf{q})}{\partial t} \right|_{\text{coll}} \quad (1.31)$$

where $\mathbf{v}_{\mathbf{q},j}$ is the phonon velocity.[26] Similarly to the case discussed for electrons, for small deviations from the equilibrium (small ∇T), the mode distribution can be linearised, i.e. $n_j(\mathbf{q}) = n_j^0(\mathbf{q}) + \delta n_j(\mathbf{q})$, where $n_j^0(\mathbf{q}) = v_j \left(\exp(\frac{\hbar \omega_{\mathbf{q}}}{k_B T}) - 1 \right)^{-1}$ is the Bose distribution, v_j is the degeneracy of branch j and $\delta n_j(\mathbf{q})$ the deviation proportional to ∇T . The solutions of Eq. (1.31) in this form are very complex and impossible to be solved analytically. The relaxation-time approximation can be used again here to obtain a simple solution (we omit the index j):

$$n(\mathbf{q}) \simeq n^0(\mathbf{q}) + \tau_{\mathbf{q}} \mathbf{v}_{\mathbf{q}} \frac{\partial n^0(\mathbf{q})}{\partial T} \cdot \nabla T, \quad (1.32)$$

where $\tau_{\mathbf{q}}$ is the time between scattering events of phonons with momentum \mathbf{q} . Since, in a kinetic picture of a gas of phonons a phonon with momentum \mathbf{q} in branch j contributes to the heat current \mathbf{Q} with $\hbar\omega_{\mathbf{q},j}\mathbf{v}_{\mathbf{q},j}n_j(\mathbf{q})$, the thermal conductivity can be written:

$$\kappa_{\text{ph}} = \sum_j \int_0^{\omega_m} \hbar\omega_{\mathbf{q},j} \frac{\partial n_j^0(\mathbf{q})}{\partial T} g_j(\omega_{\mathbf{q}}) v_{\mathbf{q},j} l_{\mathbf{q},j} d\omega, \quad (1.33)$$

where $l_{\mathbf{q},j} = \tau_{\mathbf{q},j} v_{\mathbf{q},j}$ is a phonon-mean-free path and g_j is the phonon density of state of branch j . Eq. (1.33) shows explicitly how one can act on κ_{ph} : one mainstream strategy to tune κ_{ph} is to adapt the mean-free path. Another, less explored way stems in trying to adjust the phonon density of state $g(\omega)$ and/or the phonon dispersion $\omega_{\mathbf{q}}$ (hence the speed of sound).[27]

In order to have estimates of the temperature dependence of κ_{ph} at low temperatures, one can go one step further and rewrite eq. (1.33) as follow:

$$\kappa_{\text{ph}} = v_s^2 \int_0^{\Theta_m/T} \tau g(\omega) \frac{x^2 e^x}{(e^x - 1)^2} d\omega, \quad (1.34)$$

with $\Theta_m = \hbar\omega_m/k_B$, $x = \hbar\omega/k_B T$ and the speed of sound is averaged; the sum over j is omitted. In the d -dimensional phonon subsystem, $g(\omega) \propto \omega^{d-1}$, so that when $T \ll \Theta_m$, $\tau = \tau_C$ is dominated by scattering on grain boundaries:

$$\kappa_{\text{ph}} \propto v_s^2 \tau_C T^d \int_0^\infty \frac{x^{d+1} e^x}{(e^x - 1)^2} dx \propto T^d \quad (1.35)$$

Thus, being defined by the density of states only, the temperature dependence of κ in Equation (1.35) is directly related to the dimension of the phonon subsystem.

The Callaway formula

The temperature dependence of thermal conductivity is frequently considered by making use of Callaway's model.[28] In this context, the total scattering time τ is approximated by Matthiessen's rule, $\tau^{-1} = \sum_i \tau_i^{-1}$, where τ_i are generally frequency- and temperature-dependent relaxation rates characterizing different phonon scattering mechanisms. In most cases for insulators and semiconductors,[18,29] one considers three mechanisms:

1. Frequency independent Casimir scattering at boundaries of the sample, $\tau_C^{-1} = a_C$. The magnitude of this parameter can be easily estimated, because $\tau_C^{-1} = \frac{v_s}{L}$, where v_s is the average speed of sound and L a characteristic dimension of the material. L can be one critical size of the specimen, or the size of crystalline domains.
2. Rayleigh scattering at static point-like impurities, $\tau_R^{-1} = a_R \omega^4$.
3. phonon-phonon Umklapp scattering due to anharmonicities, $\tau_U^{-1} = a_U T \omega^2 \exp(-T_U/T)$, dominating the low $T \ll \Theta_D$, the intermediate $T \sim \Theta_D/5$ and the high temperature range

$T \gtrsim \Theta_D/5$, respectively, with Θ_D being the Debye temperature characterizing acoustic phonons.

Combining these three scattering mechanisms, one obtains the following expression for thermal conductivity,

$$\kappa(T) = \int_0^{\theta_D/T} dx \frac{AT^3}{a_C + a_R T^4 x^4 + a_U T^3 x^2 \exp(-T_U/T)} \frac{x^4 e^x}{(e^x - 1)^2}, \quad (1.36)$$

where $A = k_B^4 / 2\pi^2 v_s \hbar^3$ and v_s is the average speed of sound.

Extensions of the Callaway formula

In some cases, the three scattering mechanisms presented in the last section do not provide good agreement with the experimental data, especially in the case of dynamic disorder of ions or molecular units. When low-energy optical modes are present, they can indeed couple with acoustic modes. This gives rise to resonant-phonon scattering, a mechanism that can even dominate the thermal conduction. A phenomenological scattering time has been successfully used in different studies: [30–32]

$$\tau_r^{-1} = a_r \cdot \frac{\omega_0^2 \omega^2}{(\omega_0^2 - \omega^2)^2}, \quad (1.37)$$

where ω_0 is a characteristic-resonant frequency of some vibrational mode, e.g. the rotational mode of a molecular unit. a_r is proportional to the amount of “molecular” units – e.g. hosts in a clathrated structure – and to the strength of the coupling. τ_r^{-1} can be added to other contributions according to Matthiessen’s rule.²

1.2 Thermoelectricity

1.2.1 Thermoelectric generator

In thermodynamics, the Carnot engine is the ideal – the most efficient – way to produce mechanical energy in the form of work. Carnot steam engines transform energy in the form of heat to work, thanks to a moving part. A thermoelectric (TE) device, similarly to a Carnot engine, can convert heat into electrical power. However, the TE device does not contain any moving part. Instead, it relies on the Seebeck effect. Conversely, a TE device can use electricity to pump heat from a cold (T_c) to a hot side (T_h) (Peltier and Thompson effects). In an analogy

²To match the integrand of the Callaway formula, a change of variable can be made:

$$\tau_r^{-1}(x, T) = a_r \cdot \left[\frac{\gamma \omega_0 x}{\gamma^2 \omega_0^2 - x^2} \right]^2, \quad \gamma = \frac{\hbar}{k_B T}.$$

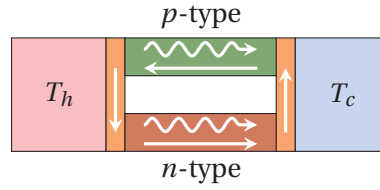


Figure 1.3 – Scheme of a thermoelectric generator. Two “legs” of p- and n- type materials are sandwiched between electrodes. One of the electrode is in contact with a hot reservoir (T_h) and the other one with a cold reservoir (T_c). Due to the thermal gradient, a heat current flows from the hot to the cold side (curly arrows), generating electrical current (straight arrows).

with the Carnot engine, the gas (steam) is replaced by a Fermi gas (of charge carriers) in the TE device, and the pressure by a chemical potential of the Fermi gas.[33,34] This analogy has limitation, though, because dissipation is inherent to the thermal- and heat- transport (see later Equations (1.1a) and (1.1b)). Therefore, the conversion efficiency of the TE device is lower than $\eta_c = T_h/\Delta T$, the Carnot efficiency. Figure 1.3 shows the working principle of the thermoelectric generator (TEG). Upon application of a temperature difference ΔT , a current of energy (heat, denoted by the curly arrows) flows from the from the hot reservoir (T_h) to the cold reservoir (T_c). In reaction to the temperature gradient, electric potentials build in both legs, owing to the Seebeck effect, thus pumping charges through the device (straight arrows). The materials composing the legs are chosen such that in one leg, the current is directed against the heat flow (n-type) and, in the other alongside it (p-type).

In fact, thermoelectric devices are less efficient than engines, because of all the dissipation phenomena, such as convection of heat in the surrounding atmosphere and in the connecting wires, radiations and Joule effect.[35] The case of a single-legged device is explained in more details in Section 5.3.1. TEGs can be coupled in optimised geometries, e.g. as a grid (series) or in a stack (thermal series) to provide more power. However, beyond device engineering, the most important part of the device is the thermoelectric material itself (p- and n-type), and one needs to asses how good a compound behave for thermoelectric applications.

1.2.2 Thermoelectric figure of merit

For best operation, a thermoelectric material must have a high absolute value of the Seebeck coefficient, because S probes the “reactivity” of charge carriers towards a thermal gradient. However, this condition only is not necessary to have an efficient thermoelectric material. One problem could indeed arise from a material with a too high electrical resistivity: charge carriers would tend to flow in reaction to the thermal gradient but there would be a strong opposition to the transport of charges. Therefore a good thermoelectric material should have a low resistivity. Finally, if the thermal conductivity of the material is too high, the thermal gradient could not be maintained, thus reducing the performance of the thermoelectric. A quantification of these features can be derived formally [34,36] and provides a dimensionless parameter characterising a thermoelectric material.

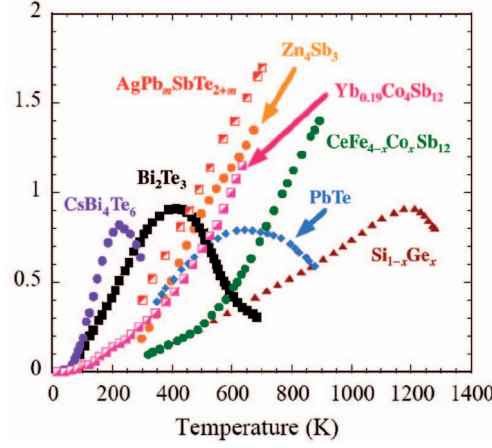


Figure 1.4 – Examples of materials realising a high figure of merit ZT . Reproduced from Ref. 37.

The thermoelectric figure of merit encompasses all the constraints discussed in the previous paragraph, as it is a function of σ the electrical conductivity (inverse of the electrical resistivity ρ), S the Seebeck coefficient or thermoelectric power (TEP), and the thermal conductivity κ , taken at the temperature T :

$$ZT = \frac{\sigma S^2}{\kappa} \cdot T \quad (1.38)$$

where T is the absolute temperature. ZT , together with the gradient ΔT accross the material, determine the thermoelectric conversion efficiency (see Appendix A.3 for a detailed account). Examples of materials with a high ZT are shown on Figure 1.4. The form of equation (1.38) contains all the features that must be fulfilled by a thermoelectric compound: σ and S have to be maximised, whereas κ must be minimised. This optimisation is really challenging and is currently the bottleneck in development of efficient TEGs. Most materials who have a high Seebeck coefficient tend to be bad conductors. On the other hand, materials with high conductivity possess high thermal conductivity, because charges also carry heat (see the Wiedemann-Franz law in Eq. (1.19)).

Figure 1.5 compares the efficiency of thermoelectric devices to that of other power-generating technologies. It appears that ZT should be larger than 2 to compete with other available technologies: this is a reference value, a goal to keep in mind for research and development of thermoelectric materials. However, materials exhibiting lower values of ZT should not be discarded. TEGs, because they are easier to miniaturise than steam engines, could have extremely appealing applications in low-power generation. For example, remote power and “personal” micro-power, necessitating low ΔT , have a great technical and commercial potential, especially a times when the “internet of things” seems to invade a large amount of sensor applications.[35]

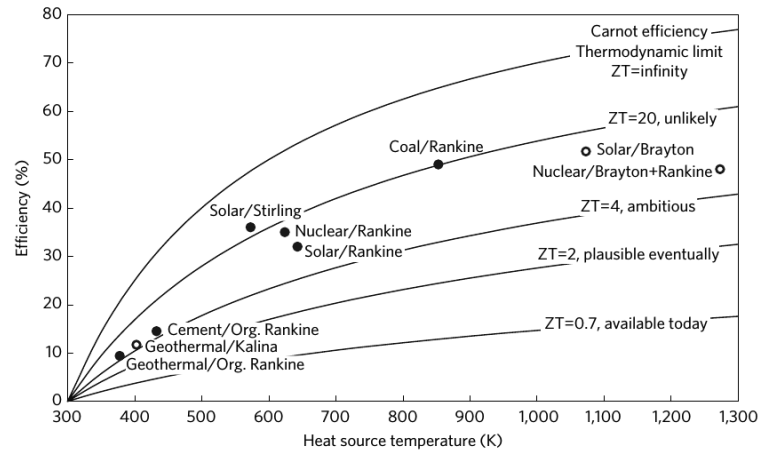


Figure 1.5 – Assessing thermoelectrics. Thermoelectric conversion efficiency as a function of the heat source temperature (T_h), for different values of ZT ($T_c = 300$ K). Reproduced from Ref. 35.

1.2.3 Strategies to optimise ZT

Thermoelectric materials often have a very complex (electronic and lattice) structure. It is challenging to manipulate the properties of these materials without affecting the delicate balance between the transport coefficients. Two strategies are usually adopted to increase ZT . The first one consist in reducing the lattice thermal conductivity κ_{ph} ; the second one focuses on increasing the power factor (PF) σS^2 .

Minimising the lattice thermal conductivity

The most common path to decrease κ_{ph} is to structure a media at meso/nano-scales, thus truncating the phonon-mean-free path (see Eq. (1.33)).[38,39] 100-Fold reduction of the thermal conductivity in silicon nanowires in respect of bulk was reported, and comparable results were obtained in other nanostructured alloys.[40,41] Superlattices or heterostructures have also proven a higher degree of control on thermal properties.[42,43] In addition to shortening the mean-free path, there have also be attempts to adjust the crystal chemistry to promote scattering of phonons and lower the speed of sound.[39] A more subtle way to tune κ was proposed by Maldovan, using thermal bandgap materials and modifying its phonon-dispersion relation by precisely design its nanostructure.[27] Moreover,

Choosing a material with low κ_{ph} is an alternative approach: compounds with complex cage structures (clathrates, skutterudites) and mixed-lattice atoms (half-Heusler alloys) exhibit low thermal conductivities.[44,45] Here, the random vibrations of groups of atoms in the lattice hinder the propagation of heat by phonons. Corresponding phenomena have been described in organometallic perovskites, where crystal-liquid duality, together with the formation of large polarons, account for the very low κ . [46–48] Nielsen et al.[49] were reasoning that compounds with anharmonic phonon modes stand amongst the best candidates to moderate

heat transport.[49–51]

Although these progresses demonstrate the ability to lower κ significantly, fundamental insight into the mechanisms of thermal transport have not been completely deciphered, hence they have to be addressed in further extent, because it helps in designing more efficient materials for thermal management. In addition, many of the proposed low- κ compounds are difficult to scale up for applications, owing to the scarcity of their constitutive elements or to intricate synthesis (e.g. by high-pressure or -temperature, or nano-lithographic processes). Developing materials with few elements and a simple structure thus remains the most viable strategy.

Maximising the power factor

The other approach in attempts to optimise ZT focus on increasing the power factor (PF) σS^2 . To begin with, it is useful to build an intuition of the role of the transport coefficients in ZT, and to have order-of-magnitude indication of their required values. First, the thermal conductivity $\kappa = \kappa_{\text{el}} + \kappa_{\text{ph}}$ must be minimised. Let us assume an ideal case with $\kappa_{\text{ph}} \simeq 0$, and κ_{el} respecting the WFL. In this situation, the effects of resistivity and κ_{el} annihilate themselves, so that $ZT = S^2/L_0$ depends on S only. Taking $ZT = 1$, this gives $S \simeq 157 \mu\text{V/K}$. [37] This permits one to situate the range in which S should lie for good thermoelectric performance.

To maximise S and decouple σ and κ_{el} , low carrier concentrations are required at the same time as high mobility.[52] One way to achieve this is by band engineering, attempting to have a high degeneracy and flat bands. Flat bands indeed give the carriers a low effective mass. In addition, chemical doping can help promoting only one type of carriers and/or to increase the band gap of alloys.[37,52,53] A good example of band gap engineering is the doping with calcium of SnTe.[54] Here, the addition of Ca has two main effects: first it reduces the hole concentration; second the energy gap increases. As a result, several bands with larger effective masses become active in transport.

Finally, it is worth mentioning the work of Gaultois *et al.*, whose methodology is rather original: they used machine-learning to select unremarked or new materials with predicted-promising-thermoelectric properties.[55] Along with this study, they propose a very useful permitting on-demand visualisations of thermoelectric data from a large database (available at <http://www.mrl.ucsb.edu:8080/datamine/thermoelectrics.jsp>).[56]

2 Transport in selected high-entropy alloys

Metallic alloys compose a very large class of versatile materials, with uncountable available applications in everyday life as well as for very specific or demanding requirements (e.g. space exploration). Usually, two or more metallic elements are mixed (alloyed) with one principle (matrix) element in large concentration (> 50 at%). In general, alloying permits to tune/improve the desired properties of a metallic matrix. For example, adding a few atomic percent of carbon to iron drastically modifies the mechanical properties of iron, making it tough and resistant to corrosion.

Although a multitude of systems containing one or two principle (matrix) elements have been largely enquired, alloying of more than two metals in equal ratios has remained unexplored for a long time. Multiple-principle-elements alloys, also called complex-concentrated alloys or high-entropy alloys (HEAs) were recently approached to host rich physical phenomena.[57–59]

2.1 High-entropy alloys

There is no strict definition of HEAs, instead, three complementary criteria exist:[59]

1. Composition criterium: alloys with more than 4 elements in nearly equimolar concentration (between 5 and 35 at%).
2. Molar entropy of mixing: the molar entropy of mixing is larger than $1.5R$, with R the universal gas constant.¹
3. Microstructure: alloys forming a single phase solid solution of high symmetry (bcc, fcc or hcp).

Here, the first concept that gave rise to speculations about the potential of HEAs is the entropy

¹The molar entropy of mixing for a compound with N species with concentration x_i , $i = 1, \dots, N$ is $\Delta S_{\text{mix}} = -R \sum_{i=1}^N x_i \ln x_i$. It follows that for a material with equimolar concentrations, $\Delta S_{\text{mix}} = R \ln(N)$.

of mixing. In an ideal solid-solution, the atoms of different elements are randomly distributed to the lattice sites (Figure 2e). This maximal disorder could lead to interesting functionality.[59]

The momentum to study thermoelectric properties of HEAs emerged from the idea that the high-entropy, in other words the random distribution of atoms in a simple cubic lattice structure, could translate into high-entropy of other physical quantities, such as electronic, vibrational or magnetic “entropy”. The coefficient of choice to probe electronic entropy is the Seebeck coefficient, as it can be related to the entropy per charge carrier.

Structurally, there is a direct consequence expected from the high entropy of mixing. Arising from the difference in atomic masses and radii, strong distortions of the lattice could influence, or even govern the electronic, magnetic and vibrational properties of the alloys. Only few studies so far have dealt with electrical and thermal conductivities of HEAs, experimentally or numerically.[60–65] Jin *et al.* reported the temperature-dependent electrical and thermal conductivities of a series of Ni-based HEAs,[61] however, no investigations of the Seebeck coefficient were found in the literature. The peculiar structure of HEAs fills a gap between crystalline lattice and quasi-crystals, and therefore it is very important to assess their thermoelectric properties. Finally, since we expect unforeseen physical phenomena to arise in HEAs (“cocktail effect”[59]), and regarding the distorted lattice of these alloys, there is a hope to use these materials for thermoelectric applications, if their electrical resistivities and thermal conductivities are low enough compared to their thermopower.[64]

For this work, series of multiple principle elements with a face-centred-cubic (fcc) structure based on 3d-transition metals were prepared by arc-melting. The starting material is nickel (Ni), and a series of 7 alloys with increasing chemical complexity are added subsequently. The principle elements, in their order of addition are iron (Fe), chromium (Cr), cobalt (Co), copper (Cu), aluminium (Al) and titanium (Ti).

2.1.1 Synthesis of high-entropy alloys

All alloys were synthesised by first pressing elemental metals ($\sum m_i \approx 1.5$ g) into pellets. Following this preliminary step, the pellets were placed in a chamber, evacuated and then filled with argon (Compact Arc Melter MAM-1 with a motor-driven, water-cooled tungsten electrode which can be positioned freely above the crucibles). To remove any residual oxygen in the pellets, elemental zirconium was heated until it glows, in the same chamber. Second, 20% of the maximal-available power was sufficient to fully melt our samples, by vacuum arc melting.² The arc melting was repeated at least three times, rotating the samples between each step. The resulting drop-like specimen ($m \approx 1.35$ g each) were diced by electrical discharge machining (copper wire) into slices of ≈ 0.5 mm thickness and polished with gradually finer silicon-carbide sandpaper to remove copper and oxides from surface. The slices were finally cut into bars with WS-22 high-precision wire-saw (tungsten). In some cases, Cr/Au electrical contacts were deposited by sputtering (inset of Fig. 2.1), or in others 50 μ m Au-wires were

²The maximum-reachable temperature of the arc melter is 3500°C.

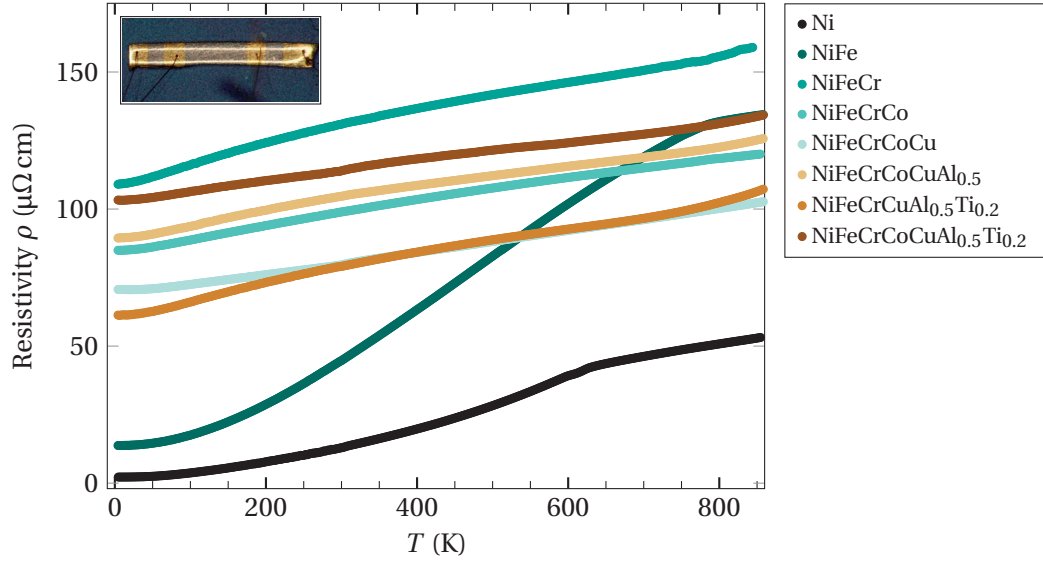


Figure 2.1 – Temperature-dependent resistivity of as-cast Ni-based high-entropy alloys. The inset (bottom right) shows a bar-shaped samples with 4 Au-wires bonded to sputtered Cr-Au electrodes; the width of the inset is about 10 mm.

spot-welded onto one face of the bar.

The HEA samples were characterised by means of X-ray diffraction (XRD) and proved to have a well-defined fcc crystalline structure. The analysis of the half-width of diffraction peaks (Deby-Scherrer relation [66]) provided an estimate of the crystallite size of about 15 to 21 nm in most specimen. Scanning-electron microscopy (SEM) and electron-dispersive X-ray spectroscopy (EDS) revealed precipitates of copper and titanium in the structure, for the alloys containing these elements.

In addition to the as-cast samples, a small quantity of each alloy was annealed in an evacuated-quartz ampoule, for one month at 1030°C, after which they were quenched in water.

2.2 Thermoelectric properties

The resistivity of our eight metal and alloys was measured from 4 K to 850 K and is presented on Figure 2.1. All have a temperature dependence characteristic of a metal ($\frac{d\rho}{dT} > 0$). Nickel was prepared in the same manner as the other alloys so that its thermoelectric properties could be compared with results available in the literature, thus providing a reference for the other measurements. Its resistivity correspond to that of polycrystalline Ni,[67,68] with a residual resistivity of 2 $\mu\Omega\text{cm}$ and the magnetic transition at $T_C \approx 630\text{ K}$ (Fig. 2.7). Here $\rho(T)$ was reported to follow Matthiessen's rule, where ρ is the sum of a temperature-independent contribution of scattering of electrons on impurities, and a temperature-dependent term, following a T^2 -law at low temperatures ($< 20\text{ K}$), accounting for interaction between itinerant electrons.[69,70] Subsequently to these studies, models have been developed, arguing that a

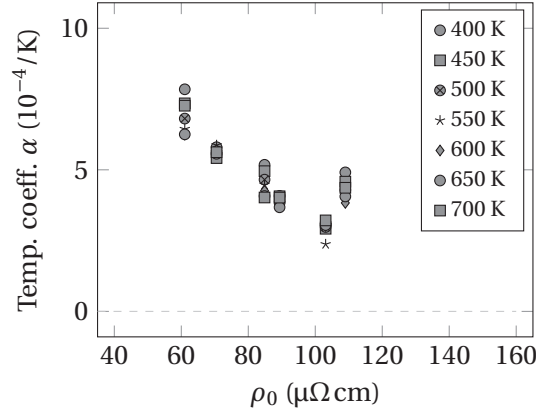


Figure 2.2 – Temperature coefficient $\alpha = \frac{1}{\rho} \frac{d\rho}{dT}$ of the (high-entropy) alloys in Fig. 2.1 (Ni and FeNi are excluded). α was calculated at different temperatures from 400 to 700 K, with little difference.

two-band conduction occurs in Ni, due to spin-polarisation. For the next alloy, FeNi, addition of Fe in equiatomic concentration has two effects. First, it increases the residual resistivity and second, the temperature coefficient is higher. $\rho(T)$ follows a quadratic-power law in T over a broad temperature range, from 10 to ~ 500 K. This is an indication that electron-electron interaction are enhanced as the temperature increases (I will discuss the properties of Fe-Ni alloys in more details in Section 2.3).

For the alloys with three principle elements or more, there is a qualitative change in the resistivity compared to Ni or FeNi. First of all, the residual resistivities have values ~ 1 order of magnitude higher than for Ni and NiFe. Furthermore, the temperature coefficient $\alpha = \frac{1}{\rho} \frac{d\rho}{dT}$ is much lower than that of Ni and NiFe. There is no obvious correlation between the number of alloying elements and the slope of the resistivity, or with ρ_0 , above three elements, as it was found for similar alloys in an independent study.[61] Moreover, one can observe an upturn in ρ at low temperatures for NiFeCoCrCu. This is the signature of Kondo effect, when electrons are scattered by dilute magnetic impurities at low temperature.[61]

The anomalous electronic properties of binary or ternary alloys, outside of the dilute limit, have been discussed by Mooij.[71] It has been observed for a variety of systems (glassy metals, amorphous alloys, etc.) that, as the residual resistivity ρ_0 approaches a critical value ρ_c , the temperature coefficient α changes sign, to become negative for alloys with $\rho_0 \gtrsim \rho_c$. For these disordered systems, in particular metallic alloys, Mooij found a linear (anti-)correlation between the temperature coefficient and the resistivity. $\rho_c \approx 150 \mu\Omega$ cm corresponds to the Mott-Ioffe-Regel (MIR) limit, when the scattering length coincides with inter-atomic distances.[72] The temperature coefficient α of six high-entropy alloys is plotted against their resistivities, for four reference temperatures on Figure 2.2. They fall well within the Mooij-correlation behaviour.[71,73] The temperature coefficient belongs to a similar range as for other alloys: for comparison, in Ni α is about 2 orders of magnitude larger. If one would draw a line following the trend in α , the intercept would be at $\sim 140 \mu\Omega$ cm, reasonably close to the

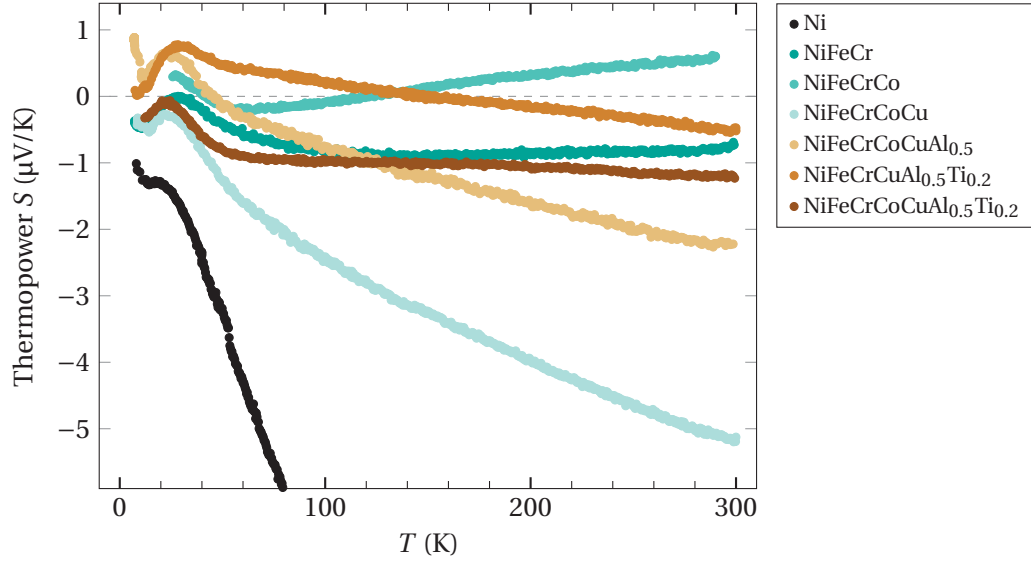


Figure 2.3 – Temperature-dependent thermopower (S) of as-cast Ni-based high-entropy alloys.

MIR limit. The difference could be explained by the change in lattice constant between the different materials. Furthermore, Ciuchi *et al.* explain in a recent study that a universal scaling of α is only possible if ρ_0 is properly rescaled to avoid material-dependent interference.[73] In the same article, they shed light on the possible mechanism at the origin of the anomalous $\rho(T)$: a polaronic mechanism of strong disorder renormalisation.

The Seebeck coefficient, as a measure of the entropy per charge carrier, could be the ideal quantity to probe effects of the atomic disorder on electronic properties. The temperature-dependent thermoelectric power is reported on Figure 2.3. It comes at a surprise that the values measured for the HEAs are very low, comparable to that of metals like gold or silver. NiFeCrCoCu has the maximal absolute value at room temperature, with $-5.1 \mu\text{V/K}$, and decrease towards zero, as the temperature decreases. For two alloys, NiFeCrCo and NiFeCrCuAl_{0.5}Ti_{0.2}, S changes sign at ~ 150 K, however S is only weakly dependent on the temperature. Such low values of S for disordered systems have rarely been seen. NiFeCr and NiFeCrCoCuAl_{0.5}Ti_{0.2} have a nearly constant value of $\sim -1 \mu\text{V/K}$ from 70 to 300 K. This is highly unusual and cannot be explained in simple terms. For disordered systems with localised states, and where the transport is determined by a variable-hopping-like mechanism, $S \propto T^{1/2}$, a relation that does not hold with the experimental data on Fig. 2.3. Nevertheless, we can make the hypothesis about the origin of the low S . One scenario that could be viable is that of a density of state that is highly irregular in the vicinity of the Fermi level, changing rapidly (see Fig. 1.2 and Eq. (1.27)). Here, more a thorough analysis with the help and power of numerical simulations would be beneficial for a better understanding.

The thermal conductivities of NiFeCrCoCuAl_{0.5} and NiFeCrCoCuAl_{0.5}Ti_{0.2} were measured from 10 to 300 K. As they are very similar in magnitude and temperature dependence, only κ of the latter is presented on Figure 2.4. For this HEA, $\kappa(T)$ increases from 0 towards 10.6 W/Km

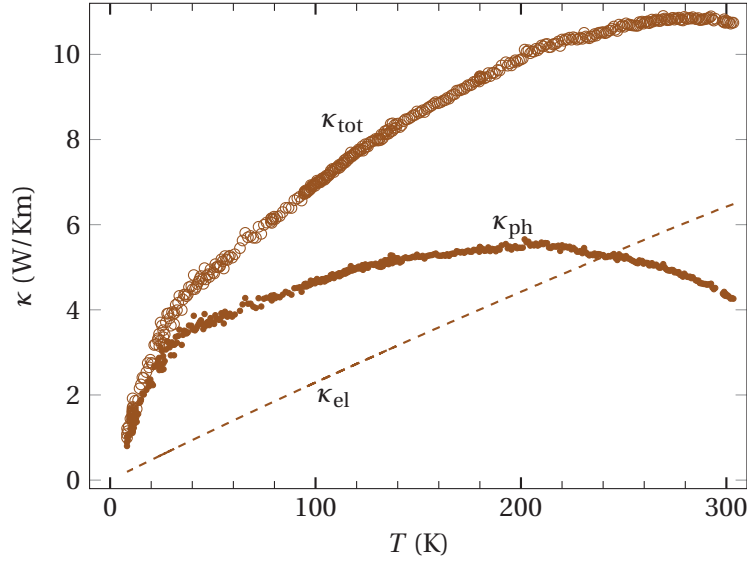


Figure 2.4 – Temperature-dependent thermal conductivity $\kappa_{\text{tot}} = \kappa_{\text{el}} + \kappa_{\text{ph}}$ of as-cast $\text{NiFeCrCoCuAl}_{0.5}\text{Ti}_{0.2}$. The electronic contribution to the total thermal conductivity, κ_{el} (thin line) has been estimated from the Wiedemann-Franz law.

at room temperature. This value is lower (one order of magnitude) than for pure metals, and comparable to κ of e.g. steel. Because the resistivity is known, the part of the thermal conductivity due to transport via the charge carriers κ_{el} can be estimated with the Wiedemann-Franz law.³ Consequently the lattice-thermal conductivity is estimated at $\kappa_{\text{ph}} = \kappa_{\text{tot}} - \kappa_{\text{el}}$ (Fig. 2.4). This separation of κ in two contributions permits us to observe that at high temperatures (> 250 K), the thermal transport is dominated by the electronic part whereas, at low temperatures, the phonon system governs it. $\kappa_{\text{ph}}(T)$ is relatively low and glass-like: it reflects well the polycrystalline and disordered nature of the alloy. Above 200 K, it decreases with rising T , likely a consequence of three-phonon scattering processes.

It is interesting to note that measurements of ρ and S of the annealed sample displayed no significant, qualitative difference with the results presented here. Therefore they are not shown in this section.

Our expectations to see the molar entropy of mixing translated into a high value of thermopower is not realised in the selected high-entropy alloys. Instead S yields exceptionally low values, comparable to that of pure metals, however not governed by standard diffusion of the charge carriers. Therefore, the prospects of transforming Ni-based HEAs to thermoelectric devices fades away in regard of the very low Seebeck coefficient of these materials. Nonetheless, a feature of the “simplest” alloy considered in this chapter (FeNi) has attracted our attention: it is distinguished by the high absolute value of its thermopower $S = -50 \mu\text{V/K}$ at room temperature, thus yielding a power factor (PF) σS^2 of $58 \mu\text{W/K}^2\text{cm}$. This elevated value of the

³One should be careful and keep in mind that, for such highly disordered system with polaronic interactions, there is not warranty that the Lorenz number L_0 is constant.

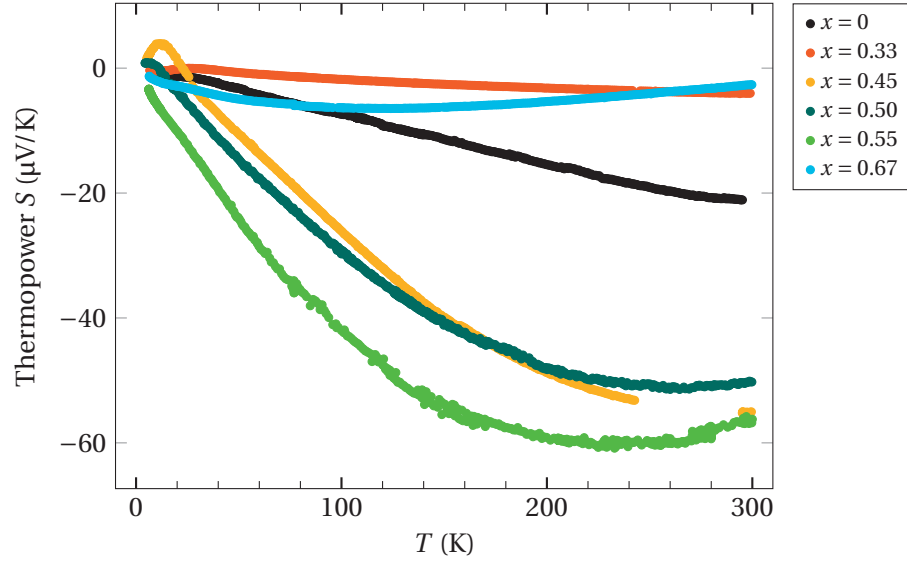


Figure 2.5 – Temperature-dependent thermopower (S) of $\text{Fe}_x\text{Ni}_{1-x}$ as-cast alloys, at different concentration of Fe (x).

power factor, one of the key ingredients for efficient thermal energy conversion, compares with that of commercially available thermoelectrics. For Bi_2Te_3 , $\sigma S^2 \approx 20 \mu\text{W}/\text{K}^2\text{cm}$. We have not found any discussion promoting FeNi as a potential thermoelectric material in the literature. Therefore we further investigate the thermoelectric properties of the $\text{Fe}_x\text{Ni}_{1-x}$ system in the next section.

2.3 FeNi alloys

Iron-nickel alloys ($\text{Fe}_x\text{Ni}_{1-x}$) provide a vast range of properties. Also known as permalloys, or super alloys, they are used in aero-spatial applications because they stand high temperatures without deforming.[74,75] Beside their outstanding mechanical properties, their magnetic properties can be tuned with the composition (x) and/or by heat treatment (annealing, rapid cooling). In fact, FeNi alloys were the first alloys encountered by mankind, even before bronze age, because it was a natural alloy brought on earth by meteorites.[76] It is also found in Earth's core.[77] Last, $\text{Fe}_{0.65}\text{Ni}_{0.35}$ has the peculiar property not to experience thermal expansion over a wide temperature range (Invar system).[78]

Beyond studies on mechanical and magnetic properties of $\text{Fe}_x\text{Ni}_{1-x}$ alloys, there have been many reports elucidating the electrical transport in this system.[67–70,79–83] However, only scarce investigations on thermopower and thermal conductivity are available. S of Ni is explained well by the diffusion thermopower for simple metals of Eq. (1.28) ; upon addition of Fe in dilute quantities, a phonon-drag contribution to S appears through a local minimum around 40 K.[84] This phonon-drag is due to the mixed-spin nature of the system. In addition, S at room-temperature as a function of x was reported claiming that a link exists between S

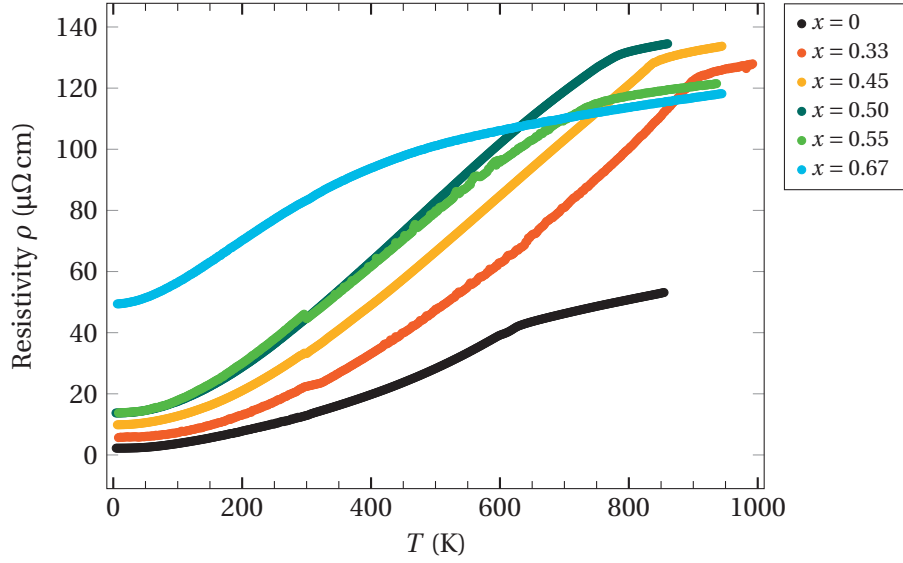


Figure 2.6 – Temperature-dependent resistivity of $\text{Fe}_x\text{Ni}_{1-x}$ as-cast alloys, for different atomic percent of Fe (x).

and the heat of mixing.[85] In order to study the system in more details, and motivated by the very high power factor of equiatomic FeNi , we prepared different compositions (x) of $\text{Fe}_x\text{Ni}_{1-x}$ by the same arc-melting method presented earlier. Their composition and structure (fcc) was confirmed by XRD analysis.

The thermopower of Ni and five $\text{Fe}_x\text{Ni}_{1-x}$ alloys is presented on Figure 2.5. Apart from pure Ni, the Seebeck coefficients of the alloys have a non-trivial temperature dependence. $S(300\text{ K})$ is low ($< 5\text{ }\mu\text{V/K}$ and lower than for Ni) for $x = 0.33$ and $x = 0.67$. However, when the concentration of Fe is near the equiatomic ratio, S is enhanced to a maximal value $S = 56\text{ }\mu\text{V/K}$ at $x = 0.55$. As x increases, there seem to be a minimum in S shifting from room temperature ($x = 0.45$) towards lower T ($\sim 100\text{ K}$ for $x = 0.67$). The origin of the large enhancement of S for near-equiatomic $\text{Fe}_x\text{Ni}_{1-x}$ is unclear and requires further investigations, because this effect could be beneficial for efficient thermoelectric materials.

Figure 2.6 shows the resistivity of Ni and the same alloys. Except for $x = 0.67$, all specimen have a residual resistivity below $18\text{ }\mu\Omega\text{ cm}$ and rise with temperature. Their residual resistivities gradually increase with Fe concentration x (Fig. 2.7b). They all have a kink above 600 K , which is associated to a magnetic transition: the alloys become paramagnetic above the Curie temperature T_C . From 5 to 500 K , $\rho(T)$ scales as T^2 . The sample that contain more Fe (light blue curve) has a higher residual resistivity ($\rho_0 = 50\text{ }\mu\Omega\text{ cm}$), the magnetic transition occurs at a lower temperature ($T_C \simeq 400\text{ K}$) and the transition is less sharp than for the other alloys. This is a sign of increased disorder. It is also interesting to note that $x = 0.67$ is part of the invar systems, which are known to display anomalous behaviours, e.g. in their thermal expansion. As the phase diagram of $\text{Fe}_x\text{Ni}_{1-x}$ has been established,[79] it provides an additional way to assess the composition of our samples, through Curie temperature. $T_C(x)$ is reported on

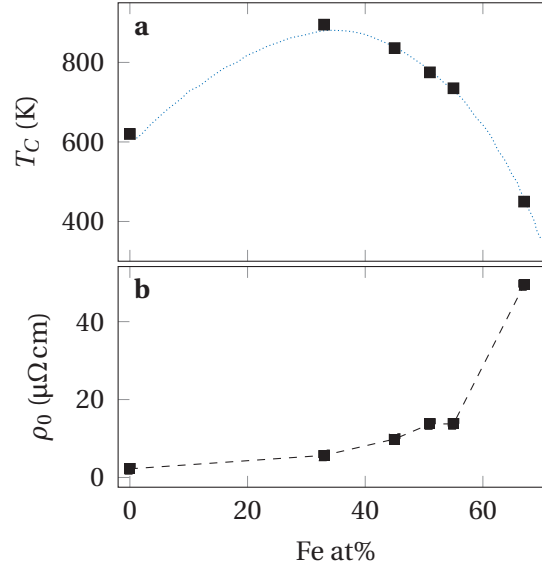


Figure 2.7 – **a** Curie temperature of the FeNi alloys as a function of the Fe atomic concentration x . The blue-dotted line is reproduced from the phase diagram in Ref. 79. **b** Residual resistivity ρ_0 increasing with x .

Figure 2.7a. Our data for T_C , extracted from the resistivity curves, perfectly matches the phase diagram (dotted line).

The knowledge of $\rho(T)$ and $S(T)$ permits us to calculate the power factor σS^2 for the different $\text{Fe}_x\text{Ni}_{1-x}$ alloys. Three of the alloys, the ones with Fe concentrations close to equi-atomic ratio, have a remarkably high power factor. Whereas for Ni, the power factor equals $35 \mu\text{W}/\text{K}^2\text{cm}$, it increases to 58, 70 and $92 \mu\text{W}/\text{K}^2\text{cm}$ for $x = 0.5$, 0.67 and 0.45 respectively. Another feature of the PF of these compounds is a wide maximum 150 and 200 K. For the sample containing 55% of Fe, this maximum reaches the high value of $130 \mu\text{W}/\text{K}^2\text{cm}$. In order to see if the high PF translates into high ZT, we measured the thermal conductivity of two of the alloys ($x = 0.5$ and $x = 0.45$).

On Figure 2.9, one can observe $\kappa(T)$ of both materials, that have qualitatively a similar dependence in temperature, increasing from 0 to a maximum value and then decreasing slowly as the temperature rises. However, extracting κ_{ph} using the WFL as an estimation of κ_{el} , both alloys display significantly different behaviours. In the equi-atomic FeNi, κ_{ph} and κ_{el} both contribute to the thermal conduction, whereas for $x = 0.45$, κ_{el} clearly dominates over κ_{ph} . Here, κ_{ph} is comparable to the results found for $\text{NiFeCrCoCuAl}_{0.5}\text{Ti}_{0.2}$ in Fig. 2.4. Although both compositions are close, the mismatch between κ_{ph} of the two different compositions is large ($\kappa_{\text{ph}}^{0.55}$ is 5-fold larger than $\kappa_{\text{ph}}^{0.50}$ at 250 K). It indicates that some scattering must act to reduce the phonon-mean free path in $\text{Fe}_{0.45}\text{Ni}_{0.55}$. Such damping occurs above ~ 35 K and could be due to an order-disorder phase transition of FeNi.

Provided with these results, the thermoelectric figure of merit ZT can be calculated

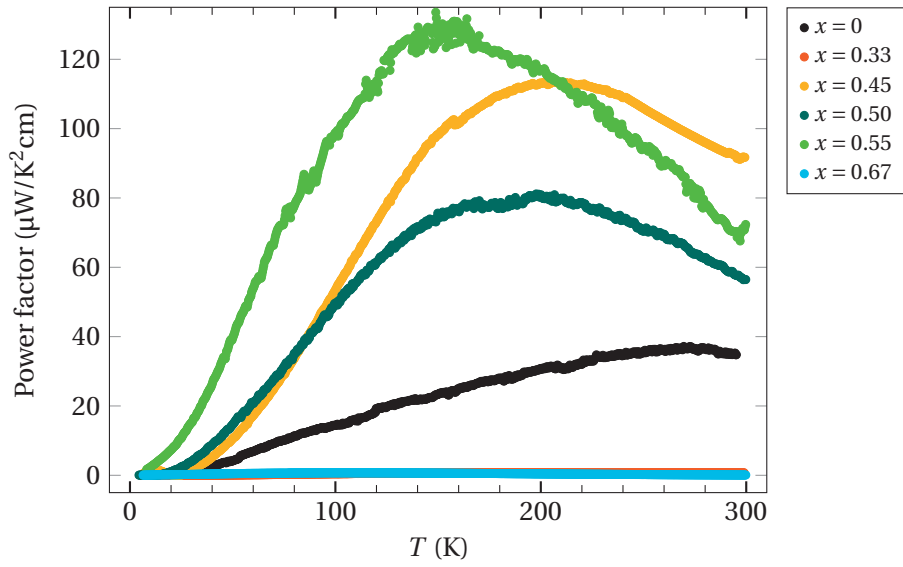


Figure 2.8 – Temperature-dependent power factor σS^2 of as-cast $\text{Fe}_x\text{Ni}_{1-x}$ alloys at different Fe atomic concentrations (x).

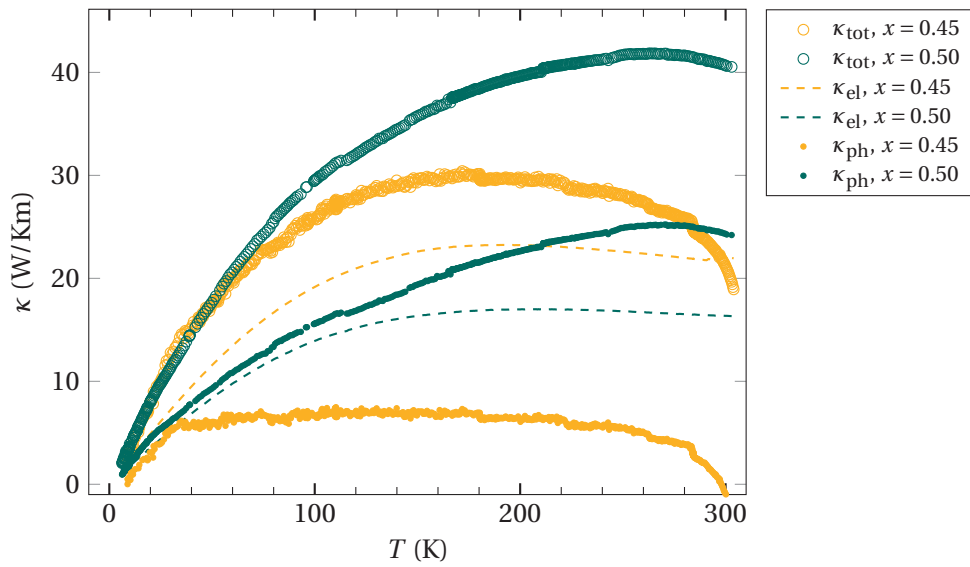


Figure 2.9 – Thermal conductivity of two as-cast FeNi alloys, with Fe atomic concentrations of $x = 0.5$ and $x = 0.45$. The contributions of κ_{el} and $\kappa_{\text{ph}} = \kappa_{\text{tot}} - \kappa_{\text{el}}$ have been estimated from the Wiedemann-Franz law.

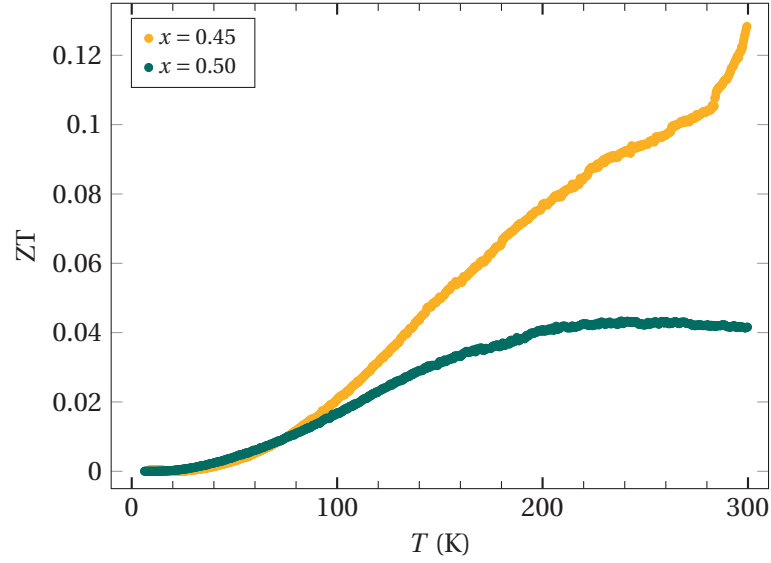


Figure 2.10 – Thermoelectric figure of merit ZT of two as-cast FeNi alloys.

(Figure 2.10). For the equi-atomic alloy, ZT saturates at 200 K before slowly decreasing, with a moderate $ZT = 0.04$ at room temperature. For $\text{Fe}_{0.45}\text{Ni}_{0.55}$, it monotonically increases towards the value of 0.12 at 300 K. This value is very promising for an as-cast alloy with a very simple composition, synthesised by arc-melting. It is only one order of magnitude below unity, the value required for viable applications. The high ZT is possible in this material by the combination of high thermopower ($-55 \mu\text{V/K}$), low resistivity and by reducing κ by texturing the material.

2.4 Conclusions

We have reported the thermoelectric properties of Ni, $\text{Fe}_x\text{Ni}_{1-x}$ series and six Ni-based as-cast high-entropy alloys. We observe no apparent correlation between the transport coefficients and the number and type of alloying elements. The resistivity of HEAs has a low-positive temperature coefficient ($\alpha < 10^{-4} \text{ K}^{-1}$) and takes values in the range of 60 to $160 \mu\Omega\text{cm}$. Unexpectedly, their thermoelectric power is very low, comparable to that of pure metals. This effect has never been documented and deserves further investigations. It seems that disorder and polaronic effects due to the random arrangement and variations of masses could be a basis for reasoning. As no simple argument can describe S of HEAs, theoretical modelling could help solving this puzzle.

Next, the transport coefficients of as-cast $\text{Fe}_x\text{Ni}_{1-x}$ alloys have been reported. Large variations in the electrical and thermal transport occur upon variation of the Fe atomic ratio x . We found that $\text{Fe}_{0.45}\text{Ni}_{0.55}$ has a high figure of merit of 0.1 at room temperature. This study thus sets the ground for further engineering of FeNi alloys. This could have consequences on the development of novel FeNi-based thermoelectric materials. Indeed, the opportunities

to tune the thermoelectric properties are manifold in this system. First, the atomic ratio \bar{x} that would optimise ZT should be found. We expect it to lie in the interval $0.4 < \bar{x} < 0.55$. A second step would be to play with the order/disorder, or crystallinity by appropriate thermal treatments or different syntheseses. For example, it is possible to synthesise $\text{Fe}_x\text{Ni}_{1-x}$ powders by precipitation from a solution. Another way to indirectly tune ZT would be to play with the structure at a meso-/nano- scale, with the goal to reduce the phonon-mean-free path. One option would be to synthesis metal-FeNi foams (see Chapter 3), or prepare FeNi heterostructures. However, this approach might not be the most efficient, because the thermal conductivity of the phonon subsystem is already low, so that any change would be shadowed by the electronic thermal conductivity. Finally, the addition of other elements in dilute quantities (chemical doping) could impact favourably the thermoelectric and permit a fine adjustment of the desired properties. In addition, if one could dope the $\text{Fe}_x\text{Ni}_{1-x}$ system to change it to a p -type conductor, commercial applications would be viable even at $ZT = 0.1$.

3 Charge and heat transport in metal foams

3.1 Metal foams

A foam, by definition, is an arrangement of matter formed of gas cells trapped in a solid or liquid matrix. The size and positioning of the cells is usually disordered. In *closed-cell* foams, the cells are separated from each-other by a membrane, whereas in *open-cell* foams the cells “communicate” with each other, and only filaments of the matrix go around them. An example of the former is the foam topping a draft beer, and of the latter insulation materials used in constructions.

Liquid foams can form and stabilise only under some circumstances. Injecting gas into water (or any single-component liquid), bubbles will form and drift towards the surface and eventually pop. In this example, drainage of the bubbles prevents the formation of the foam, in addition to the rupture of the cell (bubble) wall. Thus, for the foam to be stable, there should be no drainage of the cells and the cell walls should resist against external perturbations. [86] A common approach to limit drainage of the bubbles is to add elements to the liquid to enhance its viscosity. Furthermore, an additional force is necessary to stabilise the film (or filaments) surrounding a cell. This is made possible by adding a surface-active component (surfactant). Recalling the example of water, addition of soap enables the formation of a foam.

Metals can be foamed, like water. These metal foams are very interesting for applications, because they combine attractive features of metals, like high electrical and thermal conductivity and good mechanical properties with light-weight and large surface-to-volume ratios.[87,88] One of the most regarded feature of metal foams is their use for thermal control. On the one hand, the foamy material is a poor thermal conductor compared to its bulk matrix, because of the high porosity of the foam. This effect can be used to prevent heat to be transfered to mechanical parts, for example in automotive applications or buildings. On the other hand, the high surface-to-volume ratio of an open-cell foam favours heat transfer from a surrounding gas to the foam. The heat recuperated in this way can then be extracted because the matrix has a relatively high thermal conductivity. Such heat exchangers are already used in buildings, automotive and aerospace applications. Next to their attractive

Chapter 3. Charge and heat transport in metal foams

	Aluminium alloys	Aluminium foams	Stainless steel
Density (g/cm ³)	2.55 – 2.85	0.50 – 2.00	7.75 – 8.05
Young's modulus (GPa)	70 – 140	0.7 – 100	180 – 200
Melting point (°C)	660 – 1200	660 – 1200	2200 – 2900
Thermal conductivity (W/Km)	90 – 170	2 – 100	35 – 50

Table 3.1 – Room-temperature physical properties of aluminium alloys.

thermal properties, metal foams possess good, tunable mechanical properties. As the cell sizes and the porosity of the material is varied, the Young's modulus can be adjusted. High compression strength and toughness combined with low-density material are properties sought for automotive applications. In this case, the security provided to customers is improved in conjunction with cost savings and reduction of CO₂ emissions. Biomedical applications of these light-weight and tough materials as prosthetic implant also exist. Another important category of applications is sound insulation. Here the cellular structure of the foams damps vibrations efficiently. An example of its use is a gun's silencer, where the light weight adds to the acoustic damping. Finally, the good electrical conductivity of metal foams enables them to be employed as electromagnetic shielding elements. It is worth mentioning that metallic-foam panels or constructions are also appreciated for their aesthetics, and are materials of choice for designers.

3.2 Aluminium foams

Amongst metal foams, aluminium foams are the most popular and most widely researched materials. Aluminium and its alloys offer manifold combinations of tunable mechanical, electrical, thermal and chemical properties in conjunction with a relatively low density around 2.7 g/cm³. [89] For comparison, stainless steel has a density more than three times higher, as reviewed in Table 3.1. After oxygen and silicon, aluminium is the most abundant element on Earth, thus being the most abundant metal in Earth's crust. An additional feature of aluminium is its resistance to corrosion. This is in part due to the nearly instantaneous (<1s) oxidation of a thin layer (≈ 2 nm) on surfaces of aluminium in contact with an oxidating atmosphere (e.g. air). Foaming of pure aluminium possible (see next section), however, depending on the production method, the foam might not be stable because of the absence of surfactants. [86,90] Therefore, so-called aluminium foams are in fact most often aluminium-alloys foams or even metal-matrix-composite (MMC) foams. The complexity of the alloys adds one more degree of freedom in tuning the properties of the foams, although they call for more refined and difficult physical interpretation. In this study, we will focus on the study of aluminium-based crystalline alloys, in particular with different silicon- and magnesium-containing alloys. Although the electrical resistivity at room temperature and above has been reported in numerous studies, there are no records of temperature-dependent thermoelectric power or thermal conductivity for these materials. These alloys will be referred as Al_xSi, where

x is the approximate content (weight%) of silicon. They are popular in industry owing to their low density and good mechanical properties. Furthermore, Al x Si alloys reinforced with SiC particles show higher hardness and tensile strength. Foams made by these metal-matrix composites (MMC) also have improved stability and can be manipulated and solidified to form any shape.[91,92] A commercially available aluminium MMC is A359 with 20% volume SiC particles of 20 μm diameter (called Duralcan F3S.20S). Al x Si and Al-MMCs foams already have applications in the automotive, naval, construction industry. Importantly, aluminium foams could play a role as a functional material in batteries and for CO₂ harvesting, or both at the same time.[93] Therefore it is very important to know their thermo-electric properties for these particularly demanding applications.

The structure of the foams plays a very important role in their functional properties. For most synthesis methods, the arrangement and size of the cells show a disordered character. Characterisation of geometrical features of the foams are possible when the structure displays regularity in some aspects. Usually, bubbles are described by spheres of average diameter D , and cell walls are attributed an average thickness. A good parameter to assess properties of a foam is its porosity $\phi = 1 - \frac{\rho_f}{\rho_0}$, where ρ_f and ρ_0 are the density of the foam and matrix material, respectively. Most aluminium foams studied in the literature can be regarded as percolation systems, where the percolation threshold is very close to $\phi = 100\%$.[94,95] This is particularly useful to analyse the properties of the foams in comparison with properties of the bulk material, as “universal” scaling relations can be observed. In particular, different studies have stated that, for the electrical conductivity σ_f of closed-cell foams, σ_f/σ_0 scales as $(1 - \phi)^{\frac{3}{2}}$ for large porosities.[96–102] In the same context, mechanical properties of various aluminium foams have been widely studied.[103–107] These works focus on the comparison between bulk and foams materials, without exploring in details the influence of the micro-structure on the electronic properties. Thermal conductivity of open-cell-[97,108,109] and closed-cell-[110] aluminium foams has been measured for a few specimen, but only at fixed temperature (room temperature). It would be interesting to measure thermal and electrical properties of metal foams over the whole temperature dependence to gain more insight on transport in these materials. At low temperature, unexpected phenomena could arise because of size effects. Indeed, when the electron/phonon mean-free path increases and becomes comparable to critical dimensions of the structure, interactions could be highlighted.

In the next section, different methods to produce aluminium foams are reviewed. Even though we focus on the case of aluminium, these procedures are also applicable to other alloys, through adjustments.

3.2.1 Preparation of the foams

Due to the large interest in metal foams for applications, different methods for foaming have been developed:[87,111] they are summarised in Table 3.2. Four main production procedures are the most common: use of removable placeholders, polymer sponge templating, melt

Chapter 3. Charge and heat transport in metal foams

Closed-cell		Open-cell	
Melt metallurgy	Powder metallurgy	Polymer sponge	Placeholder
Alporas (Foamtech)	Fominal (Fraunhofer)	Inv. casting (ERG)	Exxentis
Alusion (Cymat)	Alulight (SAS)	M-pore (Mayser)	Castfoam (Alveotec)
Aluhab (Aluinvent)	AFS (Pohltec)	Coating (Alantum)	
		Recemat	

Table 3.2 – Production methods for metal foams. Schematic grouping of the commercially most relevant production methods of metal foams and sponges. AFS: aluminium foam sandwich. Reproduced from Ref. 87.

metallurgical route (ML) and powder metallurgical route (PM). The two former provide open-cell foams, whereas the two latter closed-cell structures.

The use of a polymer sponge as a template enables regular structure of the foams (replication of the template structure), with evenly spaced cells and fixed filament thickness. Moreover, flexibility in the choice of the polymers/waxes offers tunability and this technique can be used with many metals, like iron or copper. The porosities of such foams is usually higher than 80%. However, their fabrication requires many steps and reshaping of the foam is difficult. The other procedure relying on infiltration or casting of molds filled with a placeholder present similar advantages as the first method, but are easier to implement. NaCl salt is used, e.g., for casting aluminium (or aluminium alloys). The technique works in this case because the melting point of the salt is higher than the melting point of aluminium. After solidification the salt can be easily dissolved in water. Both methods described in this paragraph permit the preparation of pure-metal foams, which is not the case of the PM and ML routes.

The preparation of the foam from metallurgic powder is based on a principle similar to baking bread. Metallic powder is mixed with a blowing agent (often TiH_2) and sintered by extrusion. The resulting precursors can then be heated so that the gas of the blowing agent expands to create pores. Similarly, in an other approach (ML), the blowing agent can be administrated to the melt directly, rapidly reacting and creating the bubbles.

Finally, we focus on another production method (ML) using direct gas injection. As discussed in the beginning of this section, aluminium without surfactant cannot be foamed, so that additional components have to be added to increase the viscosity of the melt and to decrease the surface-tension coefficient. These additional components can be e.g. Mg with an oxidising gas (it forms an oxide skin at the liquid-gas interface) or SiC particles. The optimal characteristic volume ratio is around 15%, with a particle mean size between 3 and 25 μm . If these requirements are met, gas (argon, air, etc.) can directly be blown in the melt, resulting in a stable foam. As the size and distribution of bubbles inside the matrix strongly depend on the kind of alloy and composite particles, there is a great freedom to modify the morphology.

If all the methods presented above provide a variety of paths to tune the morphology of

foams, none of these methods let us control the morphology *in situ*. The first, most obvious advantage would be to be able, on one production line, with one alloy and one surfactant, to prepare foams with different properties. The second benefit would stem from the enhanced stability of foams with smaller cell sizes, at a given porosity. In particular, Aluinvent has demonstrated the capability to prepare a “castable” foam. When heated above the melting point of its matrix, the cells of the foam remain stable, so that the foam can be shaped/casted to the desired shape.[112] In the next section the action of accoustic pressure on controlling the bubble size *in situ* will be explained in details.

3.2.2 Control of the bubble's size

Here, we propose a breakthrough method to control the size of the bubbles in aluminium foams. It is based on a direct-gas-injection procedure, with a tunable acoustic force acting on the bubble.

Formation of a gas bubble

We consider a situation with a cylindrinical nozzle, pointing upwards and submerged in a liquid. The nozzle can inject gas in the liquid at a controlled-flow rate and pressure. Typically, at low-flow rates, a bubble starts to form at the orifice and grows to a nearly spherical shape before it detaches from the orifice. In figure 3.1, an idealised situation just before detachment of the bubble is depicted. The bubble is considered symmetrical around the vertical axis parallel to the nozzle, and the contact angle of the membrane at the 3-point contact line is $\alpha = 90^\circ$. [113]. At this instant, a simple force balance allows us to predict the characteristic size D of the bubble after detachment. First the buoyancy force F_b , pointing upwards, tends to extract the gas outside of the nozzle:

$$F_b = g(\rho_l - \rho_g) V_b, \quad (3.1)$$

where V_b is the volume of the bubble, $g = 9.81 \text{ m/s}^2$ and ρ_l (ρ_g) is the density of the liquid (gas). In a very good approximation, the bubble is considered spherical so that the buoyancy force can be linked to D , and because $\rho_g \ll \rho_l$, the buoyancy force is $F_b = \frac{\pi}{6} \rho_l g D^3$. Opposed to F_b , interfacial anti-stretching forces act at the neck of the bubble (diameter D_n). The sum of these forces F_t is proportional to the surface tension of the liquid γ :

$$F_t = -L_n \sin(\alpha) \gamma, \quad (3.2)$$

where $L_n = \pi D_n$ is the perimeter of the neck and α the wetting angle. For a liquid wetting the nozzle (this is the case for our experiment with water or aluminium-matrix composite), the diameter of the neck is equal to that of the orifice ($D_n = D_0$). Writing $F_b + F_t = 0$ (instant of

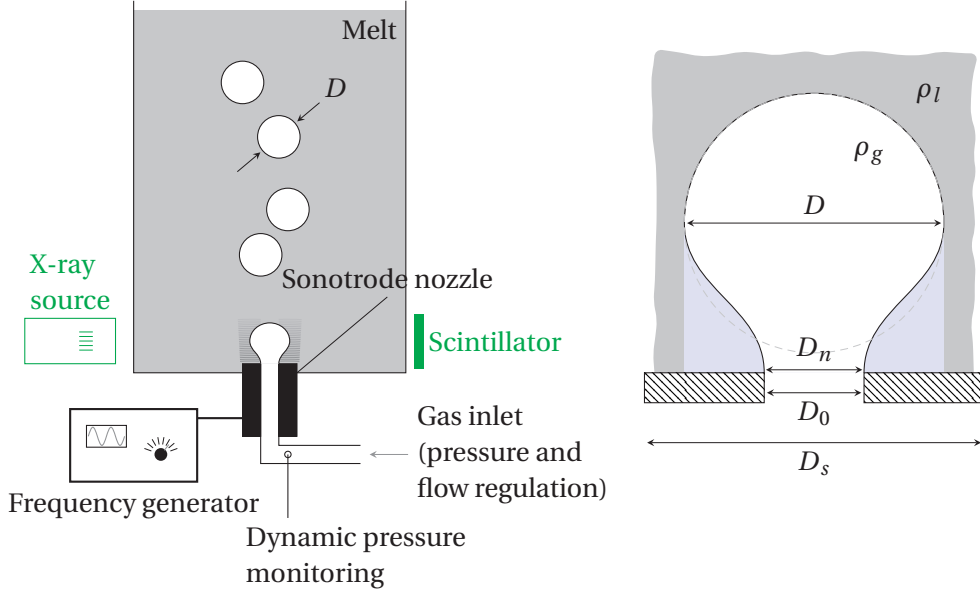


Figure 3.1 – Experimental setup for foaming. A sonotrode nozzle injects the gas inside the liquid (e.g. argon to aluminium melt). The control on the acoustic-radiation pressure is ensured by a frequency generator, controlling the transducer of the sonotrode. For the same gas-flow rate and frequency, the bubbles have a characteristic diameter D . *Left*: magnified view of the formation of a gas bubble (density ρ_g) inside a liquid (ρ_l). D_0 is the diameter of the nozzle, D_n the diameter of the bubble neck and D_{\max} the maximum diameter perpendicular to the gas inlet.

detachment), the characteristic diameter of a bubble is:

$$D^0 = \left(\frac{6\gamma D_0}{g\rho_l} \right)^{\frac{1}{3}}, \quad (3.3)$$

which can be verified experimentally. The superscript “0” denotes the absence of any additional external forces. For an orifice $D_0 = 0.5$ mm submerged in water ($\gamma = 0.072$ J/m² and $\rho_l = 998$ kg/m³), $D^0 = 2.8$ mm, a value perfectly matching experiments (Figure 3.3).

In fact, one can observe in Eq. (3.3) for a given liquid that only D_0 enables control on the size of the bubbles. However, in applications this quantity cannot easily be tuned in-situ, especially in demanding conditions of high-temperature melts. In order to overcome these technological limitations, we introduce an additional force acting on the bubble, promoted by acoustic pressure.

Acoustic pressure

Conveniently, the submerged orifice can be a nozzle combined with a sonotrode device (Figure 3.1), whose vibrating power and frequency can be electronically actuated. As a first approach, let us consider an effective force F_a opposing interfacial anti-stretching, so as to obtain a new balance equation $F_b + F_t + F_a = 0$ at the moment of detachment. In the case of

ultrasonic power applied to the sonotrode, an *acoustic radiation* pressure acts as an additional force on the bubble. It applies on the projection of the surface of the bubble on the nozzle $A_p = \pi(D^2 - D_n^2)$ and can be written as:

$$F_a = p \cdot A_p = p(X) \cdot \pi [D^2(X) - D_n^2], \quad (3.4)$$

where X is the control parameter (e.g. electrical power supplied to the sonotrode), $p = p(X)$ is the reduced-acoustic pressure and $D = D(X)$ is also dependent on the control parameter. Finally, the balance equation for the bubble diameter D in a nozzle-wetting liquid is:

$$g\rho_l D^3 + \frac{3}{2}p(D^2 - D_0^2) - 6D_0\gamma = 0. \quad (3.5)$$

To recover Equation (3.3) without external force, p must fulfill $p(0) = 0$, so that $D(0) = D^0$.

A formulation of $p(X)$ can be made recalling simple concepts. Let $X = P_{el}$ be the electrical power fed to the sonotrode. Then the actual power density transmitted to the medium (liquid) is $I_s = \frac{\eta P_{el}}{A_s}$, where $0.1 < \eta < 1$ is a transmission coefficient and $A_s = \frac{\pi}{4}(D_s^2 - D_n^2)$ is the area of the sonotrode in contact with the liquid and perpendicular to its oscillation direction. The actual pressure reflected¹ on the liquid-gas interface is:

$$p_{ar} = 2 \frac{I_s}{v_s}. \quad (3.6)$$

Here, v_s is the speed of sound in the liquid medium and the factor 2 stems from the complete reflection of the sound wave at the liquid-gas interface, both for water and aluminium.[114, 115] Finally, the reduced acoustic pressure p can be written as:

$$p = k_{eff} \cdot p_{ar} = k_{eff} \cdot \frac{1}{v_s} \cdot \frac{8\eta}{\pi(D_s^2 - D_0^2)} \cdot P_{el} =: b \cdot P_{el}, \quad (3.7)$$

where the only dependence on the liquid type is contained in v_s . The parameter k_{eff} accounts for damping inside the liquid.² For a sphere with large Reynolds number, $k_{eff} \simeq 0.4$. [116]

Experimental realisation

Experiments have been carried out for water³ and an aluminium-matrix-composites melt (Duralcan 20% SiC F3S.20S), where the characteristic size $D(X)$ of the bubbles as a function of the control parameter X were measured. For water, X correspond to a pressure whereas

¹When a sound wave travels through a liquid medium and hits a gaseous bubble, the ratio of the reflected energy density (w_r) to the total energy density (w) can be calculated as $\frac{w_r}{w} = \left(\frac{Z_g - Z_l}{Z_g + Z_l}\right)^2$, with Z_g and Z_l the impedences of the gas and liquid, respectively.[114] For a water/air interface at 298 K, $w_r/w = 0.9989$, while for aluminium/air at 950 K, $w_r/w = 0.99992$. Thus, for both cases more than 99% of the acoustic energy of the liquid is reflected back by the bubble.

²The force associated to a stream has an effective part, represented by k_{eff} .

³In water, bubbles form and drift swiftly towards the surface where they break.

for Duralcan, X is the squared sonotrode power.[117] The sonotrode has a diameter $D_s = 4$ mm and the air-cooled gas injector enables a precise control of the pressure and flow-rate (PID regulation). A 30 kHz Woodpecker UDS-N1 ultrasonic generator and a piezo-electric transducer were employed to pulse acoustic waves through the steel injector.

High-brilliance and high-coherence beam (Swiss Light Source TOMCAT) allows micro- and sub-micro-metre, quantitative, three-dimensional imaging at high frame-rate and extend the traditional absorption imaging technique to edge-enhanced and phase-sensitive measurements. A double crystal multilayer monochromator (DCMM) covers an energy range between 8 and 45 keV. The foaming furnace was placed in front of a 500 μm -thick YAG:Ce scintillator optimized for very fast recordings. The formation of bubbles in the melt has been monitored by pressure measurement and by a PCO Dimax high-speed camera attached to the imaging system of the beamline to capture radioscopy images at 1400fps, 6600fps and 10,000fps. The size of a bubble can be determined in different ways. A first option would be to capture images of the foam and to measure the size of the bubble on the image directly. However, a second, more precise option is to record the dynamic pressure inside the liquid so as to extract the period of the signal, corresponding to the time of formation of a bubble t_b . Knowing the constant gas-flow rate Q and the speed of sound in the medium, the volume of the bubble is determined with precision:

$$V_b = Q \cdot t_b. \quad (3.8)$$

Figure 3.2a shows the measured diameter of the bubbles in Duralcan upon modulation of the sonotrode current. For the aluminium-matrix composite, $\rho_l \simeq 2850 \text{ kg/m}^3$ and Eq. (3.3) permits us to estimate $\gamma \simeq 0.44 \text{ J/m}^2$, a value twice smaller than 0.85 J/m^2 for oxidised aluminium. This value is reasonable if understood as the apparent surface coefficient. It stems from partial coverage of the orifice perimeter due to the presence of the SiC solid particles at the 3-phase line, as demonstrated in Appendix B.

In order to probe the correctness of our model of acoustic pressure, the linearity of p with respect to X can be verified using the following relation by inverting Equation (3.3):

$$p(D) = \frac{2}{3} \cdot \frac{6D_0\gamma - g\rho_l D^3}{D^2 - D_0^2}. \quad (3.9)$$

As seen in Figure 3.2b, the acoustic pressure can be modelled by the form proposed in Equation (3.7). In this manner, the fitting parameter b' provides an estimation for the diameter of the bubble as a function of $p = b'X$.

The bubble diameter D as a function of the reduced acoustic pressure p is shown in Figure 3.3, for water and Duralcan. The fitting line for Duralcan fairly agrees with the experiment. For water, the model reproduces well the form of the temperature dependence (inset of Fig. 3.3), especially at acoustic pressures higher than 0.5 kPa. For lower pressures, there

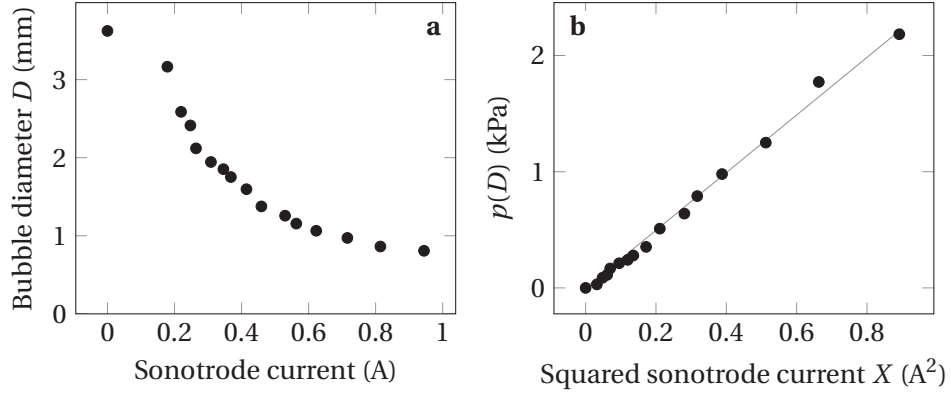


Figure 3.2 – **a** Experimental data collected for the bubble diameter D as a function of the sonotrode current in a melt of Duralcan (20% volume SiC). **b** Equation (3.9) as a function of the squared sonotrode current for the same dataset. p is linear in X , which confirms the model of acoustic pressure (Eq. (3.7)) because $X \propto P_{el}$. The solid line corresponds to $p = b'X$, with $b' = 2.5 \text{ kPa/A}^2$.

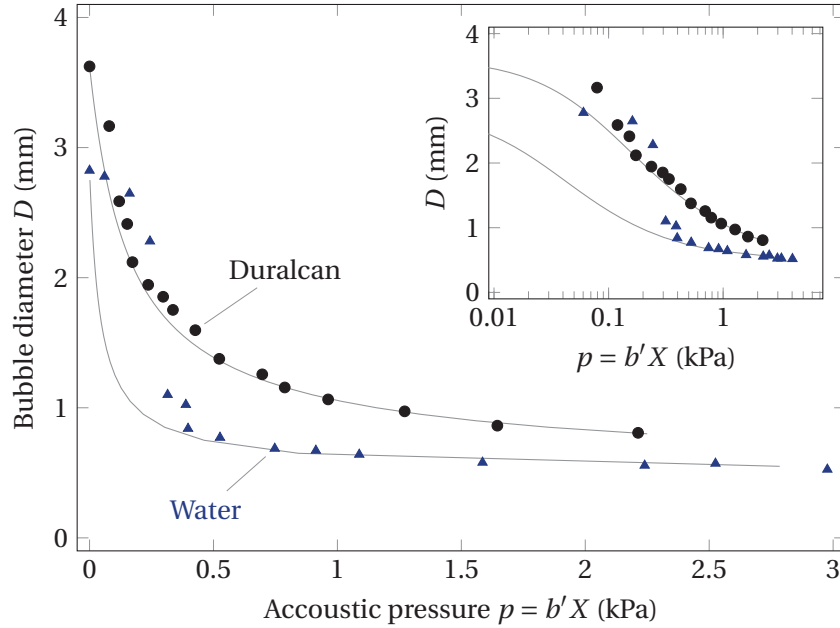


Figure 3.3 – Diameter of the bubble as a function of the (reduced) sonication pressure $b'X$ for water (blue triangles) and aluminium-matrix composite melt (black dots). The solid lines are fits according to equation (3.5). The inset shows the same data in a semi-logarithmic representation, to highlight the presence of an inflexion point in the curves.

is a larger mismatch between the fits and experiments. Whereas for water D rapidly reaches values close to the minimal diameter D_0 upon increasing sonotrode power, there is room for improvement for Duralcan, where larger pressures could be applied to gain several tens of microns.

Applying ultrasonic power to the melt permitted us to control the diameter of bubbles continuously from 3.8 to 1 mm, which has significant implications for fabrication of aluminium foams. First, one can prepare products with customised pore sizes on the same production line, which has obvious cost advantages. Second, materials with custom bubble-diameter patterns can be designed. For example, one could imagine large panels with pores smaller and smaller as they become closer to the surface, a geometry that would favour light-weight and good strength. This could even be more important for sound absorption, where an accurate-controlled distribution of the pores would lead to specific acoustic properties. Thermal-flow control could also be enhanced through alternation of large/small pores.

The beauty of our method is that it is not restricted to aluminium melts or water. Instead it could be virtually applied to a variety of other systems. In fact, the only requirements is to have a foamable phase, viscous enough and with cell walls stable against external perturbations. Knowing the density of the foamable liquid and the diameter of the injector permits an estimate of the span of diameter reachable by this method.

3.3 Microstructure

The microstructure of Al_xSi alloys and Al-MMCs very strongly influences their mechanical, as well as thermo-electric properties. Thus, it is important to characterise our specimen by multiple techniques. In this section, we explore the microstructure of both the matrix (mesoscale) and the porous architecture with optical microscopy, scanning electron microscopy (SEM), electron dispersive spectroscopy (EDX) and x-ray diffraction (XRD). Three specimen provided by Aluinvent were selected for transport studies, with different porosities and compositions. Due to restrictions regarding intellectual property, many details of their fabrication are not shared. Furthermore, our analysis is strictly based on the characterisation provided hereafter.

The three specimen were cut (bars of approximately $8 \times 2 \times 1 \text{ mm}^3$) and polished with gradually finer-grained-SiC sandpapers for inspection, and subsequently cleaned in acetone and ethanol. SEM images were acquired with a Zeiss MERLIN (GEMINI II) microscope; they are composites of in-Lens-detector and secondary-electron images, taken at 3.00 kV at about 2.2 mm working distance. An additional X-MAX silicon-drift-type detector from Oxford Instruments enables energy-dispersive X-ray spectroscopy (EDX) in combination with the AZtec software, yielding an accuracy of about 1%at. The bias applied was 15 kV. The XRD spectra were acquired with a PANanalytical EMPYREAN diffractometer (θ - θ , 240 mm) equipped with a PIXcel-1D detector. The X-ray wavelength was the Cu $K_{\alpha 1}$ emission line ($\lambda = 1.5406 \text{ \AA}$). The average-crystallite size was determined using the Deby-Scherrer relation.[66, 118]

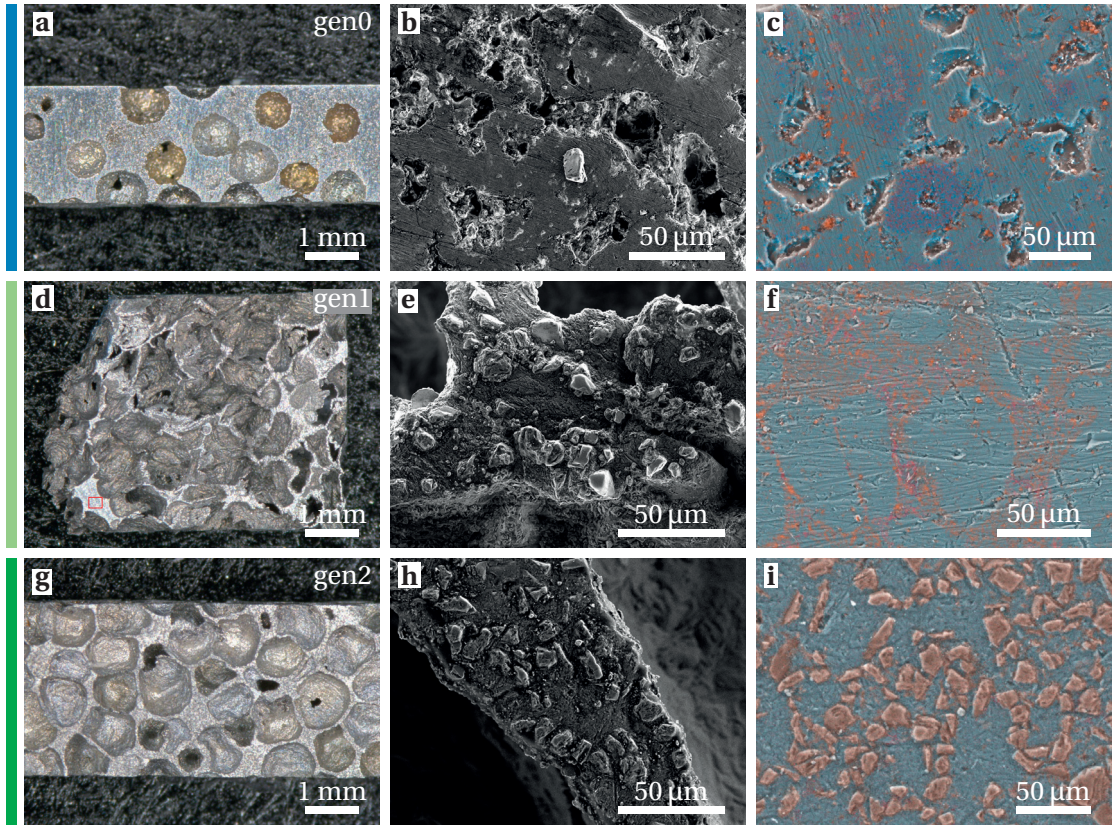


Figure 3.4 – Microstructure and composition of the samples. **a,d,g** Optical micrographs of the specimen shaped for transport measurements. **b,e,h** SEM images (blend of in-Lens and SE2 signals) of the matrix. **c,f,i** EDX color maps of the matrix. Light blue corresponds to aluminium, pale orange to silicon, red to magnesium and dark blue to oxygen. The area scanned in **f** matches the red rectangle in **d**, a portion of the matrix not containing SiC grains. The color bars on the left define the color scheme used in subsequent figures.

Figure 3.4 shows optical and scanning-electron-microscopy (SEM) images of three samples, revealing textured matrices. It can be seen on the optical images that all samples have closed-cell pores of average diameter between 300 and 500 μm , however their distribution varies. From top to bottom, the first foam is an aluminium-silicon-magnesium alloy (Al5Si) alloy without reinforcement particles (we call it *gen0*); the second is a first-generation (*gen1*) foam, with pores of irregular shapes; the third is a second-generation (*gen2*) foam with a better-defined-cell geometry. The low porosity of the first foam is inherent to its composition: without solid particles, the viscosity of the melt permits drainage of the bubbles, hence their relative scarcity. The stability of the bubbles is probably kept by magnesium oxide (MgO) forming at the surface when an oxidising gas (air) is blown. The SEM image (Fig. 3.4b) reveals secondary pores in the matrix, of approximately $30 \pm 10 \mu\text{m}$. They probably are leftovers of bubbles that collapsed during the foaming process. XRD data (Figure 3.5) indicate the presence of pure Al in a fcc phase, as well as Si in a cubic-diamond phase in the matrix, with crystallites of $60 \pm 20 \text{ nm}$. The EDX map for this sample brings to light inhomogeneities at

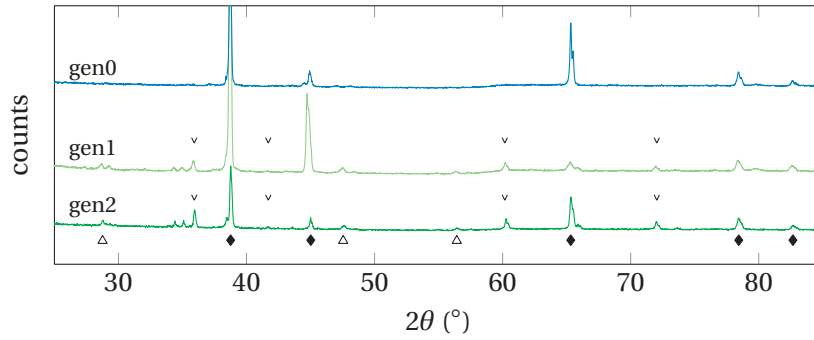


Figure 3.5 – X-ray diffraction patterns of aluminium foams. The diamonds index peaks of Al (fcc) phase, triangles peaks of Si (diamond) and inverted triangles indicate SiC peaks.

Type	EDX %wt				Avg. cell		Solid SiC particles	
	Al	Si	Mg	O	size (μm)	ϕ (%)	%vol	Size (μm)
gen0	78.2	4.6	1.0	16.1	360	39		
gen1	80.3	14.4	1.0	4.3		87	20	10-20
gen2	86.5	13.2	0.3	<1	430	76	20	10-20

Table 3.3 – Composition and structure of aluminium foams. Average-cell size (analysed with ImageJ software), porosity ϕ and size of the solid SiC particles of the foams. The composition was calculated from the averaged signal of a 400 μm² area.

larger scales in the alloys. Small (5 μm) clusters of Si (orange) are embedded in the matrix, and larger regions rich in both Mg and O are visible (dark blue and red).

In Figure 3.4e,h the silicon carbide particles are clearly visible, confirmed by the EDX mapping (Fig. 3.4i) and XRD. They occupy the surface of the cell-wall as well as the matrix. However, for the second sample (gen1), there are zones that do not contain these particles (Fig. 3.4f). This originates from an imperfect mixing when adding the SiC powder during processing. Nonetheless, such area allows us to observe the composition of the original alloy. Two phases are observed: circular domains rich in Al embedded in Si- and Mg- richer matrix. As for the first sample, the second and third samples contain the same Al fcc and Si diamond crystalline phase (crystallites average size: between 30 and 40 nm for the Al phase and 70 ± 20 nm for the Si phase, in both gen1 and gen2). The main difference between the last two specimen is their composition, differing slightly for Si and Mg, and the foaming process leading to different structures. The 2nd generation foam has better mechanical properties (the 1st generation is very brittle), as its structure is less “jagged” (SEM)⁴ and the matrix is more homogeneous (EDX and SEM). Finally, a summary of the compositions and other features of the foams are listed in Table 3.3.

⁴The thin stripes visible at the surface are a consequence of mechanical polishing.

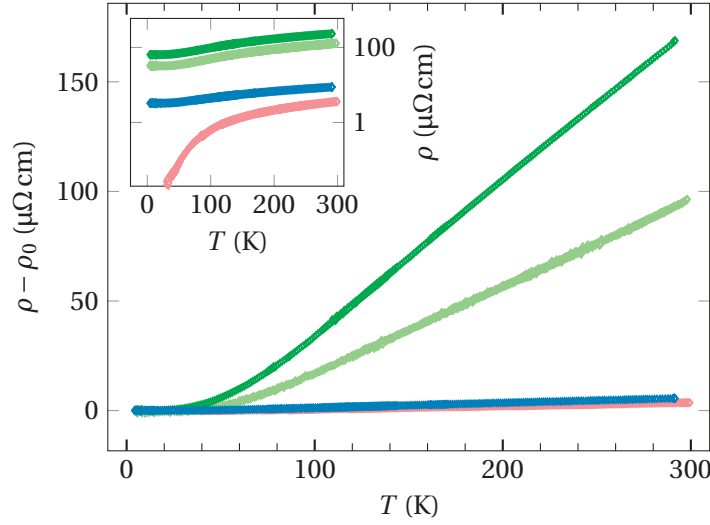


Figure 3.6 – Temperature-dependent electrical resistivity ρ of aluminium foams (orange: Al 5N, blue: gen0, pale green: gen1, dark green: gen2). The residual resistivity ρ_0 has been subtracted to highlight the change of slope, related to the strength of electron-phonon interactions. The total resistivity is presented in the inset.

3.4 Transport properties

3.4.1 Electrical and thermal conductivities

Electrical resistivity of the three foams was measured and the results are reported in the inset of Figure 3.6. First, the temperature dependence of bulk aluminium closely reproduces results found in the literature.[119] For all samples, the absolute value is shifted towards larger resistivities upon increase of the porosity. A detailed study of electronic transport in AlSi alloys with varying amount of Si has been carried by Chevrier *et al.*[120] They found that the electrical conduction was dominated by the fcc-rich aluminum phase. Similarly to their analysis, the thermal part of the resistivity ($\rho - \rho_0$) can be modelled by the Bloch-Grüneisen formula (Eq. (1.24)) giving a Debye temperature of 400 K for all samples, and thus confirming that the electronic transport is dominated by the aluminium phase in the foams.

In pure metals, thermal conductivity is largely dominated by the electronic part κ_{el} , so that conduction via phonons can be neglected and κ can be estimated from resistivity measurements using the Wiedemann-Franz law (WFL, Equation (1.19)), at high temperatures. For metallic alloys, the situation changes. First, disorder inherent to the addition of alloying elements favours the scattering of charge carriers. As a result, the residual resistivity ρ_0 increases, depleting κ_{el} . The lattice thermal conductivity κ_{ph} consequently occupies a more important part in the total κ . Therefore, as the portion of alloying element(s) grows, the WFL becomes inaccurate to describe the total κ . Furthermore, the electronic and thermal properties of alloys strongly depends on their synthesis. The formation of secondary phases, precipitates, grains or amorphous domains has consequences on the transport.

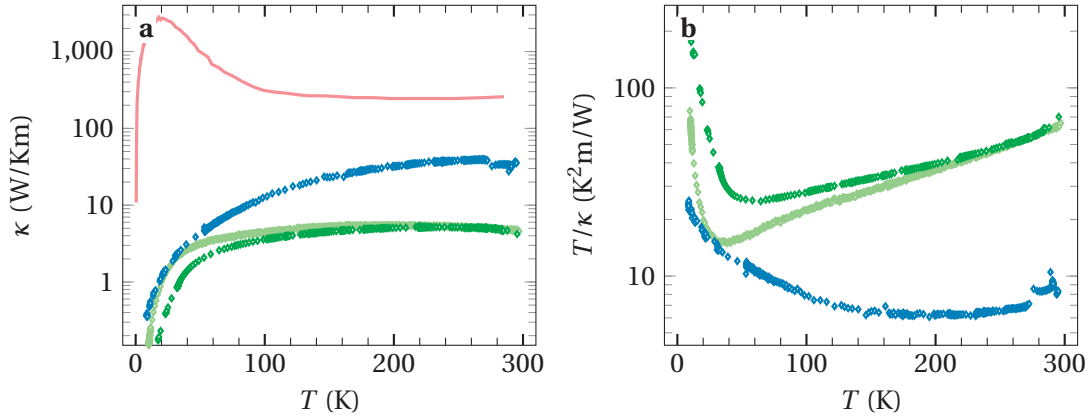


Figure 3.7 – **a** Temperature-dependent thermal conductivity of aluminium foams (orange: Al 5N, blue: gen0, pale green: gen1, dark green: gen2). **b** Unified thermal resistivity T/κ for the three foams. The curve for pure aluminium is reproduced from Ref. 121.

Figure 3.7 shows the temperature-dependent thermal conductivity $\kappa(T)$ of three aluminium foams, compared to bulk aluminium (5N purity). Compared to bulk, κ of the foams is damped significantly on the whole temperature range. In particular, the low-temperature peak is completely erased. The low-temperature dependence of κ of the foams does not follow a T^3 power law, a sign of high disorder that corresponds well to the micro-structure. In very pure aluminium the electron- and phonon- mean-free path are limited only by dilute impurities and grain boundaries, respectively. In alloys, the texture of the matrix (grain boundaries, different crystal orientation, precipitates, exogenous particles, pore walls) strongly shortens the electron mean-free path and destroys long-range order, thus promoting phonon-phonon scattering. The room-temperature value of the gen1 and gen2 foams are two orders of magnitude below that of pure aluminium. This shift down can be partially explained by disorder, introduction of SiC particles and porosity respectively; however, it is cumbersome to distinguish the relative magnitude of these effects, except for the effect of the porosity (see next section).

In theory, the electronic contribution to the thermal conductivity κ_{el} could be calculated from the Wiedemann-Franz law. However, a quantitative analysis is difficult because of the large error on the geometrical factor for both thermal and electrical conductivities. Indeed, the size of the pores ($\approx 400 \mu\text{m}$), comparable to that of the specimen (a few millimetres) adds “border effects”. To avoid these effects, the specimen should have larger sizes. Nonetheless, one can observe, qualitatively, that the Lorenz ratio $L_e = \rho\kappa/T$ deviates from a linear behaviour as the temperature decreases. This is expected for alloys,[18, p. 152] but raises questions of the relative magnitude of κ_{ph} in the total thermal conductivity. κ_{ph} was calculated for pure aluminium at low temperatures and was found to be around 1 W/Km at 20K.[122] For impure aluminium, κ_{ph} should be lower than this value because of phonon-scattering by impurities (Si and grain boundaries), but still weight in the balance against κ_{el} that is also much lower in the alloys than in pure aluminium. The unified thermal resistivity (T/κ) is

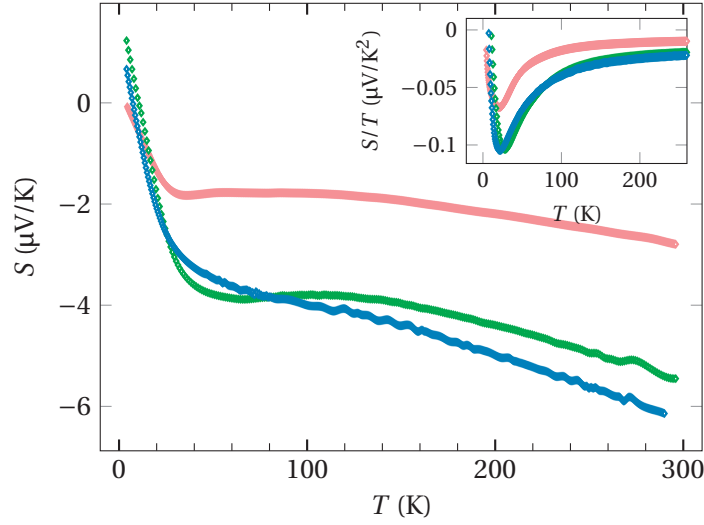


Figure 3.8 – Temperature-dependent thermoelectric power S of aluminium foams (orange: Al 5N, blue: gen0, dark green: gen2). The quantity S/T is shown in the inset.

shown on Figure 3.6b. This quantity should be equal to ρ/L_0 if the WFL is respected. One can observe that the behaviour of T/κ is similar to that of ρ , at high temperatures. However, below 50 K there is a sharp upturn for the 1st and 2st gen. foams, indicating an abrupt deviation from the WFL. This upturn is present in the gen0 foam, but is smoother and occurs at higher temperatures, a characteristic of amorphous systems. The complex structure of the foams and the experimental error makes it very delicate to distinguish the contribution to thermal conductivity by charge carriers and phonons, so that little can be said about the lattice thermal conductivity of the foams. Whereas for ρ , the transport is mainly governed by the Al phase, the picture is different for κ . As κ of Si has values comparable to that of Al, Si precipitates also contribute to the thermal transport.[123]

3.4.2 Seebeck coefficient

The thermoelectric power S for bulk aluminium and two foams (gen0 and gen2) is shown in Figure 3.8. The temperature dependence as well as the absolute value of S of pure aluminium agree with previous reports[124]. The peak in the absolute value of S around 30 K (Al) and 50 K foams could be associated to phonon-drag. In the two aluminium foams, S is enhanced by a factor ~ 2 above 50 K with respect to pure Al. This could be due to a carrier-scattering mechanism (in this case electron-phonon) occurring in presence of the Si precipitates or SiC particles. The right-hand term of Equation 1.27 could account for this contribution to S , adding to the S_{Al} . Notably, both foams have a very similar temperature dependence and magnitude of S . This strengthens this hypothesis, because the foams have different morphologies, but a very close content in Si. We expect that S should not be modified by the presence of the bubbles or different morphologies, because S is an intensive quantity.

3.4.3 Effect of the porosity

Using simple considerations, we are able to assess the part of the resistivity (thermal conductivity) due to the absence of material in the pores. The behaviour of effective parameters in disordered systems has been widely studied, including the case of random resistor networks. Our foams can be viewed as such systems, both for electrical and thermal conductivity. The effective parameter is the measured one, and the reference is the bulk value, when the porosity equals zero. Then, the ratio of the effective to reference values for large porosities is equal to $(1 - \phi)^t$, with t an universal exponent. Away for the percolation threshold (≈ 0), the same ratio is equal to $1 - \phi$. For three-dimensional systems, t was predicted to be between 1.5 and 1.6.[95] Numerous studies of aluminium foams have systematically evaluated these relations for both electrical and thermal conductivity at room temperature, and found that $t = 1.5$ for these systems.[96–102] The conditions for such scaling laws to be valid are that the mean-free paths are much shorter than the shortest-characteristic size in the system. This is the case in our foams, as we estimate the electron-mean-free path $\rho \cdot l_e = \frac{m_e v_F}{ne^2} = 40 \mu\Omega\text{cm}\cdot\text{nm}$ [125] to attain a maximal value of 30 nm. Not surprisingly this value compares with the size of the crystallites of the aluminium-rich phase. This value of 30 nm is much smaller than the cell-wall thickness of 50 μm (Fig. 3.4), for the temperature-range considered so that, for high porosities, $\bar{\rho}(T) = \rho(T) \cdot (1 - \phi)^t$ and $\bar{\kappa}(T) = \kappa(T) \cdot (1 - \phi)^{-t}$, where the bar stands for the property of the matrix. The correction factors for the conductivities are 0.61, 0.047 and 0.12 for gen0, gen1 and gen3 respectively. Even though there is a significant change in absolute value between the effective and matrix properties, there is no qualitative change in the discussion of the last section.⁵

The same reasoning could even be pushed further in presence of SiC particles. For electrical resistivity, they can be considered as of infinite resistance compared to that of the aluminium alloy ($\rho_{\text{SiC}} \gg \rho_{\text{AlSi}}$). It is equivalent to having the alloy matrix with additional holes instead of the SiC particles. For thermal conductivity, one must be careful because the limit of high contrasts (in κ) is not respected any more.

3.5 Conclusions

We have explored two very important aspects of aluminium alloys foams. First we established a method to modify the size and distribution of cells in metallic melts *in situ*. We derived a theoretical model to explain the effect of acoustic pressure on the reduction of cell's sizes and we compared this model to experiments made in water and SiC-reinforced aluminium-alloy melt. Second, we studied the low-temperature thermo-electric properties of three aluminium foams from different syntheses. A strong decrease of thermal conductivity as well as an increase in electrical conductivity were simultaneously observed. Owing to the fairly complex structure of the system, containing crystalline metallic grains, precipitates, pores and SiC

⁵Note that we neglect thermal transport via radiations from the cell walls. It is a reasonable assumption because κ of the matrix is high enough.[126]

particles altogether, the respective contributions of these elements are hard to disentangle. In order to have a more accurate interpretation of the thermo-electric properties, it would be beneficial to have measurements of the compact material (without pores) and of the alloy without SiC particles. Moreover, a systematic study of κ of bulk aluminium alloys containing varying amount of Si or Mg would help to assess the influence of these elements on the heat transport.

The successful modifications of the thermoelectric properties of metallic foam by foaming supports a current strategies to texture a medium in order to improve the delicate balance between the thermoelectric coefficients.[127] In the case of our foams, the size of the smallest “neck” for electrons and phonons is the wall thickness, and it is well above the mean-free- paths of both electrons and phonons, thus the foamy structure is not interacting independently with either. Nevertheless, if one could synthesise foams with thinner cell walls, the door would be open for interesting modifications of the thermoelectric properties. For example, if the electron mean-free path were shorter than the phonon-mean-free path, so that phonons would be heavily scattered at cell walls, but not electrons, there would be a net benefit in the thermoelectric figure of merit ZT . This would be possible because we observed that S does not change significantly between different structures. We believe that this route could be transferred to other alloys more promising for thermoelectric applications, such as half-Heusler alloys, bismuth-telluride compounds or $\text{Si}_x\text{Ge}_{1-x}$.

4 Heat transport in functional oxides

Solid oxides represent a very extensive family of materials and their utilisation spans all fields of applications. Usually stable in atmospheric conditions and sustaining high temperatures, they also have appealing mechanical properties. Perhaps the most common oxide we daily encounter is silicon dioxide (SiO_2). Quartz is the crystalline form of SiO_2 found in nature, and glassware is composed of an amorphous phase of SiO_2 , with a little amount of impurities added (e.g. sodium). The optical transparency of quartz witnesses a large band-gap and correlates with very low electrical conductivity. Beyond SiO_2 , the case of more complex oxides offers a variety of interesting phenomena. For example, the category of copper oxides (cuprates) displays high-temperature superconductivity or good thermoelectric properties. Substitution of elements by chemical doping permits an enlarged range of physical effects.

If increasing structural complexity entails beautiful and surprising physical phenomena, there exist simple compositions that are the ground for intriguing physics, and more importantly for very valuable applications. This is the case of titanium dioxide (TiO_2), that will attract our focus in this chapter. Next, looking for other polaronic materials with interesting thermoelectric properties, another oxide, mayenite ($12\text{CaO}\cdot 7\text{Al}_2\text{O}_3$), with a simple composition yet more complex structure will also be discussed.

4.1 Titanium dioxide

Titanium dioxide is found in Nature in three polymorphs: rutile, anatase and brookite (Figure 4.1). Rutile has the smallest unit cell (Fig. 4.1a) of the three and it is also the most thermodynamically stable phase of TiO_2 , hence it is also the most common in its bulk form. A natural-rutile gem is displayed in Figure 4.1c. The other most important polymorph is anatase, a phase that is found in nanostructured forms of TiO_2 , like nanowires or nanoparticles.

As titanium is the ninth most abundant material on Earth,[128] and because it is found in nature in oxidised forms, TiO_2 is available world-wide in large quantities, making it commercially attractive. One of its firstly recognised property was its high reflective index and

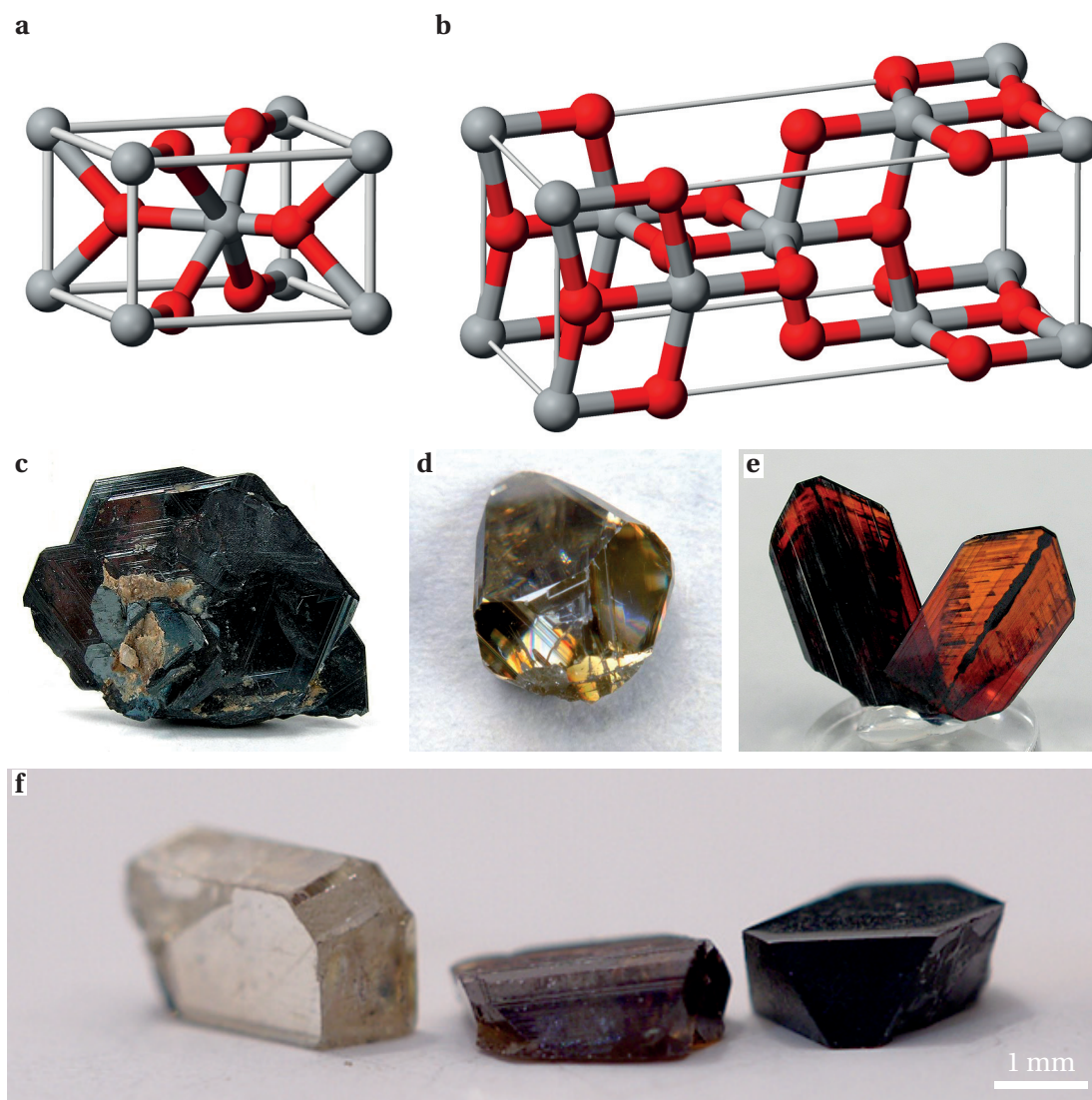


Figure 4.1 – Polymorphs of titanium dioxide. Ball-and-stick model of unit cells of **a** rutile and **b** anatase TiO_2 (grey: Ti and red: O). Optical image of **c** a rutile gem, **d** a synthetic single-crystal of anatase and **e** a brookite gem. **f** Three specimen of synthetic anatase TiO_2 containing different amount of oxygen vacancies, from the pristine (left) to H-reduced one (right). Image credit: **a-d** Wikimedia common, **e** Rob Lavinsky/iRocks.com.

capability to absorb UV-light. Therefore titanium dioxide is used intensively in industry as a white pigment. The white TiO_2 pigments enter in the composition of paints, as well as in the food and cosmetic sector, (gummy candies or toothpastes). As the pigments absorb UV-light very efficiently, they also are active ingredients of sun-screens.

In addition to these “basic” yet important applications, TiO_2 provides a wide spectrum of functionalities, allowed by a variety of different architectures at nanoscales.[129] In particular, photo-catalytic activity of thin TiO_2 coatings proves antibacterial action and self-cleaning properties.[130–132] These features can also be achieved when titanate nanowires are arranged into a fibrous network, thus providing an enhanced filtering with significant potential for water and air purification.[133,134] Moreover, nanoparticles of TiO_2 contribute to good performances of solar-cells regarding the collection of photo-induced charges.[135] For Niobium-doped TiO_2 a high power-factor was reported which places this material among promising thermoelectric converters.[136] Besides energy and environment oriented applications, TiO_2 nano-structures achieved humidity sensing,[137] they were employed to reinforce polystyrene composites[138] and are foreseen as central elements of non-volatile memories (memristors).[139] Most of the beneficial characteristics of TiO_2 stem from the anatase phase of the material. While thermal conductivity of rutile was measured decades ago ($\kappa = 8 \text{ W/Km}$ at room-temperature),[29] the same quantity for bulk-anatase crystals or titanate nanowires remains largely unexplored, mainly due to difficulties in synthesis.

4.2 Anatase single-crystals

4.2.1 Synthesis

Figure 4.1f shows the broad range of anatase-phased samples for which thermal conductivity is reported in Section 4.3. The large, millimetres-long single-crystals (SC) on Fig. 4.1f are unique for anatase in which growth our laboratory is specialized. They were grown by chemical-vapour transport.[140,141] Anatase powder of high purity (less than 300 ppm of Al detected) and powder of NH_4Cl (transport agent) were sealed in a quartz tube in argon gas. The 3 mm-thick, 2 cm-wide and 20 cm-long ampoule was placed in a horizontal tubular furnace, and the temperature at its ends were set to 740°C and 610°C . After two weeks, crystals of a few cubic millimetres were grown on the cooler side of the ampoule. The prepared samples are brown (center of Fig. 4.1f), signalling the presence of impurities, while other transparent-stoichiometric samples are colourless with a band gap of 3.2 eV (Fig. 4.1d and left of Fig. 4.1f).

4.2.2 Oxygen vacancies

The very rich defect chemistry in TiO_2 has been studied in details, numerically and experimentally. In particular, one type of defects have attracted our attention. Oxygen vacancies in anatase are known to have a strong influence on the optical and electronic properties of this material.[142]

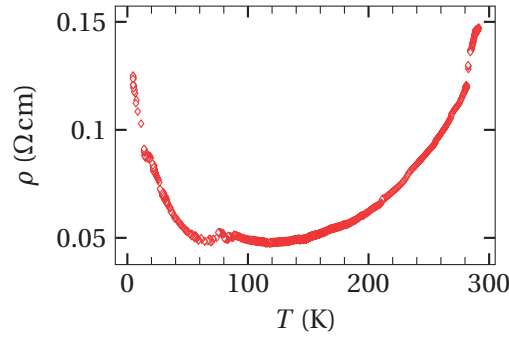


Figure 4.2 – Temperature-dependent resistivity of conducting (black) anatase TiO_2 .

One can easily vary the oxygen stoichiometry, from the pristine SC (transparent) on the left of Fig. 4.1f, towards the increased concentration of oxygen vacancies (brown and black) achieved by heat treatment in a hydrogen-rich atmosphere. Several specimens of anatase crystals grown by the method described in the last section were placed in a silica glass tube and inserted into an electric tubular furnace and heated under hydrogen at 650°C for several hours. The black SC on the right, from the pristine, 3.2 eV gapped semiconductor, evolved towards a semi-metallic sample due to shallow-donor levels introduced by the off-stoichiometry.[140,143] The energetic states induced by such treatment are circa 100 meV below the conduction band,[134,142] resulting in two observed effects: the crystals change their colour to dark blue, almost black (right of Fig. 4.1f) and electrical resistivity drops to $1\ \Omega\text{cm}$ at room-temperature. The electrical resistivity measurements (Figure 4.2) show that such material has metallic character down to 60 K when it starts to behave as insulator, in agreement with earlier findings.[143,144] This situation is different from the case of the brown sample, where, from the energy point of view, the electrons are localized deep in the band gap and do not contribute to the electrical conductivity. This is confirmed by the measured electrical resistivity of $10^{12}\ \Omega\text{cm}$ at room-temperature.

To provide a precise identification of defect densities in our different TiO_{2-x} single-crystals and in the anatase as-grown foam, we performed high-precision, low-temperature electron paramagnetic resonance (EPR) studies. EPR is a readily applicable technique for the determination of concentration of paramagnetic centers even below ppm levels.[145–147] In the study of the structure of TiO_2 defects, EPR evolved to be an essential tool due to its high sensitivity to local-crystal environments and low concentrations, its versatility, and its capability to differentiate bulk and surface states.[148–152] Electron paramagnetic resonance (EPR) at 9.4 GHz microwave frequency was performed on a Bruker X-band spectrometer. A conventional field modulation technique was employed with lock-in detection, providing the first derivative of the EPR-absorption spectra. The EPR intensity was calibrated with $\text{CuSO}_4 \cdot 5\text{H}_2\text{O}$ reference samples. The EPR intensity of each signal component is determined both by double integration of the EPR signal and by fitting the (derivative) Lorentzian curves, as is customary in the electron spin resonance-related literature.

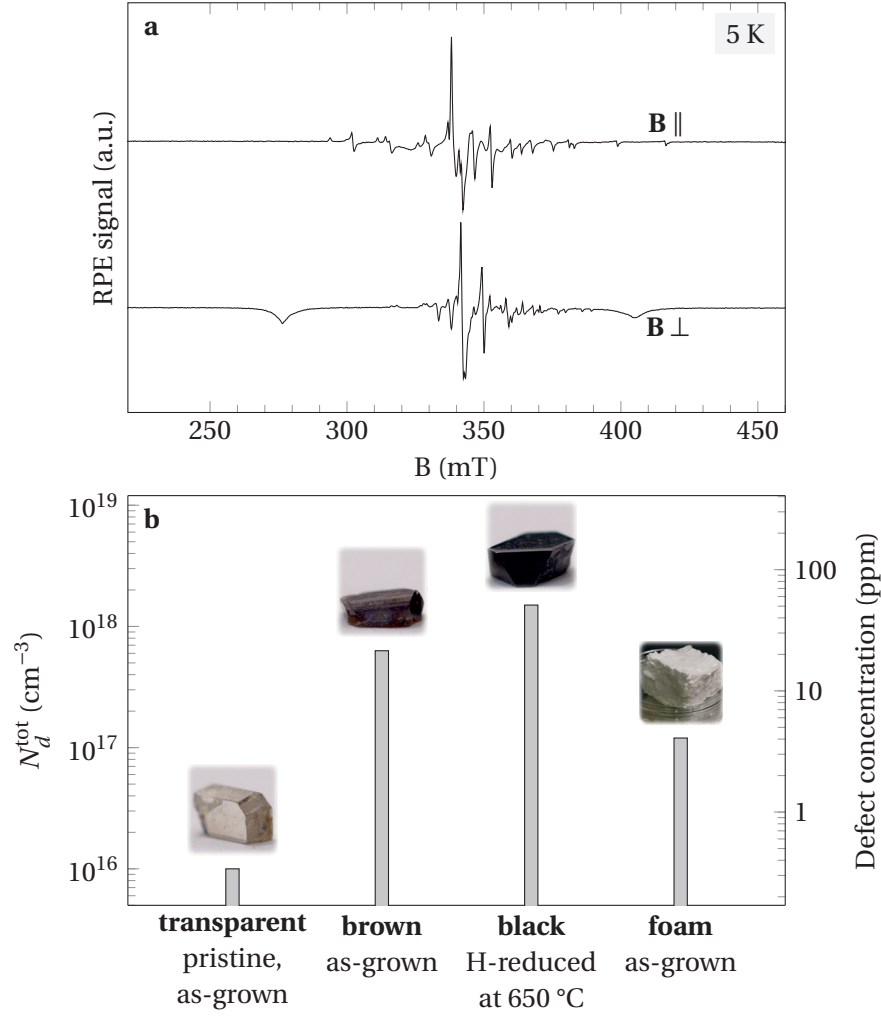


Figure 4.3 – **a** RPE signal for the black anatase single-crystal at 5 K for different orientations of the magnetic field **B**. **b** Summary of the defect concentrations of the three single-crystals of anatase and the anatase foam.

As presented in Figure 4.3a in the case of our black single-crystal, EPR spectra of our TiO_{2-x} crystals exhibit a combination of different spin-1/2 defects. The different g -factors of the measured defects reveal that these are placed in a distribution of crystal environments corresponding to slightly different crystal fields in the single-crystal structure. Angle dependence of the measured-EPR spectra highlights that all these defects are in well-defined positions in the structure. In addition, given that all spectral components have strong angle dependence, we can provide a further proof of the absence of small grains in the structure.

In addition, EPR linewidth (ΔB_{pp}) of all homogeneously broadened components remains small in all samples. This yields a first confirmation of the small local density, and that all defect types are sufficiently distributed in these materials. From the temperature dependence of the EPR intensity (not shown), we can clearly identify that all defects show Curie-temperature

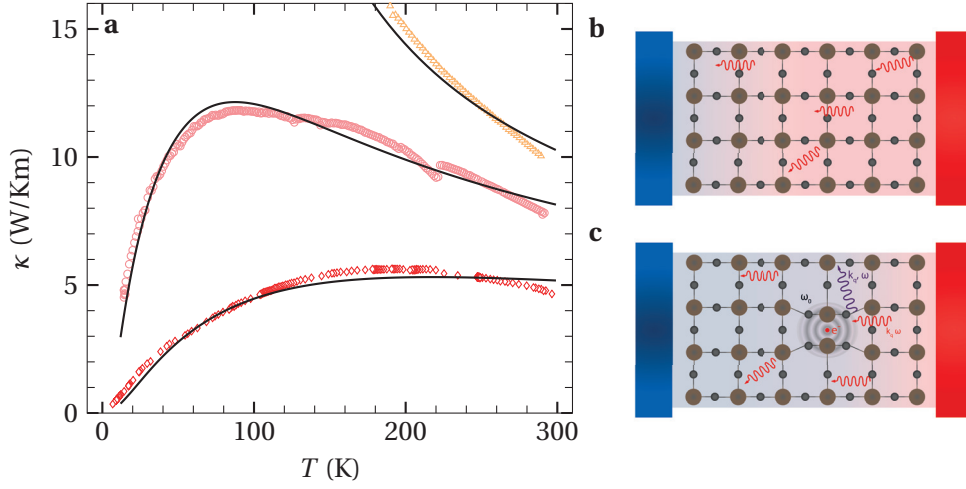


Figure 4.4 – **a** Temperature dependence of the thermal conductivity of insulating-transparent, -brown and conducting-black anatase TiO_2 single-crystals, respectively from higher to lower κ . The solid lines are fits of κ including the resonant-dynamical-scattering term. Sketches of the difference between heat propagation in **b** pristine single-crystal and in **c** crystal with oxygen vacancies. Only one vacancy is displayed with an electron localized in its surrounding. Such defects exhibit strong polaronic effects, which heavily scatter phonons and reduce κ . The colour gradients from red to blue illustrate temperature differences across the material.

dependence at the lowest temperatures. Nevertheless, polaronic diffusion of defects at higher temperatures leads to a sudden drop of the EPR intensity.

To precisely calculate the defect density of our samples, we complementarily applied double integration and fitting procedures to verify that the total-defect density is taken into account. In Figure 4.3b, the calculated total-defect densities are shown for anatase TiO_{2-x} single-crystals and for the anatase as-grown foam.[130] They vary from 0.34, 21 to 51 ppm for the transparent, brown and black crystals, respectively.

4.3 Thermal conductivity

Thermal conductivity of all specimens were acquired from 10 K to 300 K using the steady-state method described in Reference 153 and in the Appendix A.2. Experimental error at 300 K is 15%, and decreases with lowering temperature as the black body radiation contribution diminishes. The three curves in Figure 4.4 correspond to the crystals displayed in Fig. 4.1f, from the top κ of the transparent crystal and below with an increasing amount of oxygen vacancies.

4.3.1 Low intrinsic thermal conductivity

For a material with such a simple composition as TiO_2 , it is a surprise to find low intrinsic values of κ in the brown and black crystals, not only at room temperature ($\kappa = 5 \text{ W/Km}$),

4.3. Thermal conductivity

TiO ₂	a_C (s ⁻¹)	a_R (s ³)	a_U (K ⁻¹ s)	θ_D (K)	T_U (K)	a_p (s ⁻¹)	ω_1 (K)	ω_2 (K)	α
black	$1.14 \cdot 10^{10}$	616	$5.01 \cdot 10^4$	1000	600	--	--	--	--
brown	$5.02 \cdot 10^8$	616	$5.01 \cdot 10^4$	1000	600	--	--	--	--
black ^r	$4.56 \cdot 10^6$	228	$2.29 \cdot 10^4$	900	170	$39.8 \cdot 10^8$	191	89.7	2.76
brown ^r	$4.56 \cdot 10^6$	228	$2.29 \cdot 10^4$	900	170	$3.63 \cdot 10^8$	191	89.7	2.76
transp.	$4.56 \cdot 10^6$	228	$2.29 \cdot 10^4$	900	170	0	--	--	--
F-doped	$4.56 \cdot 10^6$	6156	$2.29 \cdot 10^4$	900	170	$16.9 \cdot 10^8$	41	--	--

Table 4.1 – Model parameters in Eq. (1.36) and (4.11) obtained by two fitting procedures (without and with resonant scattering in Callaway’s formula), for the conducting (black) and insulating (brown) anatase SCs. With resonant scattering, only a_p , the parameter proportional to the concentration of defects, varies between the different SCs.

but also over the whole temperature dependence. Thurber and Mante reported, more than fifty years ago, thermal conductivity of rutile SCs. For their pristine sample, they found $\kappa(300 \text{ K}) \approx 12 \text{ W/Km}$, whereas for their hydrogen-reduced samples this value reached 9 W/Km , a magnitude similar to that of the anatase pristine (transparent) single crystal (10 W/Km).

The significantly higher value of κ for the more insulating crystals with respect to the semi-metallic one indicates that the itinerant charge carriers are not the main heat transporters. Using the Wiedemann-Franz law, even for the most electrically-conducting crystal (the black SC), the electronic part κ_{el} is at the level of 10^{-3} W/Km , a negligible fraction of the total κ at room-temperature (5 W/Km). Consequently, heat is propagated almost entirely by the phonon subsystem in all anatase SCs.

At the first glance, it might be expected that a reason for the low κ arises from phonon scattering on impurities. Such impurities, in our case, would be oxygen vacancies, ostensibly the only characteristics defining differences between the three anatase SCs. In order to evaluate this idea, we attempt to model the three curves of Figure 4.4 with the Callaway formula in Eq. (1.36), embracing three “conventional” scattering mechanisms (Casimir-, Rayleigh- and Umklapp- scattering), including scattering on static, dilute impurities. Such procedures leads to the parameters’ values referred as “standard” in Table 4.1. For the black crystal, the corresponding fitting curve is shown in Figure 4.5 (dashed line) and it appears reasonably close to the experimental data. However, a closer look at the fitting parameters reveals unexpected – and unphysical – values. The Casimir scattering time $\tau_C^{-1} = v_s/L$ can be estimated from the average speed of sound $v_s = 7 \cdot 10^3 \text{ ms}^{-1}$ in anatase[154] and the characteristic size of our SCs is $L \approx 10^{-2} \text{ m}$. This order-of-magnitude estimate for the Casimir scattering rate gives $\tau_C^{-1} = a_C \approx 7 \cdot 10^6 \text{ s}^{-1}$, a value falling three orders of magnitude behind $1.14 \cdot 10^{10}$, the value obtained from fitting. An additional problem originates from the characteristic energy where phonon-phonon scattering is activated T_U , high compared to other oxide compounds.

These inconsistencies clearly indicate the existence of an additional mechanism for phonon-scattering. Recent progresses in ab initio calculations[26] involving non-perturbative-

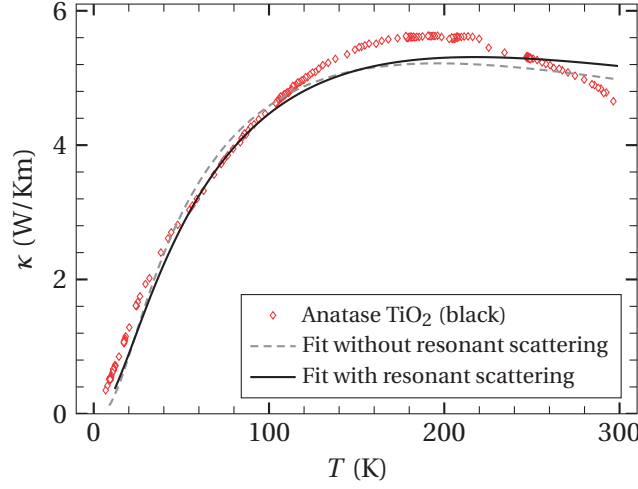


Figure 4.5 – Visual comparison between fits with or without resonant scattering. The difference is - apparently - minute, however the fit without resonant scattering yields unphysical parameters.

microscopic treatment of static defects and lattice-elastic-constant variances around these defects[155] have shown that perturbative approaches can significantly underestimate the scattering rates of low-frequency phonons for systems involving large mass variances. In particular, calculations for pristine FeSi,[156] silicon carbide,[157] and diamond[158] systems show that static defects can account for a reduction of the thermal conductivity (< 300 K) by more than one order of magnitude, when the concentration of defects exceeds 1%. In comparison, the concentrations of defects in our SCs attain five tenth of ppm at most, for a tangible modification of κ .

4.3.2 Polaronic defects coupled to crystalline phonons

In the quest for identifying an extra contribution to phonon-scattering, we have to recall that in anatase the Ti-O are dominantly ionic bonds,[159,160] which is underlined by a large difference between static and optical dielectric constants, $\epsilon_0 \gg \epsilon_\infty$. [161] Therefore, the presence of an excess charge in such a medium can significantly affect the surrounding lattice polarization (deformation), particularly in the limit of low concentration of itinerant charge carriers, when screening is weak (even for the electrically conducting SC).[162] Density functional theory (DFT) calculations found a diversity of band-gap states and resonances in anatase TiO₂ (bulk and surfaces), for various impurities and intrinsic defects.[163–167] In particular, polaronic defects related to charged oxygen vacancies in anatase have been reported both theoretically[168–171] and experimentally.[140,172]

Oxygen vacancies in anatase TiO₂ coincide with charged states deep in the semiconducting gap, provoking a significant local rearrangement of atoms.[167,168,170,171,173,174] This indicates a strong local polaronic coupling between the lattice degrees of freedom around the vacancy site and the charge in excess. The large binding energy (≈ 0.3 eV) of such polaronic

defects in the gap[171] preserves their stability against low-energy excitations (local phonon modes). In addition, optical transitions to delocalized states of the charge in excess, requiring higher energies (≈ 1 eV), [171] can be neglected at low temperature ($k_B T \lesssim 30$ meV). Within such approximation, the excess charge always remains in its ground state that can change adiabatically (almost instantaneously), accommodating to the motion of atoms near the vacant site. Such local charge fluctuations $\delta\rho$, correlated with the vibrations of the lattice, are responsible for the adiabatic renormalisation of local phonon modes.[175] Integrating out the degrees of freedom regarding the charge, an effective potential for the motion of atoms $U(\nu)$ is obtained, where ν are the local atom displacements associated with the defect, $\nu \sim \delta\rho$. The minimum of U corresponds to the equilibrium charge and atomic configuration of the polaronic defect ($\nu = 0$), whereas the second derivatives of the potential define adiabatically renormalized frequencies of the local phonon modes.[175]

While the internal dynamics of the polaronic defects is characterised by the strong binding between the lattice and charge degrees of freedom around the vacancy site, the excess charge interacts on a weaker scale with crystalline phonons as well. In the absence of screening, this latter electron-phonon interaction may be long-ranged; it is indeed the case in anatase TiO_2 , a polar crystal.[176] To the leading order, the interaction between the polaronic defects at positions \mathbf{r}_j and crystalline phonons at positions \mathbf{R}_n is given by a bilinear form of the interaction-Hamiltonian:

$$H_{int} = - \sum_{j,n} \lambda(\mathbf{r}_j - \mathbf{R}_n) v_j Q_n, \quad (4.1)$$

where Q_n are the (crystalline) phonon displacement coordinates, v_j the displacement coordinates that characterise the internal dynamics of polaronic defects. The strength of interaction is given by $\lambda(\mathbf{r}_j - \mathbf{R}_n)$, fading with the distance $\mathbf{r}_j - \mathbf{R}_n$. For clarity, in Eq. (4.1) only a single degree of freedom per polaronic defect is assumed, coupled to a single branch of phonons; however, this coupling can be generalized to multiple degrees of freedom per defect and multiple phonon branches and polarizations. The equations of motion of the lattice with polaronic defects therefore yield:

$$M \ddot{Q}_n = - \sum_m K_{n,m} Q_m + \overbrace{\sum_j \lambda(\mathbf{r}_j - \mathbf{R}_n) v_j}^{\text{external force for the lattice}} \quad (4.2)$$

$$m_p \ddot{v}_j = - \frac{\partial U(v_j)}{\partial v_j} + \underbrace{\sum_m \lambda(\mathbf{r}_j - \mathbf{R}_m) Q_m}_{\text{external force for the defect}}, \quad (4.3)$$

with M and m_p the reduced masses characterising phonons and defects, respectively. $K_{n,m}$ are elastic constants of the crystalline lattice. In Eq. (4.3), phonons act as an external force field on defects. The motion of v_j is solved within the standard linear response theory: $v_j(t) \approx R(\omega) \cdot \sum_m \lambda(\mathbf{r}_j - \mathbf{R}_m) Q_k e^{i(\mathbf{k}\mathbf{R}_m - \omega t)}$, where $R(\omega)$ is the frequency-dependent-defect-

response function to the external force caused by the phonon mode \mathbf{k} with frequency ω . $R(\omega)$ depends on the kind of defect involved, exhibiting resonant behaviors at frequencies of internal-mode excitations. With ε_n and $|n\rangle$ denoting the eigenenergies and eigenstates of the defect, the response function is given by

$$R(\omega) = \frac{2}{\hbar} \sum_{n,m} e^{\beta(\Omega - \varepsilon_n)} |\langle n | \hat{v} | m \rangle|^2 \frac{(\varepsilon_m - \varepsilon_n)}{(\varepsilon_m - \varepsilon_n)^2 - (\omega + i\eta)^2}, \quad (4.4)$$

where $\langle n | \hat{v} | m \rangle$ are the matrix elements of the displacement operator for the defect, $e^{-\beta\Omega}$ is the defect partition function, and $\eta \rightarrow 0^+$.

Now, because $v(t) \sim e^{-i\omega t}$, the action of polaronic defects on the crystal-lattice vibrations can be re-written in terms of a local change of lattice-elastic constants $K_{n,m}$ in Eq. (4.2):

$$H_{int}^{(ph)} = \frac{1}{2} \sum_{n,m} \delta K_{n,m}(\omega) Q_n^\omega Q_m^\omega, \quad (4.5)$$

where $\delta K_{n,m}(\omega) = -\sum_j \lambda(\mathbf{r}_j - \mathbf{R}_n) \lambda(\mathbf{r}_j - \mathbf{R}_m) R(\omega)$, and Q_n^ω, Q_m^ω are the displacements associated to crystalline phonon modes of frequency ω . Because $\delta K_{n,m}(\omega)$ is frequency-dependent, this quantity cannot be treated as an ordinary change of the elastic forces between displacements of the lattice. The change of $K_{n,m}$ is caused by the presence of the dynamical defects, giving rise to an effective retarded harmonic interaction between crystalline phonons.

In terms of phonon creation/annihilation operators, the interaction-Hamiltonian in Eq. (4.5) writes:

$$H_{int}^{(ph)} = \frac{1}{2} \sum_{\mathbf{k}, \mathbf{k}'} R(\omega) \sum_{j,n,m} \lambda(\mathbf{r}_j - \mathbf{R}_n) \lambda(\mathbf{r}_j - \mathbf{R}_m) e^{i\mathbf{k}\mathbf{R}_m} e^{-i\mathbf{k}'\mathbf{R}_n} \cdot \sqrt{\frac{\hbar}{M\omega_{\mathbf{k}}}} \sqrt{\frac{\hbar}{M\omega_{-\mathbf{k}'}}} (a_{-\mathbf{k}} + a_{\mathbf{k}}^\dagger)(a_{\mathbf{k}'} + a_{-\mathbf{k}'}^\dagger). \quad (4.6)$$

This derivation of the effective interaction Hamiltonian for phonons provides the frame to estimate the scattering probability.

4.3.3 Phonon scattering on polaronic defects

Using Fermi's golden rule and the results of the previous section, the scattering probability per unit time from phonon-state \mathbf{k} to \mathbf{k}' is:

$$w_{\mathbf{k} \rightarrow \mathbf{k}'} = \frac{2\pi}{\hbar} |\langle \mathbf{k} | H_{int}^{(ph)} | \mathbf{k}' \rangle|^2 \delta(\hbar\omega_{\mathbf{k}} - \hbar\omega_{\mathbf{k}'}). \quad (4.7)$$

In the long-wavelength limit that is of particular interest for thermal transport, the phase $e^{i\mathbf{k}\mathbf{R}_m}$ in Eq. (4.6) changes slowly over the interaction length, so that $\lambda(\mathbf{r}_j - \mathbf{R}_m)e^{-i\mathbf{k}\mathbf{R}_m}$ tends to $\lambda(\mathbf{r}_j - \mathbf{R}_m)e^{-i\mathbf{k}\mathbf{r}_j}$. Consequently $H_{int}^{(ph)}$ can be approximated by $\sum_{\mathbf{q},j} \hat{H}_{\mathbf{q},j} e^{i\mathbf{q}\mathbf{r}_j}$, where \mathbf{r}_j is the defect position and $\mathbf{q} = \mathbf{k} - \mathbf{k}'$. Dominant contributions to the scattering probability are obtained by averaging over defect positions. Since the defects are randomly distributed over large distances, $H_{int}^{(ph)}$ involves a rapidly oscillating function:

$$\overline{|\langle \mathbf{k}' | H_{int}^{(ph)} | \mathbf{k} \rangle|^2} \approx \sum_{\mathbf{q}, \mathbf{q}'} \sum_{j, j'} \overline{e^{i(\mathbf{q}-\mathbf{q}')\mathbf{r}_j}} \delta_{j, j'} \langle \mathbf{k} | \hat{H}_{\mathbf{q},j} | \mathbf{k}' \rangle \langle \mathbf{k}' | \hat{H}_{\mathbf{q}',j'} | \mathbf{k} \rangle \approx N_d \sum_{\mathbf{q}} |\langle \mathbf{k} | \hat{H}_{\mathbf{q},j} | \mathbf{k}' \rangle|^2, \quad (4.8)$$

with N_d the concentration of defects. The total scattering probability is obtained by integrating over all final states:

$$\begin{aligned} w(\omega_{\mathbf{k}}) &= \sum_{\mathbf{k}'} w_{\mathbf{k} \rightarrow \mathbf{k}'} = \frac{2\pi}{\hbar} \int \frac{d\mathbf{k}'}{(2\pi)^3} \overline{|\langle \mathbf{k} | H_{int}^{(ph)} | \mathbf{k}' \rangle|^2} \delta(\hbar\omega_{\mathbf{k}} - \hbar\omega_{\mathbf{k}'})(1 - \cos(\angle(\mathbf{k}, \mathbf{k}')) \\ &= \frac{\pi}{2} N_d \frac{g(\omega_{\mathbf{k}})}{\omega_{\mathbf{k}}^2} \left| \sum_j \lambda(\mathbf{r}_j) \frac{1}{\sqrt{M}} \right|^4 \cdot [R(\omega_{\mathbf{k}})]^2, \end{aligned} \quad (4.9)$$

where $g(\omega)$ denotes the phonon density of states. In this final form, $w(\omega) = 1/\tau_p(\omega)$, is one of the contributions to the total scattering time that appears in the phonon Boltzmann's equation for heat transport.

The phonon-scattering problem regarding two-level impurities has been analysed previously, applying Green's function formalism.[177,178] If the internal degree of freedom of a defect corresponds to a harmonic motion of frequency ω_p , the response function yields $R^{-1}(\omega) = m_p \cdot (\omega_p^2 - \omega^2)$. For a three dimensional acoustic phonon subsystem ($g(\omega) \sim \omega^2$) in Eq. (4.9), the scattering rate exhibits a resonant form:

$$\tau_p^{-1}(\omega) = N_d \sum_i b_{p,i} \frac{\omega_{p,i}^4}{(\omega_{p,i}^2 - \omega^2)^2}, \quad (4.10)$$

where $b_{p,i}$ are frequency-independent constants, and $\omega_{p,i}$ are the frequencies of internal excitations. Equation (4.10) has been generalised to more than one internal frequency.

A resonant structure of the scattering rate [31,46] has been considered on phenomenological grounds, mainly in the context of localised-phonon modes. Two-phonon excitations of localised oscillators as a mechanism for phonon-scattering has been investigated in Ref. 179. On the other hand, in our approach the starting points are polaronic defects, coupled to crystalline phonons by *electron-phonon interaction*. The low-energy excitations of polaronic defects, involving strong-charge-lattice correlations near a vacancy, define the resonance frequencies in Eq. (4.9).

4.3.4 Dynamical phonon scattering in anatase titanium dioxide

Implementing the Callaway formula with τ_p^{-1} included,¹ one does not only obtain a qualitative agreement with experimental data but also a remarkable quantitative agreement across the whole temperature range in Figure 4.4a (also in Fig. 4.5, for comparison). Striving to retain a minimal number of parameters, τ_p^{-1} relies on two resonant frequencies only in Equation (4.10), yielding $\omega_{p,1} = 16.4$ meV and $\omega_{p,2} = 7.8$ meV. These frequencies characterise internal excitations of polaronic defects and their values are much lower than E_b , in accordance with our prediction. Simultaneously, the values of the parameters related to the Casimir-, Rayleigh- and Umklapp- scattering are kept identical for the three kinds of SCs (transparent, brown and black) to highlight the role of polaronic effects. The parameter proportional to the concentration of defects N_d is the only one altered, allowing three distinct fitting curves to fairly align with experimental data of the three SCs in Figure 4.4a. From these fits, N_d in the conducting SC (black) is found to be about one order of magnitude higher than in the insulating SC (brown) (Table 4.1), and this term even vanishes in transparent anatase. Therefore, we infer that N_d is closely related to the amount of oxygen vacancies in our specimens.[140]

To our knowledge, the dynamical phonon-scattering as described in Eq. (4.10) and in the SI was derived for the first time, successfully explaining the reduction of κ in anatase TiO₂ by oxygen vacancies. This mechanism should act in the doped-rutile phase of TiO₂ as well, which has shown a strong dependence on the oxygen stoichiometry.[143] It could even be more general in other materials with defects or vacancies, where the stoichiometry could change considerably.[180]

4.4 Chemical doping with fluorine

To complete our understanding of the influence of defects on κ in anatase, we analyse transport properties of anatase in the presence of another type of defects. Crystals of anatase doped with fluorine (F-anatase) were prepared by adding high-purity ammonium fluoride (NH₄F) in the quartz tube, as a source of fluorine. The crystals have a dark blue/black color. The resistivity of F-anatase was measurable and displays a semiconducting behaviour, with $\rho = 32.6$ mΩ cm at room temperature. ρ is mildly increasing when the temperature decreases down to ~ 120 K, where it starts rising more rapidly to become very high at low temperatures. Between 80 and 30 K, $\rho(T)$ displays an activated behaviour (Figure 4.6b), with an activation energy of 13 meV.

The thermal conductivity of F-anatase has a similar temperature dependence and magnitude as anatase, with $\kappa(300\text{ K}) = 4$ W/Km, slightly lower than κ of black anatase. The maximum, however, is shifted towards lower temperatures (~ 110 K). Both curves are compared on Fig-

¹The resonant term τ_p^{-1} enters in the Callaway formula as follow:

$$\tau_p^{-1}(x, T) = a_p \left[\frac{(\gamma\omega_1)^4}{((\gamma\omega_1)^2 - x^2)^2} + \alpha \frac{(\gamma\omega_2)^4}{((\gamma\omega_2)^2 - x^2)^2} \right], \quad \gamma = \frac{\hbar}{k_B T}, \quad (4.11)$$

where α , $\omega_{1,2}$ and a_p are fitting parameters.

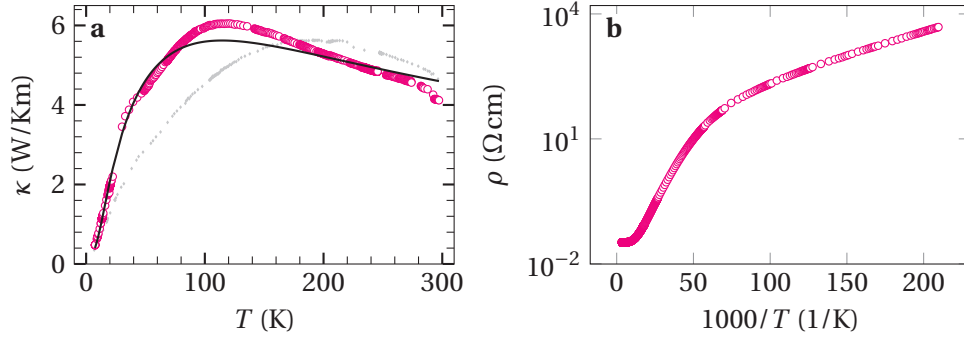


Figure 4.6 – **a** Thermal conductivity of F-doped anatase TiO_2 single-crystals. The data in grey correspond to the conducting, undoped (black) anatase, for comparison. The solid line is the fit obtained using the resonant polaronic scattering (Table 4.1). **b** Electrical conductivity plotted in the invert temperature scale.

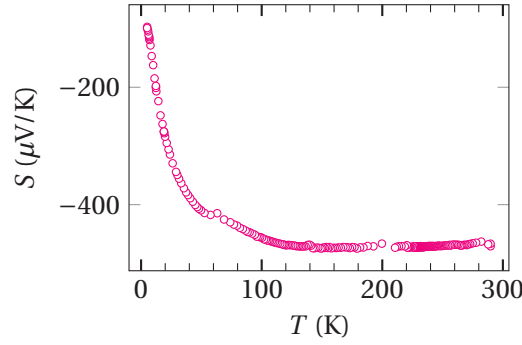


Figure 4.7 – Thermoelectric power of fluorine-doped anatase TiO_2 .

ure 4.6a. The incorporation of fluorine in anatase is known to create Ti^{3+} centers. Like oxygen vacancies, they entail localised charges, with energies well below the conduction band.[181–183] Therefore, the same fitting procedure as for reduced anatase was performed, with a resonant-polaronic scattering added to the other standard scattering mechanisms of the Callaway formula. The resulting fitting line (Fig. 4.6a) gives a good agreement with experimental data, and the fitting parameters further support resonant-polaronic scattering (Table 4.1). The Debye temperature, Casimir- and Umklapp- scattering rates were kept the same as for the other anatase crystals in Figure 4.4, and only the parameters related to impurity scattering were adjusted to fit experimental data. Compared to black anatase, Rayleigh scattering on static impurities has an enhanced contribution, whereas the parameter related to the intensity of the resonant-polaronic mechanism is two orders of magnitude lower than for black anatase. Remarkably, only one resonant frequency ($\omega_1 = 3.5$ meV) was necessary to obtain the fit in Fig. 4.6a.

Figure 4.7 shows the thermoelectric power of F-anatase. The negative sign of S over the whole temperature range indicate that electrons are the dominant charge carriers. At low temperature, the absolute value of S ($|S|$) increases with temperature; From 130 K to room temperature, S shows weak temperature dependence, with a nearly constant value of $470 \mu\text{V/K}$.

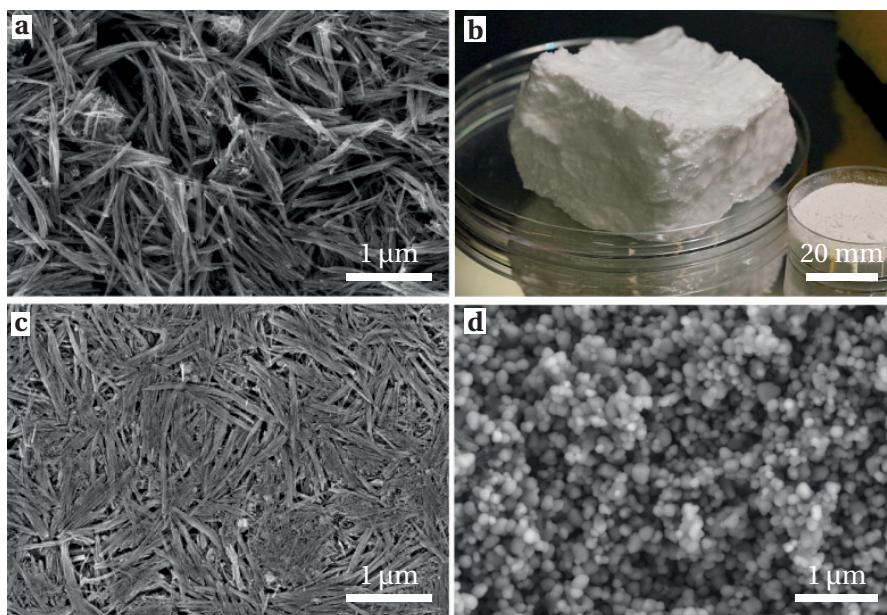


Figure 4.8 – Anatase foams and nanoparticles. **b** Photography of the as-grown TiO_2 foam; the jar (bottom right) contains the TiO_2 powder employed for the synthesis of nanowires and nanoparticles. **a**, **c**, **d** SEM micrographs of uncompressed foam, foam compressed (100 MPa) and TiO_2 nanoparticles, respectively. The scale bars correspond, 20 mm in **b** and 1 μm in **a**, **c** and **d**.

This unconventional temperature dependence has been attributed to polaronic effects in anatase SCs.[184]. The high S , combined with low κ is promising for energy conversion. The thermoelectric figure of merit of F-doped anatase monotonically increases with temperature up to 0.05 ± 0.01 at 300 K. Even though this value is below unity, it presents an enhancement compared to undoped anatase. To further augment ZT, the electrical resistivity should be lowered. One route to achieve this goal would be to increase the doping level to provide more charge carriers, but maintain the beneficial polaronic effects at the origin of high S and low κ . It is still a challenge to precisely control the doping of anatase, especially to incorporate more dopants in this material. Nevertheless, technical improvements in crystal growth, like the use of three-zone instead of two-zones furnaces could lead to a better control of the vapour transport.

4.5 Anatase foams and nanoparticles

A further reduction of κ in anatase was thought to be achievable by texturing the material at micro- and nano-scales. This is precisely the course of action taken here and presented next for anatase nanowires organized into foams and nanoparticles presented in Figure 4.8. On Fig. 4.8b, the egg-white-like, airy sample (we call it foam) was prepared from the quantity of TiO_2 powder exposed in the right Petri-dish, by first transforming it into nanowires. The breakthrough in its preparation is the scaling-up of the growth of nanowires from milligrams (hydrothermal synthesis) to kilograms by a different synthesis route.[135] Figure 4.8a displays

a zoom on the foam by scanning electron microscopy (SEM), showing the architecture of the nanowires, and after its compression applying 100 MPa of uniaxial pressure (Fig. 4.8c). The density and the inter-wire connections are clearly increased. For the sake of completeness, an assembly of anatase nanoparticles (mean diameter 50 nm), already used in many applications, was also prepared and measured (Fig. 4.8d).

Preparation of the foams The preparation of TiO₂ fibrous network (foam) is reported elsewhere.[135] Some of the foam was compressed under a uniaxial pressure of 100 MPa. Pellets were then shaped into parallelepipeds suitable for measurements of κ . Anatase TiO₂ nanoparticles were bought from Sigma-Aldrich Inc. (powder, ~ 325 mesh, > 99% purity) and mixed with polyvinil alcohol (PVA) and poly ethylene glycol (PEG). Secondly the mixture was compressed (380 MPa) to form pellets. In order to completely remove the organic molecules (PVA and PEG), 10 hours sintering at 600°C was performed. As for the foams, evenly shaped samples were obtained by dicing the pellets.

4.5.1 Thermal conductivity of anatase foams and nanoparticles

The thermal conductivities of the anatase foams and nanoparticles are shown in Figures 4.9a and b, mirrored in Figure 4.9c,d and e by sketches of the sample's textures. Compared to the most thermally insulating anatase single-crystal, κ of the as-grown foam at room-temperature is reduced by a factor of 600, attaining the ultra-low value of $\kappa = 0.014$ W/Km. This number competes with that of organic and silica aerogels at room-temperature and makes anatase foam a (thermal) superinsulator.[185] Yet, structural inhomogeneities and the high porosity of this foam alone ($\phi = 95\%$) cannot account for such a strong reduction of κ . Indeed, an estimation of the thermal conductivity of the foam κ_f as a sole consequence of the porosity can be obtained from percolation theory $\kappa_f = (1 - \phi)^{1.5} \cdot \kappa_b$, [94,95] where κ_b is the thermal conductivity of the pristine anatase SC. This estimation gives $\kappa_f = 0.1$ W/Km at room temperature, an order of magnitude above the experimental value. Hence, reasons for the particularly low value of κ_f and its temperature dependence have to be sought in the peculiar morphology of the foam at nanoscale: properties of individual nanowires composing the foam and the number of contacts between them drastically affect the thermal transport.

On average, anatase nanowires can be approximated as crystalline rods of ≈ 200 nm length and 10 nm diameter.[186] As for the contacts between nanowires, transmission-electron microscopy verifies their crystalline nature and their small cross-section (approx. 10 nm).[135] Further analysis of the scanning electron microscopy (SEM) images of the as-grown foam (Figures 4.8a and 4.9c) indicate that each nanowire connects to only few (~ 3 on average) neighbouring wires, whereas upon compression this number rises to ~ 25 (Figures 4.8c and 4.9d). Considering one nanowire, only phonons with momenta aligned along its axis contribute to the heat transport, for two reasons. First, Casimir scattering at the rod's boundaries heavily damps phonons whose momentum is not aligned along the rod's axis. Second, the finite number of unit cells along the rod's diameter restricts the kind of phonons allowed at low

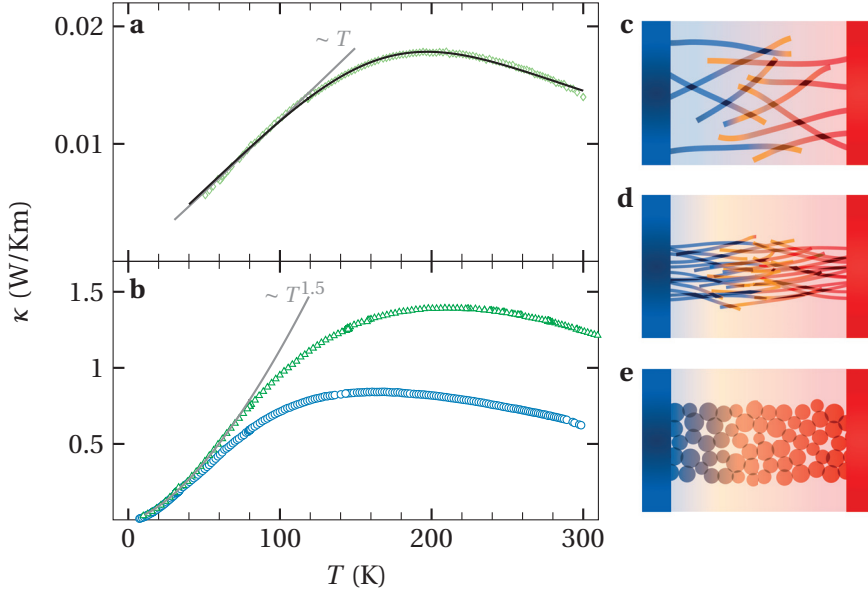


Figure 4.9 – **a** Temperature dependencies of the thermal conductivity of as-grown and **b** the compressed anatase TiO₂ foams (green triangles). The solid lines correspond to fitting curves. The blue circles represent the data for the assembly of nanoparticles. **c**, **d**, **e** Sketches of the three nanostructures based on the SEM images of Figures 4.8a, 4.8c and 4.8d.

temperature: only those characterised by zero-point motion in the direction perpendicular to the rod's axis can propagate heat. These effects of reduced dimensionality can be probed at low temperatures, where κ scales as T^β , and β is the effective-low-temperature dimension of the phonon subsystem (Eq. (1.35)). For the as-grown foam, according to a simple fit, $\beta = 1.0$ (Figure 4.9a), which permits the Callaway formula to be implemented with a single-dimensional density of state.[187] Compared to anatase SCs, the phonon system in anatase nanowires is less complex to describe owing to the scarce amount of defects (4 ppm)[130] Therefore, we deliberately omit the effects of polaronic and static defects. As a result the fit of the whole temperature dependence of κ in Fig. 4.9a can hardly be distinguished from the experimental data. At low-temperatures, the mean free path l_{ph} , comparable to the average length of nanowires, points towards a partially-ballistic, quasi-one-dimensional transport between contact areas. However, temperatures higher than $\theta_D/5$ prompt Umklapp scattering, hence significantly reducing l_{ph} .

We benefit from compaction as a simple and powerful way to continuously tune thermal (and mechanical) properties of the foam. As the porosity drops by about 70%, κ of the compressed foam increases by two orders of magnitude. Here, the contribution of the porosity is enhanced by the elevation in the number of inter-wire contacts, as the low-temperature exponent $\beta = 1.5$ (Figure 4.9b) supports the drastic change in the nanowires-connectivity scheme after compression. Interestingly, the assembly of TiO₂ nanoparticles exhibit analogous thermal transport properties as the compressed foam (blue dots in Figure 4.9b), especially at low temperatures. This suggests that both nanostructured materials are characterized by a

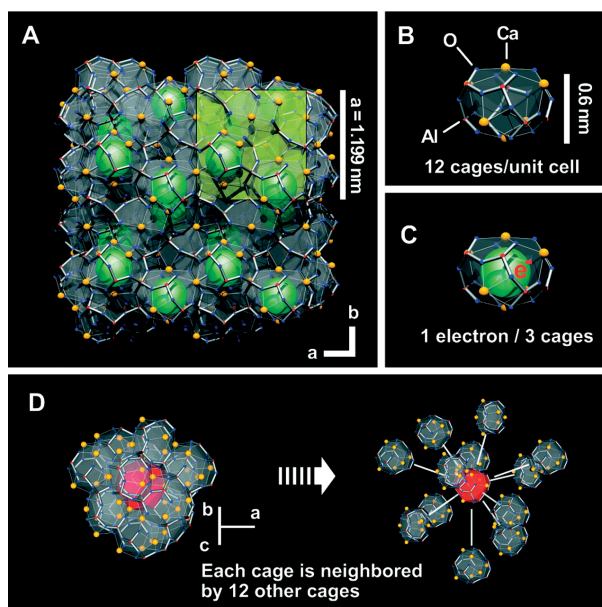


Figure 4.10 – Crystal structure of mayenite. Reprinted from Ref. 188.

similar connectivity scheme in the three-dimensional volume, with a small active portion of nanoparticles surface actually contributing to heat transport (as for nanowires).

4.6 Mayenite

Another functional material that, like anatase, could display polaronic effects in its transport properties is mayenite, a nanoporous oxide. Mayenite has a simple composition, $12\text{CaO} \cdot 7\text{Al}_2\text{O}_3$ (C12A7), associated with a more complex structure. A unit cell (cubic) of this light oxide in its pristine state is composed of a charged framework $[\text{Ca}_{24}\text{Al}_{28}\text{O}_{64}]^{4+}$ containing two “free” oxygen anions (2O^{2-}). In fact, 12 cages form the framework (Fig. 4.10A), and the oxygen anions are randomly distributed in the cages (Fig. 4.10B), with a total of one oxygen for six cages.[188] A cage has an outer(inner) diameter of $\sim 0.7(\sim 0.4) \text{ nm}$, and is neighbored by 12 cages (Fig. 4.10D). Cages “communicate” via openings of $\sim 0.3 \text{ nm}$, so that there can be ionic transport.[189,190]

This material, first used in cements, has recently attracted attention for its unusual structure and electronic properties.[191] The possibility to tune its electrical conductivity upon hydrogen reduction and UV-irradiation makes it a promising functional material for applications like electron emitter,[192] catalyst,[193] or THz-wave detector.[194]

4.6.1 Electronic properties

Upon hydrogen reduction of C12A7, localised electrons start to replace the oxygen anions, creating F^+ -centers localised in cages. Eventually, all the free oxygen anions are substituted by

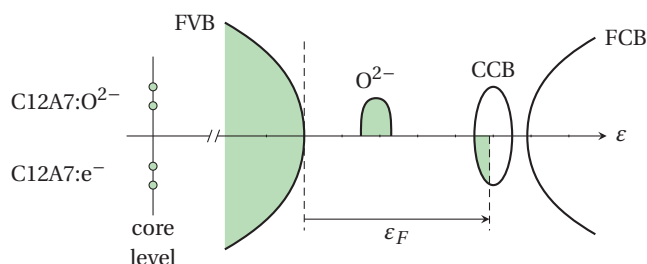


Figure 4.11 – A stylised schematic of the C12A7 electronic structure. Each tick mark represents about 1 eV. The shaded regions mark occupied states. FCB: framework conduction band, CCB: cage conduction band, FVB: framework valence band. Inspired from Ref. 191.

electrons (C12A7:e^-), and the mayenite becomes an electride. Electrides are materials usually unstable in normal-atmospheric conditions, with the peculiarity to have the smallest anions, electrons. Even though not every cage is occupied by one electron (only 1/3 of the cages contain electrons), mayenite is considered the first “stable” electride. When the amount of F^{+} -centers increases, states in a cage-conduction band (CCB) are populated, as it is represented in Figure 4.11, where simplified electronic densities of states for pristine and reduced C12A7:e^- are compared.

There have been report of a metal to insulator (MI) transition in the electrical resistivity of mayenite.[188,195,196] Pristine C12A7 is extremely insulating, beyond the measurement limits of conventional systems. Following hydrogenation and reduction of the free oxygen anions, the crystals change colors, from transparent to yellowish to black.[197] Along with the change in colour, the resistivity of the crystals decreases. First, in the lowest conductive samples, ρ reflects an activated behaviour, where electron-hopping is assisted by polarons. Following an increase of the amount of intra-cage electrons, $\rho(T)$ displays a variable-range-hopping-like (VRH) conduction mechanism ($\ln(\rho) \propto T^{-1/4}$). [188] When concentration of the host electrons becomes larger than 10^{21} cm^{-3} (maximal density $2.3 \cdot 10^{21} \text{ cm}^{-3}$), C12A7: e^- undergo a MI transition[196]. In metallic C12A7: e^- , intra-cage electrons are no more localised and participate to a cage conduction band with a large dispersion ($\sim 2 \text{ eV}$). Furthermore, superconductivity has been observed, with a critical temperature of $0.14 - 0.4 \text{ K}$, depending on the concentration of anionic electrons.[198] The tunability of mayenite systems regarding the wide range spanned by electrical resistivity offers a playground for future applications. It is especially true because the anionic electrons could also be replaced by different species like F^- or OH^- or larger molecules.

4.6.2 Electrical resistivity

We obtained mayenite specimens grown by the travelling molten zone method.² The yellowish, transparent crystals were cut in bars (approx. $5 \times 5 \times 0.5 \text{ mm}$) and prepared with Pt electrodes

²The mayenite crystals were provided courtesy of Dr. Branko Matović, Vinča Institute of Nuclear Science, Belgrade, Serbia.

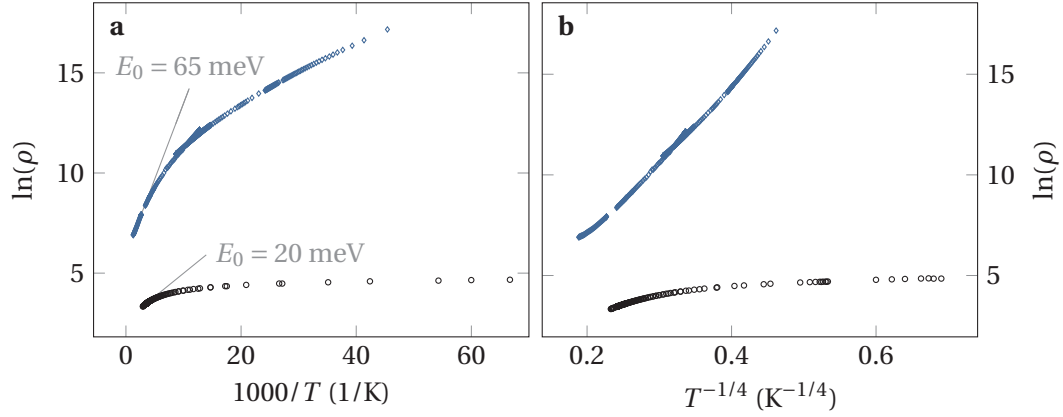


Figure 4.12 – Resistivity of H-reduced mayenite single-crystals. One specimen was reduced for 1 hour in a mixture of $N_2:H_2$ in a ratio 9 : 1 at 800°C (dark blue open circles). The other one was reduced in pure H_2 for 5 hours at 1050°C (black diamonds). **a** Arrhenius plot and **b** $\ln(\rho)$ versus reduced temperature $T^{-1/4}$, supporting variable-range hopping.

for 4-points resistivity measurements. For the low-temperature range of the most insulating samples, 2-points measurements were acquired with an electrometer. Additionally, some samples were cured in a reducing atmosphere: 1 hour in a mixture of $N_2:H_2$ (9 : 1) at 800°C and 5 hours in pure H_2 at 1050°C. After both of these treatments, the crystals were polished and showed a uniform black color throughout their sections. The latter treated sample and a pristine one were prepared for thermal conductivity, as described in Appendix A.2.

The resistance of pristine crystals was beyond the sensitivity of the electrometer ($1 > P\Omega$). The resistivity of the two hydrogen-reduced samples, shown on Figure 4.12, fairly agree with the picture described in the last section.[188] The most resistive samples (blue) follows $\rho = A \exp(BT^{-1/4})$ over three orders of magnitude, with A and B some constants, so that it corresponds to a variable-range-hopping-model mechanism (Fig. 4.12b). The other crystal, as a consequence of longer and hotter hydrogen treatment, has lower resistivity, showing a weaker dependence on temperature. For both specimen, activation energies can be extracted from the Arrhenius plot (Fig. 4.12a), of 65 and 20 meV respectively, two values sensibly lower than that given in Ref. 188.

4.6.3 Thermal conductivity

Whereas electronic properties of C12A7 have been largely explored, thermal properties of have been assessed in only a few reports. Huang *et al.* calculated the phonon dispersion and successfully compared the resulting heat capacity with experimental data.[199,200] We measured the thermal conductivity of mayenite crystals in a pristine state and after hydrogen reduction, showed in Figure 4.13. At room temperature, $\kappa = 2$ W/Km for the pristine sample, slowly rises to a maximum value of 4.3 W/Km as the temperature decreases to 30 K, before it finally decreases towards zero. In the higher temperature range, κ scales as $1/T$, as three-

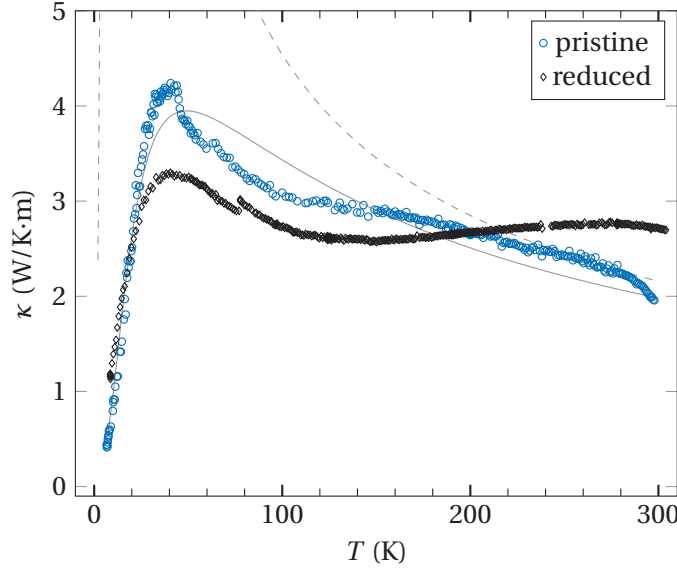


Figure 4.13 – Temperature-dependent thermal conductivity of pristine (blue circles) and H-reduced (black diamond) mayenite single-crystals. The solid line is a fit obtained with the parameters in Table 4.2, whereas the dashed line is the same fit without resonant scattering ($a_r = 0$), which reaches the maximal value of $\kappa = 19.2$ W/Km at 15 K.

	a_C/A	a_R/A	a_U/A	θ_D (K)	T_U (K)	a_r/A	ω_0 (K)
mayenite	60	$29 \cdot 10^{-4}$	0.38	450	50	$1.5 \cdot 10^4$	25

Table 4.2 – Model parameters in Eq. (1.36) for mayenite.

phonon processes dominate the thermal conduction. In the lower temperature range, κ does not increase as much as in the case for crystalline materials.

The peculiar structure of C12A7 is that of a clathrate, with cages hosting oxygen ions. In this context, this would not be a surprise to observe a coupling between vibrational modes of the free oxygen and the acoustic modes of the framework. As a consequence of this scattering, the phonon-mean-free path would be shortened. This hypothesis is probed by adding a resonant term as described in Equation (1.37) to the total scattering time in the Callaway formula (Eq. (1.36)). A fitting line is obtained in good agreement with the experimental data (Fig. 4.13). The fitting parameters obtained are reported in Table 4.2. For this fitting procedure, the Debye temperature provided by a study on C12A7 thin films ($\theta_D = 450$ K) was used.[201] The rattling motion of the free oxygen in the cage was associated to an absorption band at ~ 1.3 THz.[194,202] This frequency corresponds well to the single resonant frequency emerging from the fit, $\omega_0 = 25$ K, therefore supporting strong phonon scattering by the free O^{2-} . The dashed line on Fig. 4.13 shows the thermal conductivity extrapolated in absence of resonant scattering. This permits us to grasp the pronounced effect of resonant coupling on κ .

The thermal conductivity of the reduced (at 1050°C) sample does not differ much from

that of the pristine sample, in value. Nevertheless, the temperature dependence is different, and non-trivial, with a maximum at ~ 30 K followed by a dip at ~ 120 K. At room temperature, $\kappa = 2.8$ W/Km even surpasses the value of the pristine specimen. Above 200 K, unlike for the pristine mayenite, $\kappa(T)$ does not follow a $1/T$ dependence. One has to recall that, in the reduced specimen, some cages are filled with oxygen anions, and some with electrons. As a consequence, there could be a supplementary contribution to phonon scattering from modes related to anionic electrons, in addition to the interference of the O^- anions. This contribution might stem from the large deformation of cages (polarons) filled with oxygen compared to cages filled with an electron.[196] In this case, the situation could have similarities with oxygen vacancies in anatase TiO_2 in terms of localised charges polarising the lattice, with states deep in the gap (~ 2.6 eV below the framework conduction band.[203]). However, unlike oxygen vacancies in anatase, the strength of the interaction is probably weak, compensated by the large amount of anionic electrons (~ 2 orders of magnitude more than oxygen vacancies in anatase).

4.7 Conclusions

The thermal conductivity of $Ca_{12}Al_{14}O_{33}$ is reported for the first time. This system shows polaronic features, and the low value of κ in the pristine crystals arise from its peculiar-clathrated structure. In view of these measurements, the mayenite electride appears to be a phonon-glass/electronic-crystal system. This family of compounds is foreseen for its enhanced thermoelectric properties. Indeed, the fact that no significant change in κ occurs upon hydrogen-reduction, simultaneously with an increase in the electrical conductivity is very promising for thermoelectric applications because of the net benefit in $ZT(\propto \kappa^{-1}\rho^{-1})$. In the present situation, we can estimate, taking the value of $\rho(300\text{ K}) = 2\text{ m}\Omega\text{cm}$ [196] and assuming $\kappa(300\text{ K}) = 5\text{ W/Km}$, that the required thermopower to obtain $ZT \simeq 1$ at 300 K is $S \simeq 600\text{ }\mu\text{V/K}$. As the value of S appears to be proportional to $-\ln(\rho)$, [188] further efforts in doping would be necessary to increase the electronic entropy. If one could fill more cages with a proper dopant, κ could be further damped and S enhanced, provided that these dopants enable a cage conduction band with delocalized charge carriers. As the cages are voluminous, they could host molecules with large masses (larger than oxygen) and with an ideal average charge of $-1/6e^-$.

A summary of our measurements on Figure 4.14 shows the outstanding flexibility of anatase TiO_2 -based systems in tuning the thermal conductivity over three orders of magnitudes at 300 K by polaronic and nano-structuring effects. The dynamic-polaronic-scattering mechanism, prompted by charged-oxygen vacancies, had not been observed before. It has been uncovered by theoretical modelling and found to dominantly account for the reduction of κ in bulk anatase. Yet, beyond oxygen vacancies in anatase, this model encompasses wider classes of defects and impurities, opening the door to a more accurate understanding of polaronic effects on phonon thermal transport. This also brings attention to the multiple consequences of doping efforts in anatase, many of which aspire to reducing the energy gap

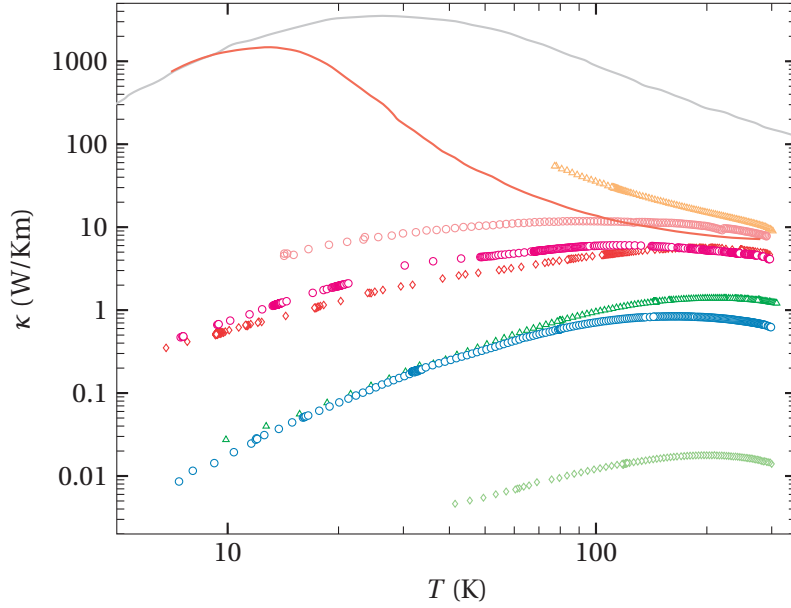


Figure 4.14 – Overview of the thermal conductivity of single-crystals and textured anatase polymorph of TiO_2 . The thermal conductivity of the transparent (orange triangles), semi-conducting-brown (pink circles) and conducting-black (red diamonds) single-crystals, compressed (dark green triangles) and as-grown (light-green diamonds) foams made of nanowires and of nanoparticles (blue circles), span four orders of magnitude. For comparison, the solid line shows the thermal conductivity of rutile TiO_2 single-crystal, reproduced from Reference 29.

and to collect a broader spectral range in photovoltaics. Our study shows that one does not only change the electronic, but substantially the thermal properties as well, through the resonant scattering of phonons on polaronic defects. We explored the case of fluorine-doped anatase, where we also observed polaronic effects on κ . This fundamentally-new finding gains importance because polarons are present in many other functional oxides like SrTiO_3 , ZnO , CaMnO_3 .

Next to that, it is an extremely useful result that in a macroscopic assembly of nanowires, and not only in lithographically fabricated micron-square surfaces, one can engineer structures with ultra-low thermal conductivity. The value of 0.014 W/Km is important and beneficial by itself, because it calls for an excellent thermal insulator, but especially also by the way it was reached: by the discreet-phonon dispersion due to the one-dimensionality of the nanowires. Since the same mechanism does not limit the electrical conductivity, this foam would be an excellent material for thermoelectric applications if one doped them to metallicity.[141] Recalling that in anatase thin films doped with 6% of Nb, the high power factor ($S^2\sigma$), where S is the Seebeck coefficient and σ the electrical conductivity) of $14 \mu\text{W}/\text{K}^2\text{cm}$ gave only a figure of merit (ZT) of 0.1 because of the high thermal conductivity (8.5 W/Km) of the thin film, but not attractive enough for practical purposes. If one could achieve a high σ by doping the nanowires, the foam could deliver a high ZT, and, together with its chemical and high temperatures stability, would be suitable for scalable applications.

5 Thermoelectricity in hybrid-halide perovskites

5.1 Organic-inorganic metallic perovskites

The emerging solar-cell community has been shaken up in 2010 by the advent of a newly rediscovered class of materials with outstanding properties. In only five years, hybrid-halide-perovskites-based solar cells have increased their efficiencies by close to 70%, a record rate in developing solar technologies.[204] Today, the best modules (23.3%) compete with crystalline-silicon technologies and perovskite-solar cells are foreseen to invade the market swiftly.[205] The reasons for such a momentum in the field are mainly the ease with which perovskites can be synthesised and the simple architecture of the modules. At the origin of the keen interest for hybrid-halide-perovskites, methylammonium lead iodide (MAPbI_3) was the first (historical[206]) material recognised for its photo-active behaviour.¹ This material crystallises in the a perovskite structure (hence its name), with corner-sharing octahedra formed by iodine atoms. At the centre of these octahedra lies a lead atom (B-site cation), and between them an organic molecule (MA, A-site cation). The structure is depicted in Figure 5.1a, next to the sketch of a typical-device architecture. MAPbI_3 can be grown by different methods. Apart from thermal evaporation,² the other routes use crystallisation from solutions.[209,210] These latter synthesis methods foster a very rapid development of new, more efficient and sustainable-perovskite materials, mainly because of the cheap and simple wet-chemical preparation method: they can be done close to ambient temperatures, processing times are short, chemicals involved are compliant to most facilities and only mildly toxic, at worse. Moreover, the synthesis from solutions offers flexibility in the fabrication of functional devices and opens new doors for technological applications. In some cases, a precursor solution can be spin-coated onto a substrate, leaving the desired thickness of perovskite material after evaporation of the solvent. Perovskites can also be printed,[211] or tailored to the desired shape thanks to nanofluidic channels.[212]

¹Although related materials were discovered earlier in the end of the 19th century.[207]

²Thermal evaporation for these materials is challenging due to the low-evaporation temperature of the materials considered. The growth of large-epitaxial-perovskite-thin films has not yet been demonstrated.

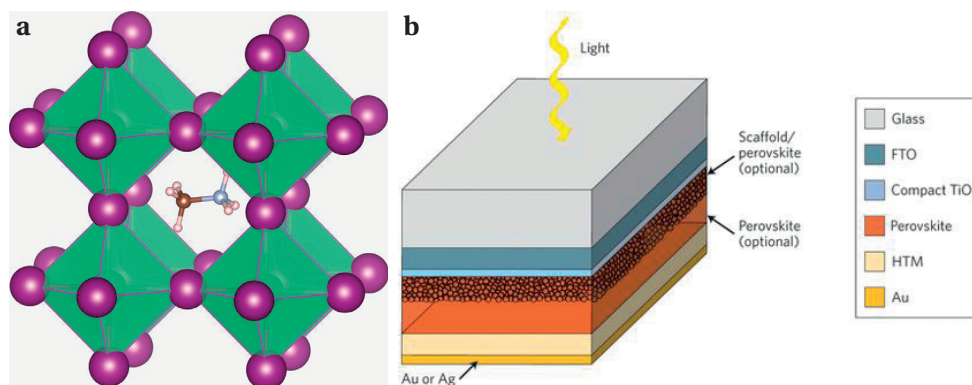


Figure 5.1 – **a** Crystalline structure of methylammonium lead iodide. Iodine atoms define octahedra whose centre is occupied by the lead atoms. The methylammonium cation is in the interstitial space surrounded by four octahedra. Reproduced from Ref. 208. **b** Model-architecture of a layered perovskite solar cell. This kind of cell can be made by depositing only a few successive layers: two electrodes (FTO and Au), the active layer (perovskite) and a hole-collecting layer (compact TiO_2). Reproduced from Ref. 12.

5.1.1 Highly tunable structures

Beyond device engineering, a virtue of hybrid perovskites is their chemical versatility. On the one hand, the perovskite structure (ABX_3) allows for manifold combinations of elements A, B or/and X. Here the cation A-site can host organic molecules like methylamine, formamidine (to name only a few), but also inorganic elements like caesium. The B-site is a post-transition metal like lead, tin or even bismuth and the X-site a halogen, e.g. chlorine, bromine and iodine. A few examples of colourful crystal synthesised in our laboratories are shown in Figure 5.2. Furthermore, the structure can be chemically doped, which offers virtually unbounded tuning of the physical properties of the resulting materials.[213] On the other hand, the size and crystal polymorphism can be varied within the same family of compounds. Large (millimetres) single crystals can be grown, whereas spin-coated or printed materials tend to be granular (grains from tens of microns to tens of nanometres). It is also possible, for some compounds, to tailor their morphology to obtain quantum dots, nano-platelets or nanowires.[134,214] Finally, a whole field of study is devoted to perovskites confined in two dimensions (2D). 2D-perovskites have a structure of the form $\text{A}_{n-1}\text{B}_n\text{X}_{3n+1}$ where $n > 1$ is an integer. “Conducting” layers with this structure can be stacked by intercalation of a spacer cation to form complex arrays.

If, compared to Si-based technologies, perovskites possess undeniable advantages like easy, rapid synthesis from cheap elements and wide tunability, they also have their downsides. A first problem arises from their poor chemical stability in atmospheric conditions in the long run, which can pose serious issue for applications. Indeed, perovskites such as MAPbI_3 are soluble in water, and even absorb water.[215] These class of materials usually does not sustain temperatures higher than 500 K, and thermal cycling seems to have impact on the performance of devices, because of structural phase transitions close to room temperature.[216] However,

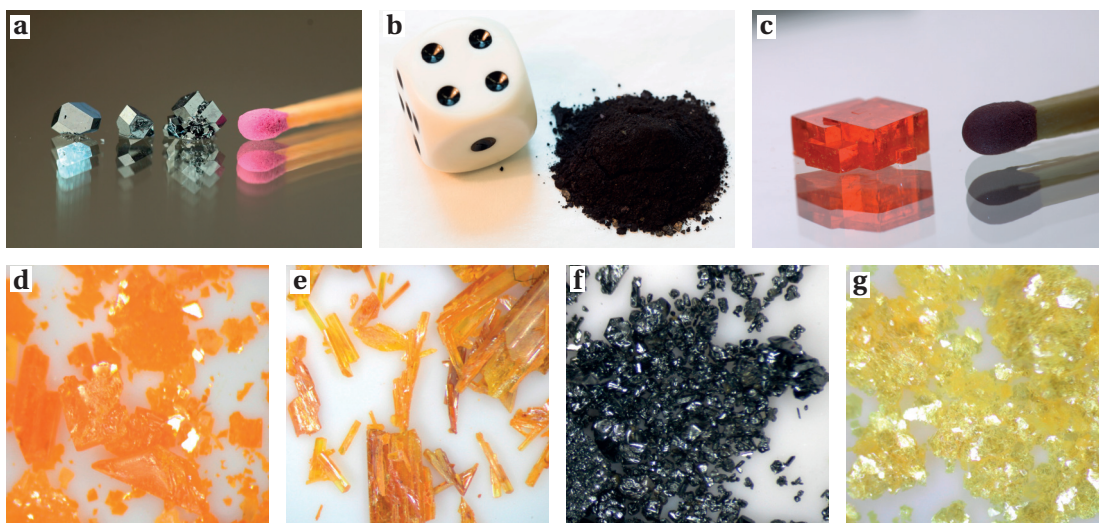


Figure 5.2 – Examples of organo-metallic perovskites. **a** Methylammonium lead iodide single crystals. **b** Methylammonium tin iodide powder. **c** Methylammonium lead bromide single crystal. **d** Butylammonium lead iodide single crystals. **e** Propylammonium lead iodide needle-like single crystals. **f** Formamidinium lead iodide single crystals. **g** Methylammonium bismuth bromide crystallites.

there is a tremendous effort to deal with undesirable effects and significant advances have been made to extend the duty life of perovskite materials. One route to enhance stability is chemical doping leading to more stable or non-soluble materials; another is decrease the dimensionality of the materials (2D-perovskites). At the level of devices, encapsulation has also been considered as viable for applications.[217] A second drawback of hybrid perovskites is the presence of toxic or not environmentally friendly elements (e.g. lead) in their composition.

5.1.2 Beyond photovoltaic technologies

It is clear that following the native impulse from the photovoltaic community, precise assessment of the physical properties of hybrid perovskite has been a necessity. Research in growing new compounds, characterising their structural, optical, electronic, thermal, magnetic and mechanical properties has lead to the discovery of very interesting phenomena. In fact, they have given a ground for development of various applications beyond photovoltaics.[218,219] It is not a surprise that hybrid perovskites are photosensitive and therefore they have been found to be performant for photodetection[209,220–223]. Due to the high mass of the B-site cation, they absorb higher energy light well and promising results have been obtain for gamma and x-ray detection[224,225] Conversely, light emission[203,226] and lasing[227,228] have been demonstrated. Next to their outstanding optoelectronic properties, hybrid-halide perovskites are sensitive to surrounding gases.[229] Finally, He and Galli have performed first-principle calculation and proposed that two materials, MAPbI_3 and MASnI_3 , could be used for thermoelectric applications.[13] Subsequently we have measured the thermoelectric properties

of these materials revealing excellent aptitudes of MASnI_3 for thermoelectricity.[230] These results will be discussed in the next section.³

5.2 Thermoelectric properties of MAPbI_3 , MAPbBr_3 and MASnI_3

For development of applications, it is of the utmost importance to properly characterise and understand electrical and thermal properties of the active material, to later be able to engineer these properties. For the most popular compounds in the family of hybrid-halide perovskites, we synthesised high-quality single-crystals or powder. Millimetre-sized single-crystal of MAPbI_3 and MAPbBr_3 are shown in Figure 5.2a and c, and powder of MASnI_3 in Figure 5.2b. The transport coefficients S , ρ and κ of these three compounds were measured according to method described in Appendix A, except for the thermoelectric power, measured by a lock-in technique, as described in Ref. 230. Synthesis of MAPbI_3 and MASnI_3 is described in the same article; for MAPbBr_3 , the synthesis method is the one described in Ref. 223. The following discussion has inspired reports in the literature: the resistivity and thermal conductivity of MAPbI_3 in dark have been discussed in Ref. 46 and 231. Moreover, the resistivity and thermoelectric power of MASnI_3 have already been explored.[232–234]

5.2.1 Electrical resistivity

The electrical resistivity of the three compounds is reported in Figure 5.3. In dark, ρ of MAPbI_3 and MAPbBr_3 is smoothly decreasing with increasing temperatures (insulating behaviour). Upon white-light illumination the resistivity globally decreases up to more than two orders of magnitude as an increasing number of photo-excited carriers become available for conduction. For MAPbI_3 , at $T < 150$ K, ρ of the illuminated sample decreases with lowering temperature in a metal-like behaviour. This crossover from non-metal- to metal- like resistivity reveals the coexistence of extended and shallow donor states 0.1 eV below the conduction band.[231] For MAPbBr_3 , there is no such crossover and ρ becomes metallic under low-intensity illumination already. By increasing the light intensity, $\rho(300\text{ K})$ is strongly diminished, as the slope ($d\rho/dT$) also decreases (Fig. 5.3d).

The temperature-dependent resistivity of MASnI_3 samples (Figure 5.3b) varies from a thermally activated behaviour (with activation energy E_a equal to 0.25 eV) to a metallic one for the different samples investigated. It has been previously reported that MASnI_3 is a doped semiconductor.[234] The presence of an unknown but significant amount of impurity levels within the MASnI_3 band gap is at the origin of this varying $\rho(T)$. The material has been intentionally doped by Takahashi et al.,[232] thus allowing to obtain a metallic behaviour. Two of their $\rho(T)$ curves are reprinted there (Figure 5.3b). The observed tunability of the electrical conductivity in MASnI_3 is therefore expected to be like in other extrinsic semiconductors.[235] Thus, by doping MASnI_3 , it is possible to obtain larger carrier densities and optimize the

³Many other possible applications have been omitted here, like perovskite-based batteries, water-splitting modules or field-effect transistors.[210]

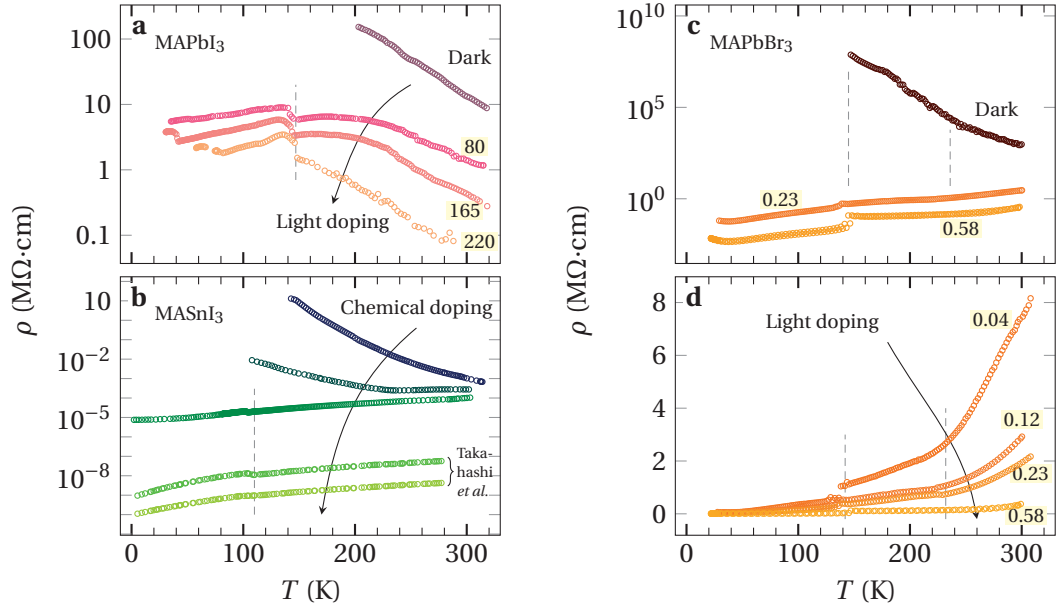


Figure 5.3 – Temperature-dependent electrical resistivity of **a** MAPbI₃, **b** MASnI₃ and **c,d** MAPbBr₃, under different illumination levels and chemical doping. The numbers labelling the curve correspond to the intensity of illumination, in mW/cm². Structural phase transitions can clearly be seen and are indicated by the dashed vertical segments. For MASnI₃, the downmost curves are reproduced from Ref. 232. The other data for MAPbI₃ and MASnI₃ is reproduced from Ref. 230.

thermoelectric properties. In contrary to MAPbI₃ and MAPbBr₃ no significant change under illumination could be observed for MASnI₃.

The various kinks (e.g. at 150 K for MAPbI₃) in ρ , S and κ account for the structural phase transition from a tetragonal to an orthorhombic symmetry of the lattice. The observed small shift in the temperature of this transition might be due to some heating effect of the lamp.

5.2.2 Seebeck coefficient

The temperature dependency of the Seebeck coefficient of MAPbI₃ follows a non-trivial behaviour with peaks appearing at $T \approx 270$, 215, and 190 K in the dark and at ≈ 280 and 210 K under white-light illumination. The absolute value of the thermoelectric power of MAPbI₃ was found to be slightly sample-dependent; however, the overall temperature behaviour is similar from one sample to another. The positive Seebeck coefficient argues for holes as the dominant type of charge carriers, but its non-monotonic temperature dependency indicates that electrons, whose temperature-dependent mobility differs from the one of holes, also participate in the charge transport. Independent variations of the contributions of holes (or electrons) weighted by their respective mobilities to the Seebeck coefficient could be the reason for some of the peaks. The decrease in S at room temperature (295 K) upon illumination, from $S_{\text{dark}} = 0.82$ mV/K to $S_{\text{light}} = 0.54$ mV/K, is consistent with the resistivity data because electrons are photo-induced in the conduction band, decreasing the absolute value of S .

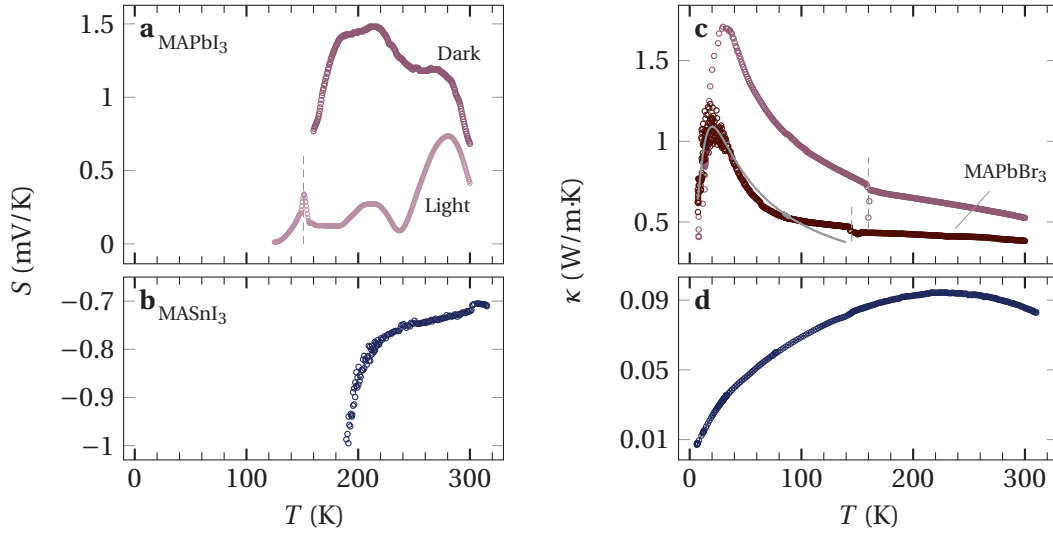


Figure 5.4 – Temperature dependent Seebeck coefficient and thermal conductivity of **a,c** MAPbI_3 and **b,d** MASnI_3 and thermal conductivity of **c** MAPbBr_3 . The thermal conductivity of MAPbI_3 was reproduced from Ref. 46. The grey solid line is a fit obtained from the Callaway formula.

The negative sign of S of MASnI_3 (Figure 5.4b) indicates that the majority carriers are electrons, in agreement with a previous study;[236] however, the negative sign is in contradiction with some previous results.[232] This discrepancy might be due to the different nature of the impurity levels present in the band gap. A predominant number of donor over acceptor impurity levels explains the negative sign observed in our sample. The absolute value of $S(295 \text{ K}) = -0.72 \text{ mV/K}$ is rather high, one order of magnitude larger than the value reported in Ref. 236, because the samples under consideration are semiconducting. Upon doping, S decreases (see next section), and for the metallic samples, it has a linear temperature dependency.[232] Its value stays in the $100 \mu\text{V/K}$ range at 295 K.

The thermoelectric power of MAPbBr_3 was found to be very difficult to quantify. An estimation from Staub *et al.*[237] in thin-films is 1 mV/K .

5.2.3 Thermal transport

The thermal conductivity of the three compounds is very low (Figure 5.4c and d), and not affected by illumination. First, from the Wiedemann-Franz law (WFL), heat transport via charge carriers can be excluded, so that κ is the thermal conductivity of the phonon system, except for the more conductive samples of Takahashi *et al.*,[232], where an additional contribution of the charge carriers to the thermal conductivity (κ_{el}) cannot be neglected and has to be taken into account. $\kappa(T)$ of MAPbI_3 and MAPbBr_3 are similar, with peaks at 40 and 30 K, respectively. Pisoni *et al.* gave clues that the very low κ in MAPbI_3 is caused by the rattling motion of the MA cations by modelling $\kappa(T)$ with the Callaway formula, improved with a resonant scattering term as described in Equation (1.37).[46] A similar fitting procedure

5.2. Thermoelectric properties

	a_C/A	a_R/A	a_U/A	θ_D (K)	T_U (K)	a_r/A	ω_0 (K)
MAPbI ₃ [46]	$2 \cdot 10^4$	$40 \cdot 10^{-4}$	0.87	120	7.5	$4.8 \cdot 10^5$	42
MAPbBr ₃	0	$9 \cdot 10^{-4}$	0.79	60	6	$1.2 \cdot 10^4$	30

Table 5.1 – Model parameters in Eq. (1.36) for MAPbI₃ and MAPbBr₃.

has been applied to MAPbBr₃, providing a curve (solid-grey) that reproduces well the main features of the experimental κ . The fitting parameter are reasonably close to that of MAPbI₃, and can be seen in Table 5.1. Above the structural phase transition from orthorhombic to tetragonal at 160 K, $\kappa(T)$ shows a very weak dependence on the temperature. This surprising behaviour should be investigated further.

In fact, subsequent studies shed more light on the mechanisms of thermal conduction in MAPbI₃. Two major contributions are believed to be responsible for the low value of κ . Simulations from many-body perturbation theory identified the low group velocity and anharmonic phonon-phonon interaction as one reason for the low κ of MAPbI₃. [238,239] However, the most important factor responsible to reduce κ is explained by the nature of the A-site organic cation. In case of MAPbI₃, the MA cation is not constrained to a preferential orientation. It therefore has rotational modes at the origin of dynamic disorder of this material. [238,240–244] The effect of the cation dynamics is experimentally highlighted by comparing κ of MAPbI₃, MAPbBr₃ and CsPbBr₃ nanowires. [244] There, for CsPbBr₃ the fully inorganic perovskite, κ is the highest. Moreover, Miyata *et al.* describe the formation of large polarons accounting for the low mobility and strong phonon-phonon scattering.⁴ Finally, equilibrium-molecular-dynamics simulations argue that there could be an anisotropy in κ , a concept that could more consequence-bearing for thin-film materials than for single crystals. [242] In the same study, Wang *et al.* claim that MAPbBr₃ should have a higher κ than MAPbI₃, a prediction contradicted by our experimental results (Figure 5.4c). There, the assumption that phonon lifetimes are the same for materials of the same class (e.g. MAPbI₃ and MAPbBr₃) might be incorrect. Our experimental results regarding MAPbBr₃ and MAPbI₃ single crystals do not match well the trend of κ of thin films at and close to room-temperature. [245] However, in the case of thin films, grain boundaries and the substrate can substantially impact κ , thus blurring different effects and rendering thin-films and SCs difficult to compare.

Regarding MASnI₃, $\kappa = 0.09 \pm 0.01$ W/Km is even lower than that observed in MAPbI₃ ($\kappa = 0.5 \pm 0.1$ W/Km, Figure 5.4d). This could be partially due to the polycrystalline nature of the MASnI₃ sample studied; however, the overall temperature dependency of κ in MASnI₃ is very different from the one in MAPbI₃. The broad maximum around 220 K suggests that there are some small structural motives that limit the phonon mean free path already at high temperature, in contrast with MAPbI₃ and MASnI₃ where it happens at 30 K. The overall temperature variation of κ in MASnI₃ seems to have a glassy behaviour, which might stem

⁴It is interesting to note that, in this study, they refer to the structure of MAPbI₃ and other similar perovskites as crystal-liquid dual. From this point of view, some of the properties of the material correspond to that of crystalline matter (charge transport), whereas other can be described well in terms of liquids (phonon glass, κ , etc.).

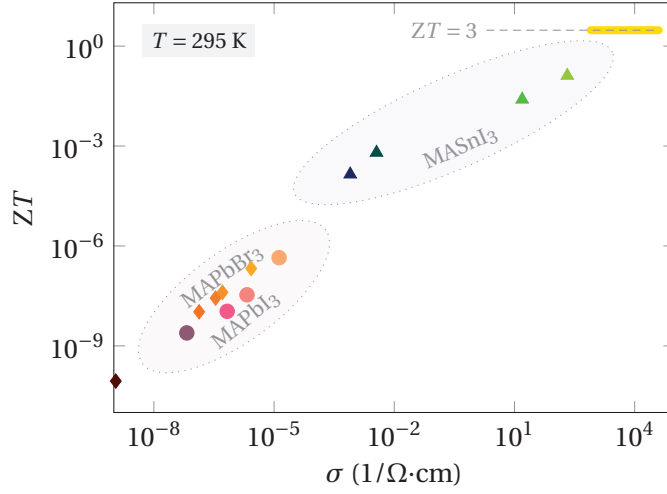


Figure 5.5 – Evolution of the figure of merit ZT as a function of the electrical conductivity, at room temperature. The dots, diamonds and triangles correspond to MAPbI_3 , MAPbBr_3 and MASnI_3 , respectively. ZT is enhanced upon illumination (MAPbI_3 and MAPbBr_3) and by impurity doping (MASnI_3). The zone shaded in yellow corresponds to the target-value $ZT = 3$, recommended for applications.

from an effective scattering source spread over a larger temperature range.

5.2.4 Thermoelectric figure of merit

The temperature dependency of ZT for MAPbI_3 , MAPbBr_3 and MASnI_3 , calculated from the transport coefficients increases globally with temperature.[230] We assume the same value of κ for our MASnI_3 samples with different doping levels because the contribution of charges to the thermal transport is negligible. For the measurements reported by Takahashi *et al.*, we used their values of ρ and S in combination with κ reported on Figure 5.4d, corrected with an additional contribution κ_{el} of the charges.

The evolution of ZT at room temperature is summarized in Figure 5.5 as a function of the electrical conductivity. ZT of MAPbI_3 (MAPbBr_3) in dark just below room temperature reaches a maximum value of 10^{-9} (10^{-8}) only. Photo-induced doping initiates an elevation of ZT because the electrical conductivity strongly increases, while S is maintained to a high value, yet ZT keeps very low, indicating that this form of doping is not sufficient for thermoelectric applications. Indeed, Hall-effect measurements for MAPbI_3 (MAPbBr_3) yield a carrier density $n \simeq 10^{14}$ (10^{12}) cm^{-3} and a carrier mobility $\mu \simeq 13$ (8) $\text{cm}^2 \text{V}^{-1}\text{s}^{-1}$ [246] for the strongest illumination condition, whereas theoretical calculations of different groups [13,247] predict that $n \simeq 10^{18}$ to 10^{19}cm^{-3} is required to bring ZT close to unity. In the case of MASnI_3 , the most resistive sample has the magnitude well above the one of MAPbI_3 . Intentional (as reported in Ref. 232) or unintentional (as in our case) doping gives much higher conductivities, so that ZT at room temperature reaches the value of 0.13. This tendency is very promising, and it should be explored systematically in the future.

Figure 5.5 emphasizes that σ is the quantity which tunes ZT independently if its increase is due to the enhancement of the carrier density or of the charge mobility. We suppose that carrier mobility does not change substantially with doping, so this plot gives a good approximation for the variation of ZT with n , as well. As it can be seen in Figure 5.5, σ plays a dominant role in the modulation of ZT. Indeed, the difference in resistivity, two orders of magnitude between the non-illuminated and the illuminated MASnI_3 sample, does not result in a dramatic decrease in the thermoelectric power under the same condition.

5.2.5 Improving the thermoelectric figure of merit

For an efficient thermoelectric conversion and to compete with the best available materials, $ZT = 3$ is required. Density functional calculations, compared MASnI_3 and $\text{NH}_2\text{CHNH}_2\text{SnI}_3$ with Bi_2Te_3 and concluded that such materials could compete with hold-doped Bi_2Te_3 . [248] Introducing polaronic effects [249] to increase S can be a rather complicated task, because S is already relatively high, and large polarons are already present in MAPbI_3 and MASnI_3 . [242]. Furthermore, κ is already very low and the possibilities to further decrease it are by structuring the material at the nanoscale. This has been achieved for MAPbI_3 [46] providing a moderate effect. Instead, doping MASnI_3 will be the route to further increase ZT. According to the trend shown in Figure 5.5, one can extrapolate the room temperature resistivity necessary to satisfy this request: $\rho = 1 \cdot 10^{-3}$ to $3 \cdot 10^{-5} \Omega \text{ cm}$. This value is not more than two orders of magnitude lower than that observed in intentionally doped MASnI_3 crystals by Takahashi *et al.* [232, 234] In their work, they studied the effect of the dopant uptake during the crystal growth, under equilibrium conditions, from Sn^{II} and Sn^{IV} precursors. To quantitatively evaluate the carrier concentrations, they performed Hall-effect measurements. They concluded that the dopant uptake was rather low; that is, the carrier concentration between the as-grown and the artificially doped MASnI_3 samples was increased by one order of magnitude only. However, this “ Sn^{II} and Sn^{IV} precursor”-doping can be instead regarded as self-doping. Hence this is not likely an effective way to shift the thermodynamic equilibrium between the Sn^{II} and Sn^{IV} ions in the resulted MASnI_3 crystal. Therefore, we suggest to shift and stabilize the Sn^{II} and Sn^{IV} redox equilibrium in the Sn-perovskite by doping with foreign cations having a stable oxidation state. For instance, the room-temperature conductivity of the single crystals of metallic slabs of the radical cation of ethylenedithio-1,2-diiodo-tetrathiafulvalene, EDT-TTF-I_2 , and polymeric lead iodide covalent anionic layers $(\beta - (\text{EDT-TTF-I}_2)_2^{\bullet+} [(\text{Pb}_{5/6}\square_{1/6}\text{I}_2)_{1/3}^-]_3)$ has increased with two orders of magnitude upon doping with silver. [250] Another path to achieve a higher electrical conductivity in the tin halide perovskite could be a postgrowth reduction of pristine or foreign cation-doped MASnI_3 . This conclusion is the same adopted by Ye *et al.*, who confirmed our measurements of the thermoelectric properties from RT to 400 K. [251]

There have been further attempt to modify the electronic properties of MASnI_3 . Doping with bismuth diminished the band gap, however increasing the residual resistivity of the material upon Bi intake. [252] Hasegawa *et al.* have also prepared $\text{MASnBr}_{3(1-x)}\text{I}_x$ and reported

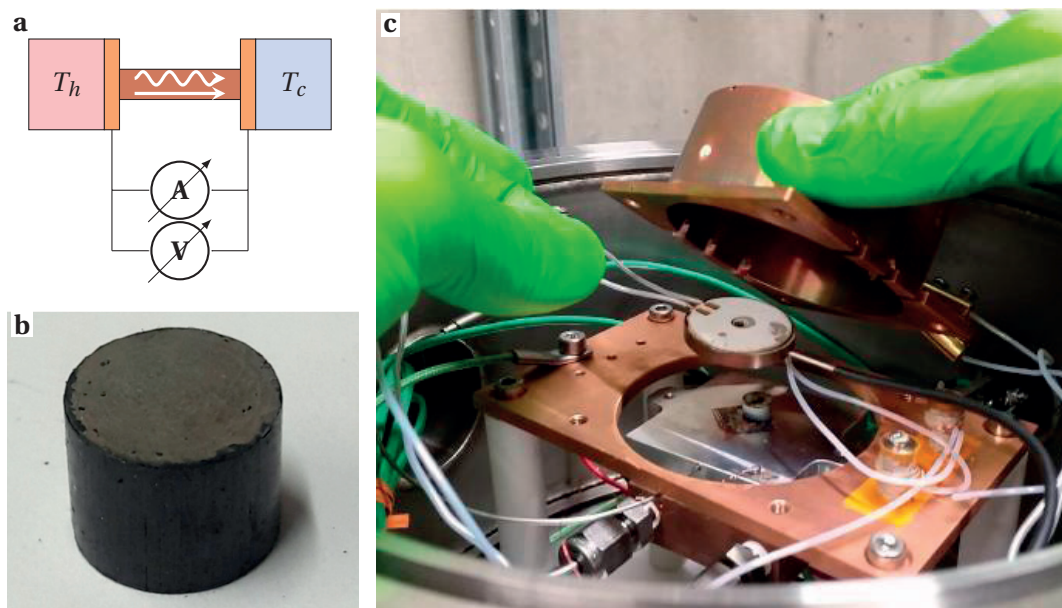


Figure 5.6 – **a** Scheme of a single-leg-thermoelectric generator, using a n-type material. The current passing through the electrodes can be recorded, as well as the voltage across them. **c** Experimental setup for direct measurements of the thermoelectric efficiency. The specimen (shown in **b**: MASnI_3) are sandwiched between a Peltier-cooled plate (below the center of the photograph) and a resistive heater (center of the image). The copper stage and cup are maintained at the temperature of the hot side to avoid dissipation via radiations.[254]

its resistivity.[253] They observed a shift towards lower values of $\rho(T)$ upon iodine doping (x). Finally, Lee *et al.* reported measurements of the transport coefficients of CsSnI_3 nanowires and found $ZT = 0.1$ at room temperature, because of the enhanced electrical conductivity and lower κ resulting from the particular geometry of nanowires.[48]

5.3 Tin-based thermoelectric devices

Encouraged by the high thermoelectric figure of merit of MASnI_3 -based materials, we propose a method capable of measuring the thermoelectric efficiency of a single-legged device directly. The opportunities to vary the chemical composition, synthesis process and micro-structure of MASnI_3 in a short time-scale pushed us to develop such system because they permit time savings compared to separate measurements of the transport properties. In addition, other important device-related questions can be tackled. For example, we reflect on the quality of thermal- and electrical- contacts on the efficiency of thermoelectric devices, and we assess ageing of the samples.

5.3.1 Thermoelectric conversion efficiency

The experimental setup (Fig. 5.6c) is inspired from the work of Kraemer *et al.*,[255] where a known thermal-energy current Q at the hot junction is applied to a single-leg device (cross section A and length L), resulting in the generation of electrical power P_{el} (Fig. 5.6a). The thermal current is flowing in a steady-state as a consequence of a temperature gradient $\Delta T = T_{\text{h}} - T_{\text{c}}$, where $T_{\text{h}}(T_{\text{c}})$ is the temperature of the hot(cold) junction. The thermoelectric conversion efficiency is the ratio of the thermal energy “current” Q and the maximal-electrical power delivered by the device:

$$\eta = P_{\text{el}}/Q. \quad (5.1)$$

Whereas P_{el} can be precisely recorded (electrical current multiplied by the voltage at the sample extremities), the estimation of Q is a more delicate task and requires a careful calibration. Measurements are made under vacuum ($p < 10^{-4}$ mbar) do avoid heat dissipation by convection. The lowest reachable T_{c} is ≈ 230 K and the maximal T_{h} is 550 K. The temperature is acquired with Type-K (ungrounded) thermocouples.

In addition to η , not only the maximal electrical power can be obtained, but also the averaged electrical resistivity of the device, its thermopower and even its thermal conductivity.[254,255] If this way can provide a good estimation of these transport coefficients, the “traditional” methods presented in Appendix A.2 remain more accurate and reliable. The largest uncertainty comes from the calibration of the thermal current at the hot side (Q). In Appendix A.3.2 it is explained how the correction factor was determined. Nonetheless, the results provided by both approaches can be compared and yield good agreement.

A typical $j - V$ curve is displayed on Figure 5.7. Such curve, taken at fixed T_{c} and T_{h} , allows us to determine three parameters. First, the open-circuit voltage V_{oc} is related to the (engineering-, see Section A.3.1) Seebeck coefficient $S_{\text{eng}}(T_{\text{h}}, T_{\text{c}}) = V_{\text{oc}}/\Delta T$. Second, if the current density is linear in V , the inverse of the slope is the resistance of the device $\rho \cdot L$, where L is the length of the leg. Third, the maximal output power density p_{max} can be determined from $j \cdot V$.⁵

5.3.2 Preparation of the samples

Three batches of powder were prepared according to two synthesis methods. In one case, MASnI_3 powder was obtained by intermixing stoichiometric amount of SnI_2 and MAI in an agate mortar (we call it sp- MASnI_3). A “doped” version of this powder was also prepared, by substituting 5 wt% of SnI_2 by BiI_3 (sp- MASnBiI_3). In the second case, a solution-grown MASnI_3 was made by reaction of Sn^{II} acetate with excess of an HI acid solution (57 wt% HI in H_2O) and a stoichiometric amount of methyl amine (MA) solution (40 wt% MA in H_2O). The black precipitate was harvested and dried, until H_2O and HI in excess were evaporated and I_2 was

⁵When j is linear in V , $p_{\text{max}} = \frac{V_{\text{oc}}^2}{4L\rho}$.

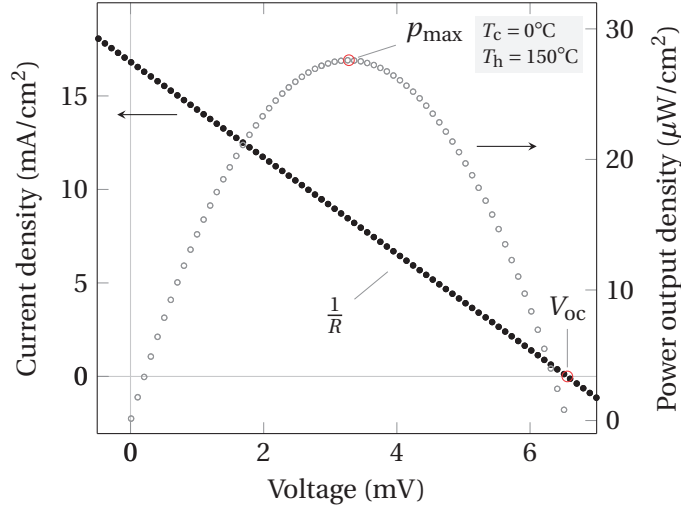


Figure 5.7 – Procedure to extract the thermoelectric efficiency of single-legged device. From the j-V characteristic, the power output density $p = j \cdot V$ can be calculated. For comparison between different specimen, we use its maximal value, p_{\max} . Other relevant characteristics can be extracted in addition. The slope of the (linear) j-V curve corresponds to the inverse of the resistance of the device (up to a geometrical factor, cross-section $A = 0.32 \text{ cm}^2$, height $h = 6.88 \text{ mm}$), and V_{oc} , the value of the voltage when the current equals zero, leads to the average thermoelectric power $S = \frac{V_{\text{oc}}}{\Delta T} = 44 \text{ } \mu\text{V/K}$. Given the heat flux $Q = 0.36 \text{ W}$ delivered by the heater, the efficiency for this ΔT is $\eta = \frac{p_{\max}}{Q} = 0.0025\%$.

sublimed (lp-MASnI₃).

MASnI₃ powders were ground and compressed in a die press (STI) of 1/4 in diameter. A typical pellet is shown on Figure 5.6b. All the powders and pellets were kept in vacuum between their transfer and preparation, and transferred to the measurement chamber on the same day of their synthesis. The pellets were mounted and attached to the electrodes by glueing them with silver-conductive paste directly. Additionally, one of the lp-MASnI₃ was pressed with Ni contacts and glued subsequently.

To probe the effect of uniaxial pressure during the preparation process, increasingly higher pressures were applied for a series of samples made of the same batch of powder. The porosity as a function of uniaxial pressure is presented in Figure 5.8a. The porosity decreases with applied pressure, reaching a few percent. Thus, at the maximal pressure allowed for the press (370 MPa), the pellet's density is very close to that of bulk MASnI₃. Simultaneously, the resistivity of the pellet was measured (Fig. 5.8b), showing that the higher pressures ensure better electrical conductivity.

Additionally, we noticed degradation of the thermoelectric conversion efficiency, for samples measured one week after their processing. This, in addition to visible colour-change of the pellet's surface prompted more careful analysis of this important issue. Figure 5.9 shows the evolution of the resistivity of one pellet over time, on a weekly scale. An increase of ρ of more than an order of magnitude occurs within two weeks, after which time the

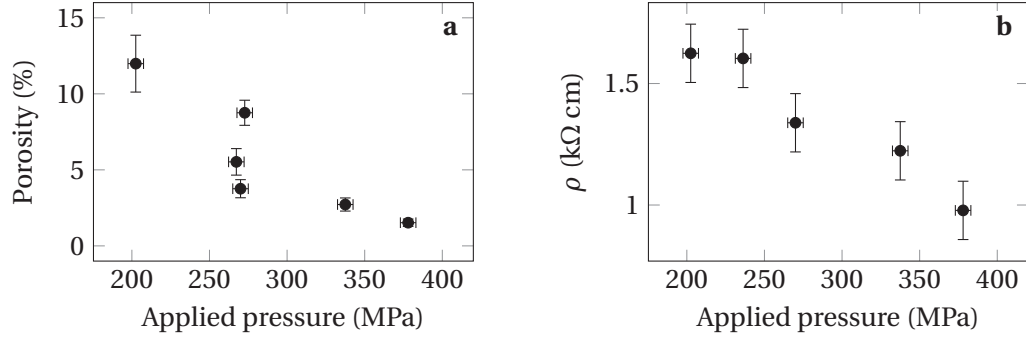


Figure 5.8 – Influence of pressure on the porosity **a** and resistivity **b** of MASnI₃ pellets.

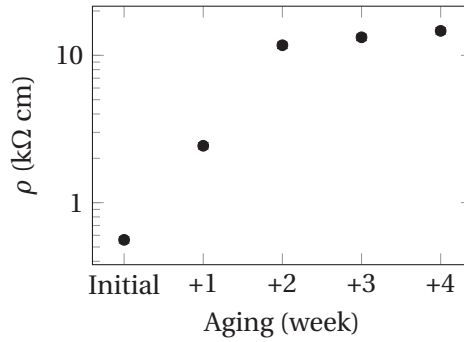


Figure 5.9 – Influence of ageing on the resistivity of a MASnI₃ pellet.

resistivity seems to saturate. This modification of the samples, even when kept in protected (dry, vacuum) atmosphere is an issue for real applications, where stability is a necessary condition for operation of devices.

5.3.3 Charge injection engineering

Like the efficiency of solar cells is conditioned by the quality of the electrodes,⁶ the performance of thermoelectric devices is strongly affected by the quality of charge collection/injection and of the thermal connexion. Indeed, a poor thermal conductivity of the electrodes will prevent heat to reach the sides of the thermoelectric leg, and poor electrical conductivity will add a load in series with the resistance of the active material, thus depleting its intrinsic quality. The choice of the electrodes also needs to take into account the chemical stability of such electrodes. In particular, ionic motion in perovskites has been reported,[256–259] and could favour chemical reaction with the electrodes. Other galvanic reactions might take place between Sn and Ag and the reactive halogen anion (AgI).

To address this issues and optimise our MASnI₃-based devices, we measured the resistivity of the same material (pressed MASnI₃ powder) sandwiched between different electrodes. Usually, silver epoxy provides very satisfying properties with other metals, including good

⁶Or their functionality, as better performances are achieved with hole-/electron- selective electrodes.

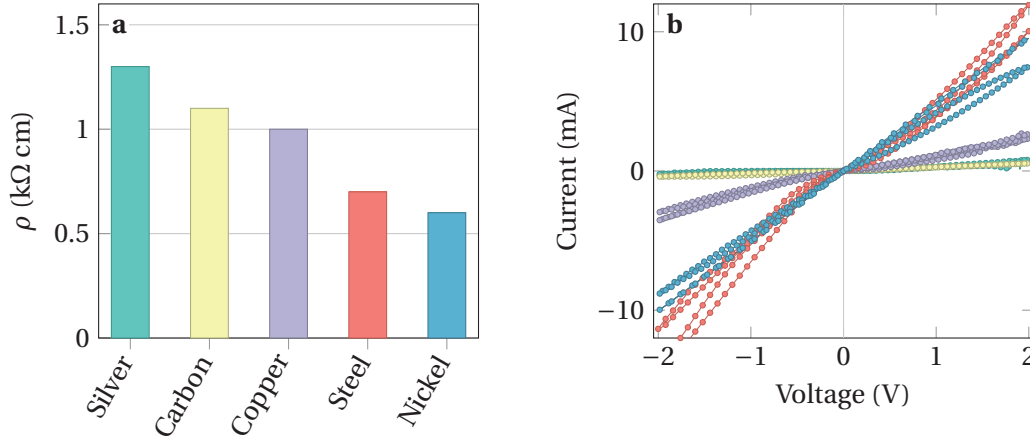


Figure 5.10 – Charge injection engineering. Resistivity of different electrodes in series with the same sp-MASnI₃ pressed powder **a** and their respective $i - V$ characteristics **b**. Even though steel electrodes display low resistivity at first, a large hysteresis and formation of bubbles at the electrodes' interfaces deteriorate their properties.

mechanical strength and low contact resistance. However, in the case of MASnI₃, the contact resistance is high. This might origin from the interaction with the solvent or formation of silver iodide. Carbon epoxy, another conductive glue that has proved more useful than its silver counterpart to measure transport in perovskites, also displays high contact resistance. Copper electrodes show ($\approx 30\%$) better performance than silver epoxy. In an effort to further decrease the contact resistance, we directly pressed steel electrodes with the MASnI₃ powder. Even though the resistivity was improved, after a few minutes, bubbles at the interfaces could be observed, indicating strong chemical (galvanic “etching”) reaction leading to degradation of the sample. Finally, the material creating least contact resistance is nickel powder, compressed directly with MASnI₃. The advantage of nickel powder, in addition to minimise the contact resistance with respect to other metals, is that it can be directly, mechanically connected to the sample, without any supplementary step. The resistivities of devices with different electrodes can be compared in Figure 5.10.

5.3.4 Energy-conversion efficiency

The thermoelectric-conversion efficiency η of four MASnI₃-based devices, obtained for different temperatures and thermal gradients are presented on Figure 5.11. The thermoelectric conversion efficiency η ranges from $10^{-5}\%$ to 0.003%, and strongly depends on ΔT and on the average temperature T_{avg} . Unsurprisingly the largest efficiencies are obtained when the thermal gradient is the highest (Eq. (A.5)). In order to better understand the reasons behind these large variations in η , the resistivity and thermoelectric power of the devices were also acquired.

First the electrical resistivity ρ of the devices reproduces the trends of Figure 5.3, with insulating samples sp-MASnI₃ and lp-MASnI₃ progressively becoming more metallic (Ni

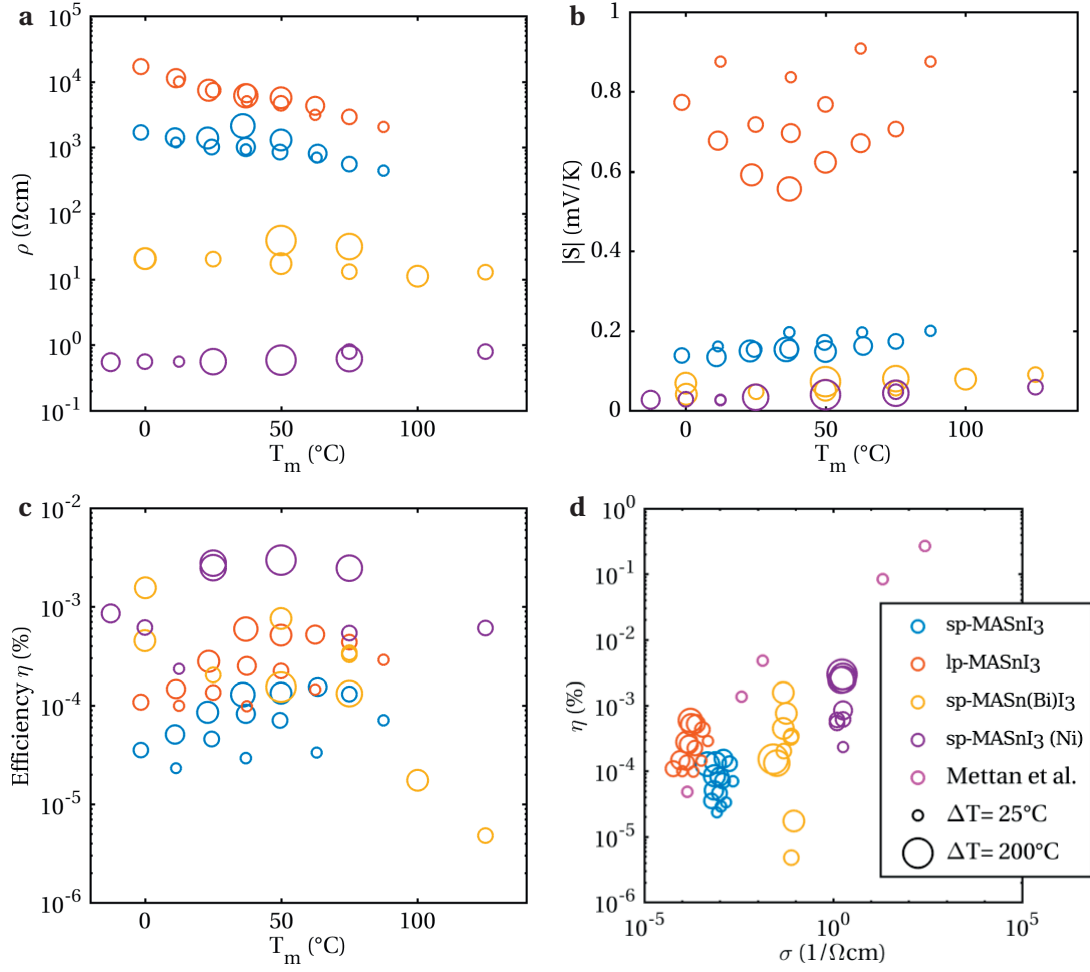


Figure 5.11 – Thermoelectric properties of MASnI₃ devices. The size of the circle is proportional to the temperature difference ΔT applied across the sample, the smallest being 25 K and the largest 200 K. **a** Resistivity and **b** Seebeck coefficient of the devices as a function of the average temperature ($T_m = T_{\text{avg}}$). Thermoelectric conversion efficiency η as a function of **c** the average temperature and **d** the electrical conductivity.

contacts). It is clear from this graph that the nickel contacts drastically decreases the contact resistance, thus allowing better performance.

The distribution of the Seebeck coefficient indicate that $S(T)$ of the lp-MASnI₃ pellet has a maximum between 340 and 380 K. Its very high value corresponds well to that measured by the “conventional” method. For the other samples, the absolute value is lower, especially for the sample doped with bismuth; however the relative change in S from sample to sample is much smaller in magnitude than the change in ρ . Therefore, as suggested in Ref. 230, at this point of the development of MASnI₃ thermoelectric devices, the bottleneck is the high electrical resistivity of the samples and contacts, yet too high to permit their use in applications. Figure 5.11d shows this trend, as η tend to be enhanced with the electrical conductivity. Using Equation (A.4) with $T_h = 290$ K and $T_c = 265$ K, the conversion efficiency for an ideal device (perfect thermal anchoring of the sample, without contact resistance) can be estimated from the results of Figure 5.5. The highest predicted value is issued for the samples of Takahashi *et al.*, [234], with $\eta = 0.4\%$. If this number could be measured directly this would be a first proof of concept for MASnI₃-based thermoelectric applications.

5.4 Conclusions

The transport coefficients of hybrid-halide perovskites MAPbI₃, MAPbBr₃ and MASnI₃ were measured over a wide temperature range and allow us to understand better the mechanisms governing the outstanding performances of these materials. Along with the rapid development of novel technologies relying on these materials, the deep knowledge of the physical phenomena underlying the operation of devices is required. In particular, thermal conductivity has to be taken into account for thermal management, as overheating of a device can irreversibly damage it; conversely, if κ is not correctly suited to the application it could lead to (thermal) energy losses. With our careful and very accurate measurements of the transport coefficients, we establish a basic understanding for more complex phenomena in hybrid halide perovskites. The very low κ , explained by the low speed of sound in these compounds and the dynamics of the organic cations is tightly linked to the formation of large polarons. The polarons themselves promote exceptionally long carrier-recombination rates, long-carrier-diffusion lengths and low mobilities, at the origin of many of the optoelectronic features of hybrid halide perovskites.[243,260–262]

Furthermore, inspired by theoretical calculations,[13,247] the thermoelectric figure of merit could be calculated and the good performance of MASnI₃ as a thermoelectric was highlighted. The high value of $ZT = 0.13$ for the most conductive MASnI₃ specimen, obtained without any specific engineering is very promising and should encourage to explore chemical doping of this material. In order to consolidate our results, we constructed a setup to assess the thermoelectric-conversion efficiency directly. This brought us to consider, in addition to optimising the thermoelectric properties of the core material MASnI₃, more device-oriented problems. Hence the benefit of nickel electrodes directly pressed with MASnI₃ powder has

been demonstrated. Although there are still important issues regarding the stability of MASnI_3 , ageing too rapidly, chemical doping, could improve not only the electrical conductivity but also the chemical stability, in a similar fashion as for solar cells.[263,264]

The maximum conversion efficiency that we demonstrated for a single-leg device has yet only reached a few tens of a percent, a value too low to be converted into mechanical work or for thermoelectric cooling. Nevertheless, this performance is largely enough to power a wireless communications or for “personal” micropower.[265] Indeed, self-powered sensors using the thermal gradient between the temperature of a body and surrounding atmosphere have numerous potential applications, like real-time monitoring of vital signals. The recent progress in inkjet printing of perovskites solar cells could have important implications for the design of wearable thermoelectric devices, and thus devise very promising prospects for the development of MASnI_3 -based, flexible thermoelectric devices.[211,266]

General conclusions and outlook

The careful measurement of the transport coefficients enabled me to probe and describe very interesting effects in functional materials. The main contributions of this work are the following:

- A new mechanism strongly reducing the whole temperature dependence of the thermal conductivity of anatase TiO_2 was discovered. It arises from the resonant interaction of localised-charged defects with the vibrations of the crystal lattice. I observed and described this effect in anatase, with two type of defects: oxygen vacancies and fluorine dopants. Nonetheless the model that we derived is relevant to any kind of defects, provided that they are charged and localised.
- I recognised the low thermal conductivity of mayenite, MAPbI_3 , MAPbBr_3 and MASnI_3 to be a consequence of the vibrational modes of anions/cations enclosed in a cage-like structure. In these materials, the heat-carrying phonons propagate via the framework, however they interact resonantly with the vibrating anions/cations.
- I demonstrated that providing a maximal disorder in the arrangement of atoms decreases the thermal conductivity of the phonon system in high-entropy alloys.
- Strategies for texturing known materials in order to minimise their thermal conductivities have been explored. The inclusion of voids (foam) was confirmed to renormalise the thermoelectric properties of aluminium-alloy foams. An efficient way to control the size of the bubbles is defined with acoustic pressure. Moreover, by reducing the effective dimensionality of the phonon-density of states in anatase foams, the thermal conductivity can be diminished by three orders of magnitude.
- Original experimental data are documented for the first time for nearly all materials presented in this Thesis. Because these materials are used/foreseen in applications, the corresponding data are of very practical use for better packaging or integration of the compounds in real devices. Furthermore, I uncovered the potential of new candidates such as FeNi alloys for applications in thermoelectric conversion.
- The anomalous temperature dependence of the low Seebeck coefficient in the series of high-entropy alloys was revealed. This finding calls for a detailed theoretical studies to try to unmask its origin.

Conclusions and outlook

Many of the materials presented here, because they have low κ and a moderate Seebeck coefficient, could be interesting for thermoelectric applications, if one could render them more conductive. This is the real challenge in developing thermoelectric materials: finding the balance between the different “ingredients”, i.e. between the transport coefficients. Since the first appearance of thermoelectric applications (e.g. power generators for space exploration[267]) progresses have been much slower than, e.g., in photovoltaics. Indeed, research into thermoelectric materials is tedious: the detailed measurements of the thermoelectric coefficients are time-consuming and prone to errors. Moreover, unlike for solar cells, there is no systematic and certified procedure to assess $(ZT)_{\text{eng}}$, so that there can be large deviations between the reported values of ZT . Setup for direct characterisation of the thermoelectric efficiency bring thermoelectric technologies closer to this standard and closer to applications. Performing direct measurements of the thermoelectric efficiency has many advantages, such as faster acquisition rate and an opportunity to address challenges related to device operation (charge injection, thermal contacts, etc.) at an early stage. In future research, I aim to systematically investigate potential thermoelectric materials, as it is a clear gain of resources and time. Further development of benchtop characterisation apparatus should be encouraged, along with discussions to elaborate standard procedures (similar to solar-cell certifications).

Even though thermoelectricity may not solve all the energy-production issues, development of new thermoelectric compounds for sustainable power production could significantly contribute to global efforts to eliminate fossil energies. I believe that our original research can impact the understanding of thermoelectric effects, in addition to fostering technological progress in thermoelectric applications.

A Experimental methods

A.1 Control of the temperature

Samples were cooled down to liquid-helium temperature (4.2 K) by directly dipping the sample stage inside the refrigerant, or thanks to a closed-cycle cryostat (ARS DE210). The temperature was controlled with Lakeshore temperature controllers (Model 331,332,340) with a feedback loop (PID) piloting 50 Ω heaters. All sample stages can be evacuated to levels lower than 10^{-5} mbar. For temperatures higher than room-temperature, tube furnaces were employed, with a maximum temperature of 1000°C. The tubes can be evacuated to high vacuum levels, or a process gas can be flown inside (Argon, nitrogen, helium, oxygen, hydrogen, or a mixture of these gases).

For thermoelectric power, thermal conductivity and thermoelectric efficiency, specialised setups were employed to detect the small thermal gradients on samples. For the two former, custom-made, differential type-E thermocouples from 50 μm -diameter-wires; the thermal gradient applied was always kept below 1 K. For the latter, the temperature was measured directly with type-K thermocouples, at the cold side, hot side and thermal shield, using simulated junctions.

A.2 Transport coefficients

A.2.1 Resistance

To measure electrical resistances below 1 G Ω , a steady-state, four-point technique was used. Usually the samples can be cut or polished to obtain well-defined geometries (rectangular- or circular- constant cross-section. A typical geometry is detailed on Figure A.1a. Gold is the material of choice for electrical connections to the sample. A software permits us to control the temperature changes and to acquire the data in real time.

For samples with higher resistivities ($> 1 \text{ G}\Omega$), an alternating polarity, two-point, steady-

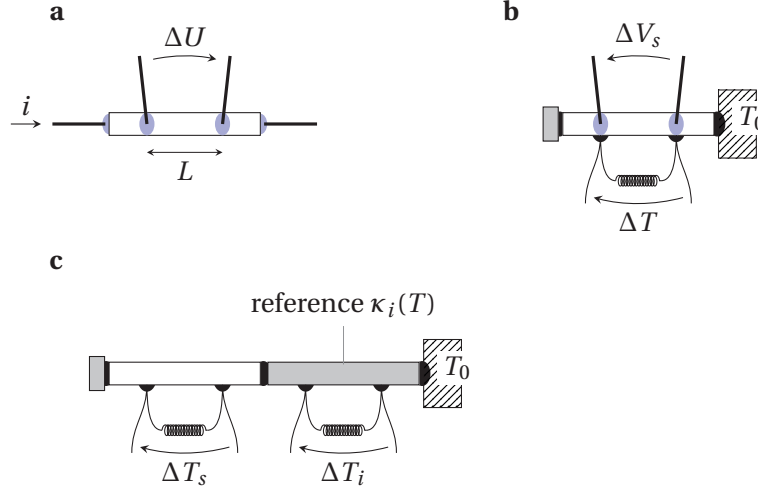


Figure A.1 – Experimental configuration for the measurements of thermoelectric properties. The sample (white rectangle) has a regular cross-section of area A . Electrical wires are usually connected by conductive epoxy (silver or carbon), but they can also be welded to the sample (light blue shade). Thermal contacts can be made with silver epoxy if electrical contact is allowed. Conversely, Stycast 2859 FT permits thermal anchoring without charge transfer (black areas). **a** For electrical resistivity, a current i is forced through the sample and the potential drop ΔU across two other points separated by L along the cross-section is recorded, so that the resistance of the wires and contacts can be discarded. Then $\rho = \frac{A}{L} \cdot \frac{i}{\Delta U}$. **b** Here, as a thermal gradient across the sample is required, a current is sent to a resistive heater (left grey rectangle) so that the temperature on one side of the sample is higher than T_0 , the “bath” temperature. The voltage drop ΔV_s is recorded from the same two points where a differential type-E thermocouple measures the temperature difference. The Seebeck coefficient is $S = \frac{\Delta V_s}{\Delta T}$. **c** An inox reference of calibrated $\kappa_i(T)$ permits the measurement of κ . The heat flux Q generated by the resistive heater is assumed to propagate from sample to reference without losses, so that $\kappa = \kappa_i \cdot \frac{L_s A_i}{A_s L_i} \frac{\Delta T_i}{\Delta T_s}$. An optical picture of a sample prepared for measurement can be seen on Fig. A.2.

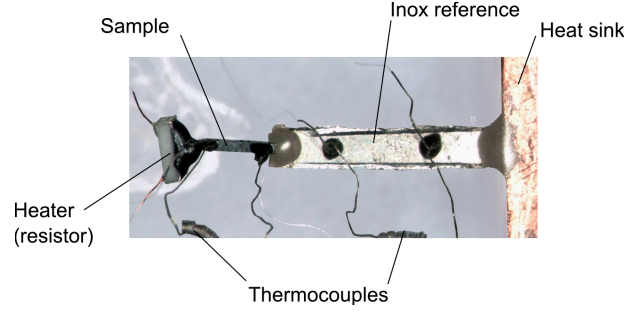


Figure A.2 – Photography of a bar-shaped sample prepared for a measurement of thermal conductivity.

state method was developed, using an electrometer, able to detect femto-Amperes. In this case, a voltage is applied accross the sample and the current is recorded. Low-noise-shielded cables were employed to avoid parasitic-capacitive effects in addition to proper shielding of the sample-holder.

A.2.2 Seebeck coefficient

The settings for measurements of the seebeck coefficient S is sketched on Figure A.1b. Here, for values of S lower than $100 \mu\text{V/K}$, the measured values S_{meas} is systematically corrected for the contribution of the gold leads ($S = S_{\text{meas}} + S_{\text{Au}}$). The Au-wires are made of high purity and their S_{Au} is precisely calibrated.

For the measurement of the Seebeck coefficient of MAPbI_3 and MASnI_3 (Section 5.2.2), a more sophisticated method was employed. A temperature gradient was imposed by a resistive heater attached to one extremity of the sample, driven by an alternating current of frequency $f = 60 \text{ MHz}$. The temperature gradient across the sample was measured by a Chromel-Constantan (Type E) differential thermocouple, using a lock-in amplifier at $2f$. The temperature gradient was carefully set to be smaller than 1 K . The thermoelectric voltage was amplified by a Keithley 6517 electrometer and determined using a lock-in amplifier at $2f$.

A.2.3 Thermal conductivity

A picture of a sample prepared for a measurement of κ is shown on Figure A.2, and a scheme of the situation on Figure A.1c. A chip resistor ($\sim 100 - 1000 \Omega$) is glued onto one end of the sample using Stycast FT 2850. In order to measure the amount of heat passing through the specimen, a stainless steel (inox) reference sample of known $\kappa_i(T)$ is connected between the sample and the copper sample holder, which acts as a heat sink. Temperature gradient in both elements is measured by Chromel-Constantan (type-E) differential thermocouples. These are fabricated using $20 \mu\text{m}$ -thick wires to reduce the evacuation of heat through them. Care was taken to maintain a temperature gradient of 1 K across the samples at all temperatures.[153]

In a sense, our way to probe κ is a 4-point, steady-state technique, where the energy

current in the form of heat Q is measured by two points (inox reference thermocouple and calibration) and the thermal gradient is obtained by two other leads (sample thermocouple).

A.3 Thermoelectric devices

A.3.1 Engineering values

The figure of merit ZT , as defined in Equation (1.38), is very useful to assess the quality of a thermoelectric material. However, it does not mirror accurately the performances of a material in a thermoelectric device, because it casts the effects of the temperature difference aside. Indeed, on the hot side, the thermoelectric properties of a given material can have different values than on the cold side, especially when ΔT exceeds a few Kelvins. Taking this into account, one is able to define *average* and *engineering* quantities, that translate to more correct estimations of the thermoelectric efficiency of a TEG.

For more clarity, we call the average temperature of the junction $T_{\text{avg}} = 1/2 \cdot (T_h + T_c)$, where T_h and T_c are the temperature of the hot and cold reservoirs, respectively. It follows that $\Delta T = T_h - T_c$, and ZT in Equation (1.38) can be written as $ZT = ZT(T) = \frac{\sigma(T) \cdot S^2(T)}{\kappa(T)} \cdot T$. The *maximal* thermoelectric efficiency is:[268]

$$\eta_{\text{max}} = \eta_c \cdot \frac{\sqrt{1 + ZT} - 1}{\sqrt{1 + ZT} + T_h / T_c} \quad (\text{A.1})$$

where $\eta_c = \Delta T / T_h$ is the Carnot (maximal) efficiency. This quantity is referred as maximal because $ZT(T)$ usually has a maximum in the temperature range considered for applications, so that averaging ZT over ΔT would give a lower value of the thermoelectric efficiency. Beyond averaging, the most precise way to predict the thermoelectric efficiency of a material, knowing the temperature-dependent-thermoelectric coefficients, is the engineering figure of merit $(ZT)_{\text{eng}}$:[269]

$$(ZT)_{\text{eng}} = \frac{\sigma(T_c, T_h) S^2(T_c, T_h)}{\kappa(T_c, T_h)} \cdot \Delta T, \quad (\text{A.2})$$

where the average value $C(T_c, T_h)$ of the thermoelectric coefficient C is defined as follow:

$$C(T_c, T_h) = \frac{1}{\Delta T} \int_{T_c}^{T_h} C(T') dT'. \quad (\text{A.3})$$

In this case, the maximal efficiency yields:

$$\eta_{\text{eng}} = \eta_c \cdot \frac{m_{\text{opt}} - 1}{\hat{\alpha}(m_{\text{opt}} + 1) - \eta_c}, \quad (\text{A.4})$$

with $m_{\text{opt}} = \sqrt{1 + (ZT)_{\text{eng}} \left(\frac{\hat{\alpha}}{\eta_c} - \frac{1}{2} \right)}$ and $\hat{\alpha} = \frac{S(T_h)}{S(T_c, T_h)}$ the intensity of the Thomson effect.[269]

Here, for small values of $(ZT)_{\text{eng}}$, Equation (A.4) simply becomes:

$$\eta_{\text{eng}} \simeq \frac{1}{4} \cdot (ZT)_{\text{eng}} = \frac{1}{4} \cdot \frac{\sigma(T_c, T_h) S^2(T_c, T_h)}{\kappa(T_c, T_h)} \cdot \Delta T. \quad (\text{A.5})$$

Whereas η_{eng} can be calculated from $(ZT)_{\text{eng}}$, the opposite is not possible without prior knowledge of $\hat{\alpha}$. Instead, one can obtain the average figure of merit ZT_{avg} from the efficiency in the following way:

$$(ZT)_{\text{avg}} = \left(\frac{\Delta T + \eta T_c}{\Delta T - \eta T_h} \right)^2 - 1 \quad (\text{A.6})$$

$$= \frac{\eta(2 - \eta)(T_h^2 - T_c^2)}{[T_h(1 - \eta) - T_c]^2} \quad (\text{A.7})$$

$$\simeq 2\eta \cdot \frac{T_h + T_c}{\Delta T} = 4\eta \cdot \frac{T_{\text{avg}}}{\Delta T} \quad (\text{A.8})$$

where the last equality holds if $\eta \ll 1$ ($\eta < 2\%$).

A.3.2 Correction factor

In order to estimate correctly the heat transferred at the hot junction, we calibrated the setup with a reference material, Bi_2Te_3 pellet. To do so, Bi_2Te_3 powder was compressed into a pellet and the three temperature-dependent transport coefficients of this specimen were measured in the relevant temperature range, according to the methods presented in Appendix A.2. Then, the engineering values can be calculated and compared to the one obtained by direct measurement.

The electrical power output of the heater is related to the heat current Q at the hot junction as follow:

$$Q = \alpha \cdot P_H = \alpha \cdot iV, \quad (\text{A.9})$$

where α is the correction factor, i and V are the electrical current and voltage supplied to the heater, respectively. Therefore, in order to calibrate the setup, we measure the efficiency of our Bi_2Te_3 pellet without correction:

$$\eta_{\text{meas}} = \frac{P_{\text{TE}}}{P_H} \quad (\text{A.10})$$

and we compare this value to the η_{eng} extracted from the separately measured thermoelectric coefficients, calculated from Equation (A.4). This procedure finally enables us to obtain α as a function of T_h :

$$\alpha(T_h) = \frac{\eta_{\text{meas}}}{\eta_{\text{eng}}}. \quad (\text{A.11})$$

Appendix A. Experimental methods

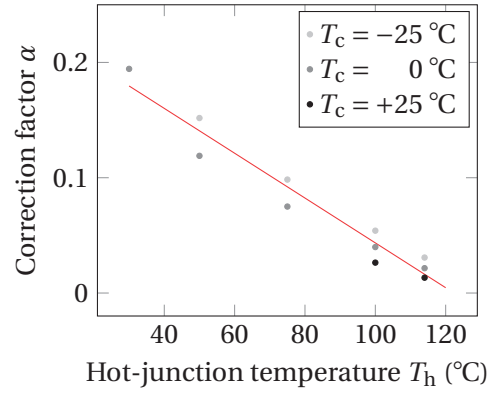


Figure A.3 – Calibration of the heat current. For subsequent experiments, a linear relation was used to map α to the hot-junction temperature T_h : $\alpha(T_h) \simeq 0.77 - 0.0019 \cdot (T_h + 273.15)$. This equation corresponds to the solid line on the plot.

Once α is determined, any new material can be probed and a realistic value of η can be found dividing η_{meas} by α . The results for our setup are displayed in Figure A.3. We used a linear least-square regression to obtain $\alpha(T_h) \simeq 0.77 - 0.0019 \cdot (T_h + 273.15)$.

B Apparent surface tension at interfaces with solid particles

In this appendix we explore the influence of solid particles diluted in a liquid phase on the wetting properties of liquid/gas or liquid/solid or 3-phase line interfaces. The results presented here help understanding the low surface-tension coefficient γ obtained for the aluminium-matrix-composite in the frame of the formation of bubbles, as discussed in section 3.2.2.

Clean liquid/gas surfaces have their own surface tension coefficient γ (J/m²). This is the extra-surface-Gibbs energy per unit-surface area of the liquid/vapour interface. However, the liquid surface can be partly covered by small solid particles, like in Figure B.1, yielding a measured *apparent* surface tension γ_{ap} .

When the liquid surface is partly covered by solid particles, its apparent surface tension is expected to be smaller compared to the surface tension of the interface without particles, as the apparent-liquid surface (A_{ap}) is smaller than that of the total-liquid surface without particles (A_0). Particles will influence the measured apparent surface tension only if their size is much smaller than the length-scale of the surface-tension measurement. In the first approximation the characteristic size of the particles can be compared to the capillary length defined as $L_{cap} = \sqrt{\gamma/\rho g}$, where ρ (kg/m³) is the density of the liquid, $g = 9.81$ m/s² is the acceleration due to gravity. For water and liquid Al, $L_c = 2.7$ mm and 6.7 mm, respectively. Thus, solid particles with characteristic sizes smaller than 0.1 mm will play a role in decreasing the surface tension. This discussion is valid only for small particles (< 0.1 mm), where the usual particle size of reinforcing particles in metal matrix composites and in particle-stabilized-

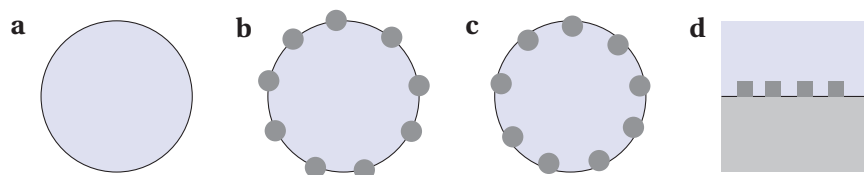


Figure B.1 – Liquid droplets with clean surface **a** and with partly covered surfaces by particles **b,c** with contact angle of the liquid on particles about 90 degrees **b** and close to 0 degree **c**. Liquid-solid interface **d** with cubic-like particles at the interface.

Appendix B. Apparent surface tension at interfaces with solid particles

liquid metallic foams. Regarding these conditions, the change in surface tension only depends on the difference between “active” surfaces:

$$\frac{\gamma_{\text{ap}}}{\gamma} = \frac{A_{\text{ap}}}{A_0}. \quad (\text{B.1})$$

From Eq. (B.1) the apparent surface tension can be expressed as:

$$\gamma_{\text{ap}} = (1 - f_{\text{cov}}) \cdot \gamma \quad (\text{B.2})$$

where $f_{\text{cov}} := 1 - \frac{A_{\text{ap}}}{A_0}$ (dimensionless) is the coverage factor of the liquid surface by the particles. If the liquid surface is clean, then $f_{\text{cov}} = 0$, while spherical particles of equal diameter can reach the maximum of $f_{\text{cov}} = 0.906$.

The “geometrical” coverage factor f_{geo} (dimensionless) is defined as the coverage factor corresponding to an area covered with particle’s maximal-cross section.

B.1 Spherical particles at a liquid-gas interface

First, we consider spherical particles of radius r (m). In this case, the ratio of the actual-surface coverage to the geometrical-surface coverage is written as the ratio of the surface of the liquid actually covered by a spherical particle to the maximum cross sectional area of the particle:

$$\frac{f_{\text{cov}}}{f_{\text{geo}}} = \frac{2rh - h^2}{r^2}, \quad (\text{B.3})$$

where h is the depth of immersion of a spherical particle of radius r below the surface of the liquid (into the liquid). Recalling that the contact angle has an influence on the immersion depth of the particle, its equilibrium value is written as:[270]

$$h_{\text{eq}} = r \cdot (1 + \cos \Theta), \quad (\text{B.4})$$

where Θ (degrees) is the contact angle of the liquid on the solid particles in the equilibrium vapour environment. Eq. (B.4) is applicable when the effects of gravity and other forces (except the interfacial forces) are neglected (valid for small particles). Substituting Eq. (B.4) into Eq. (B.3):

$$\frac{f_{\text{cov}}}{f_{\text{geo}}} = 1 - \cos^2 \Theta. \quad (\text{B.5})$$

Now, let us express f_{cov} from Eq. (B.5) and let us substitute this expression into Eq. (B.2):

$$\gamma_{\text{ap}} = [1 - f_{\text{geo}}(1 - \cos^2 \Theta)] \cdot \gamma. \quad (\text{B.6})$$

The ratio of the apparent surface tension to the surface tension of the liquid as function of f_{geo} and the contact angle is shown in Figure B.2, calculated by Eq. (B.6). As follows from Eq. (B.6)

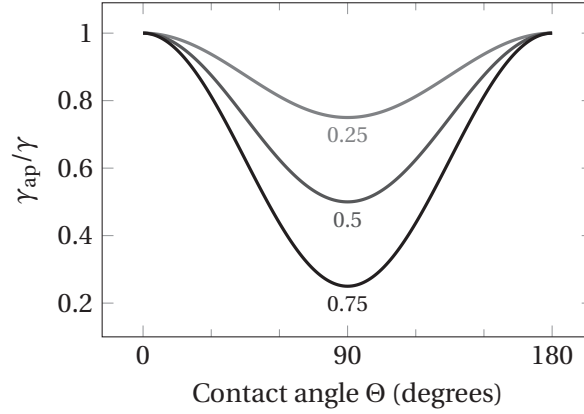


Figure B.2 – Ratio of apparent to the actual surface tensions γ_{ap}/γ as a function of the contact angle Θ for different values of the geometrical-surface coverage f_{geo} of the liquid surface by solid particles, calculated from Eq. (B.6).

and Figure B.2:

- The largest decrease of surface tension due to particles is obtained for 90 degrees of contact angle; according to Eq. (B.4), such particles are immersed half into the liquid, and therefore they cover the largest possible surface area of the liquid, being equal to their maximum cross-sectional area.
- The contact angle dependence of the ratio of the apparent to the real surface tensions is a symmetrical function around the central contact angle value of 90 degrees.
- At contact angles of 0 and 180 degrees the apparent surface tension equals the real surface tension at any geometrical coverage of the liquid by the particles: at these contact-angle values the particle is fully immersed in the liquid or in a gas phase, thus it does not cover any area of the liquid surface (see Eq. (B.4)).

These considerations hold for liquid/liquid interfaces as well.

B.2 Solid particles at a liquid-solid interface

For liquid/solid interfaces, and with the characteristic dimension of the solid particles smaller than L_c , the problem is more straightforward than in the previous section. f_{cov} in Equation (B.2) is related to the amount of solid surface in direct contact with solid particles. For spherical particles, $f_{cov} \leq 1$. For cubic particles, $0 < f_{cov} < 1$, which is the case of SiC particles in aluminium-matrix composites (Figure B.1d).

Regarding the case of a three-phase line, Equation (B.2) still holds, with the coverage factor defined as $f_{cov} = 1 - \frac{L_{ap}}{L_0}$, where L has the dimension of a length. Thus, for the circular

Appendix B. Apparent surface tension at interfaces with solid particles

orifice of the injector, value of γ_{ap} can be understood in terms of partial coverage of the orifice perimeter by the MMC melt.

Bibliography

- [1] Goldemberg, Jose, Thomas B. Johansson, Amulya K. N. Reddy, R. H. W. *Energy for a Sustainable World* (University of Virginia, 1988).
- [2] Snyder, G. J. & Toberer, E. S. Complex thermoelectric materials. *Nature materials* **7**, 105–14 (2008).
- [3] Tong, X. C. *Advanced Materials for Thermal Management of Electronic Packaging*, vol. 30 of *Springer Series in Advanced Microelectronics* (Springer New York, New York, NY, 2011).
- [4] Papadopoulos, A. State of the art in thermal insulation materials and aims for future developments. *Energy and Buildings* **37**, 77–86 (2005).
- [5] Balandin, A. A. Thermal properties of graphene and nanostructured carbon materials. *Nature Materials* **10**, 569–581 (2011).
- [6] Li, S. *et al.* High thermal conductivity in cubic boron arsenide crystals. *Science* **361**, 579–581 (2018).
- [7] Kang, J. S., Li, M., Wu, H., Nguyen, H. & Hu, Y. Experimental observation of high thermal conductivity in boron arsenide. *Science* **361**, 575–578 (2018).
- [8] Dames, C. Ultrahigh thermal conductivity confirmed in boron arsenide. *Science* **361**, 549–550 (2018).
- [9] Graebner, J. E., Jin, S., Kammlott, G. W., Herb, J. A. & Gardinier, C. F. Large anisotropic thermal conductivity in synthetic diamond films. *Nature* **359**, 401–403 (1992).
- [10] Huang, X., Liu, G. & Wang, X. New Secrets of Spider Silk: Exceptionally High Thermal Conductivity and Its Abnormal Change under Stretching. *Advanced Materials* **24**, 1482–1486 (2012).
- [11] Shen, S., Henry, A., Tong, J., Zheng, R. & Chen, G. Polyethylene nanofibres with very high thermal conductivities. *Nature Nanotechnology* **5**, 251–255 (2010).
- [12] Green, M. A., Ho-Baillie, A. & Snaith, H. J. The emergence of perovskite solar cells. *Nature Photonics* **8**, 506–514 (2014).

Bibliography

- [13] He, Y. & Galli, G. Perovskites for Solar Thermoelectric Applications: a First Principle Study of $\text{CH}_3\text{NH}_3\text{Al}_3$ (A=Pb and Sn). *Chemistry of Materials* **26**, 5394–5400 (2014).
- [14] The Editors of Encyclopaedia Britannica. Transport phenomenon (1998). URL <https://www.britannica.com/science/transport-phenomenon>.
- [15] Behnia, K. *Fundamentals of Thermoelectricity* (Oxford University Press, 2015).
- [16] Zlatić, V. & Monnier, R. *Modern theory of thermoelectricity* (2014), oxford uni edn.
- [17] Ziman, J. M. *Electrons and Phonons: The Theory of Transport Phenomena in Solids*. International series of monographs on physics (OUP Oxford, 2001).
- [18] Berman, R. R. *Thermal conduction in solids* (Clarendon Press, 1976).
- [19] Tritt, T. M. *Thermal conductivity : theory, properties, and applications* (Kluwer Academic/Plenum Publishers, New York, 2004).
- [20] Groot, S. R. d. S. R. & Mazur, P. P. *Non-equilibrium thermodynamics* (Dover Publications, New York, 1984), dover ed. edn.
- [21] Tritt, T. M. (ed.) *Thermal Conductivity*. Physics of Solids and Liquids (Springer US, 2004).
- [22] Ashcroft, N. W. & Mermin, N. D. *Solid state physics* (Holt, Rinehart and Winston, 1976), 33, illust edn.
- [23] Lee, S. *et al.* Anomalously low electronic thermal conductivity in metallic vanadium dioxide. *Science* **355**, 371–374 (2017).
- [24] Johansson, C. H. & Linde, J. O. Röntgenographische und elektrische Untersuchungen des CuAu-Systems. *Annalen der Physik* **417**, 1–48 (1936).
- [25] Callen, H. B. The application of onsager's reciprocal relations to thermoelectric, thermomagnetic, and galvanomagnetic effects. *Physical Review* **73**, 1349–1358 (1948).
- [26] Lindsay, L. First Principles Peierls-Boltzmann Phonon Thermal Transport: A Topical Review. *Nanoscale and Microscale Thermophysical Engineering* **20**, 67–84 (2016).
- [27] Maldovan, M. Phonon wave interference and thermal bandgap materials. *Nature Materials* **14**, 667–674 (2015).
- [28] Callaway, J. Model for Lattice Thermal Conductivity at Low Temperatures. *Physical Review* **113**, 1046–1051 (1959).
- [29] Thurber, W. R. & Mante, A. J. H. Thermal Conductivity and Thermoelectric Power of Rutile TiO_2 . *Physical Review* **139**, A1655–A1665 (1965).
- [30] Tse, J. S. & White, M. A. Origin of glassy crystalline behavior in the thermal properties of clathrate hydrates: A thermal conductivity study of tetrahydrofuran hydrate. *Journal of Physical Chemistry* **92**, 5006–5011 (1988).

-
- [31] Pohl, R. O. Thermal conductivity and phonon resonance scattering. *Physical Review Letters* **8**, 481–483 (1962).
- [32] Zakrzewski, M. & White, M. A. Thermal conductivities of a clathrate with and without guest molecules. *Physical Review B* **45**, 2809–2817 (1992).
- [33] Goupil, C. Thermodynamics of Thermoelectricity. In *Thermodynamics* (InTech, 2011). URL <http://www.intechopen.com/books/thermodynamics/thermodynamics-of-thermoelectricity>.
- [34] Goupil, C. *et al.* Thermodynamics and Thermoelectricity. In *Continuum Theory and Modeling of Thermoelectric Elements*, 1–74 (Wiley-VCH Verlag GmbH & Co. KGaA, Weinheim, Germany, 2015). URL <http://doi.wiley.com/10.1002/9783527338405.ch1>. arXiv:1011.1669v3.
- [35] Vining, C. B. An inconvenient truth about thermoelectrics. *Nature Materials* **8**, 83–85 (2009).
- [36] Callen, H. B., Callen, H. B., of Australia. Research Division, N. F. R. C. & Sons, W. & *Thermodynamics and an Introduction to Thermostatistics* (Wiley, 1985).
- [37] Tritt, T. M. & Subramanian, M. a. Thermoelectric Materials, Phenomena, and Applications: A Bird's Eye View. *MRS Bulletin* **31**, 188–198 (2006).
- [38] Hochbaum, A. I. *et al.* Enhanced thermoelectric performance of rough silicon nanowires. *Nature* **451**, 163–167 (2008).
- [39] Toberer, E. S., Zevalkink, A. & Snyder, G. J. Phonon engineering through crystal chemistry. *Journal of Materials Chemistry* **21**, 15843 (2011).
- [40] Zhao, L.-D. *et al.* Ultrahigh power factor and thermoelectric performance in hole-doped single-crystal SnSe. *Science* **351**, 141–144 (2016).
- [41] Guo, R. & Huang, B. Approaching the alloy limit of thermal conductivity in single-crystalline Si-based thermoelectric nanocomposites: A molecular dynamics investigation. *Scientific Reports* **5**, 9579 (2015).
- [42] Ravichandran, J. *et al.* Crossover from incoherent to coherent phonon scattering in epitaxial oxide superlattices. *Nature Materials* **13**, 168–172 (2014).
- [43] Poudel, B. *et al.* High-Thermoelectric Performance of Nanostructured Bismuth Antimony Telluride Bulk Alloys. *Science* **320**, 634–638 (2008).
- [44] Nolas, G. S., Poon, J. & Kanatzidis, M. G. Recent Developments in Bulk Thermoelectric Materials. *MRS Bulletin* **31**, 199–205 (2006).
- [45] Xie, H. *et al.* Beneficial contribution of alloy disorder to electron and phonon transport in half-Heusler thermoelectric materials. *Advanced Functional Materials* **23**, 5123–5130 (2013).

Bibliography

- [46] Pisoni, A. *et al.* Ultra-Low Thermal Conductivity in Organic–Inorganic Hybrid Perovskite $\text{CH}_3\text{NH}_3\text{PbI}_3$. *The Journal of Physical Chemistry Letters* **5**, 2488–2492 (2014).
- [47] Miyata, K. *et al.* Large Polarons in Lead Halide Perovskites. *Science Advances* under review (2017).
- [48] Lee, W. *et al.* Ultralow thermal conductivity in all-inorganic halide perovskites. *Proceedings of the National Academy of Sciences* **114**, 8693–8697 (2017).
- [49] Nielsen, M. D., Ozolins, V. & Heremans, J. P. Lone pair electrons minimize lattice thermal conductivity. *Energy Environ. Sci.* **6**, 570–578 (2013).
- [50] Morelli, D. T., Jovovic, V. & Heremans, J. P. Intrinsically Minimal Thermal Conductivity in Cubic I-V-VI₂ Semiconductors. *Physical Review Letters* **101**, 035901 (2008).
- [51] Delaire, O. *et al.* Giant anharmonic phonon scattering in PbTe. *Nature Materials* **10**, 614–619 (2011).
- [52] Pei, Y., Wang, H. & Snyder, G. J. Band engineering of thermoelectric materials. *Advanced Materials* **24**, 6125–6135 (2012).
- [53] Zhang, X. & Pei, Y. Manipulation of charge transport in thermoelectrics. *npj Quantum Materials* **2**, 68 (2017).
- [54] Al Rahal Al Orabi, R. *et al.* Band Degeneracy, Low Thermal Conductivity, and High Thermoelectric Figure of Merit in SnTe–CaTe Alloys. *Chemistry of Materials* **28**, 376–384 (2016).
- [55] Gaultois, M. W. *et al.* Perspective: Web-based machine learning models for real-time screening of thermoelectric materials properties. *APL Materials* **4** (2016).
- [56] Gaultois, M. W. *et al.* Data-Driven Review of Thermoelectric Materials: Performance and Resource Considerations. *Chemistry of Materials* **25**, 2911–2920 (2013).
- [57] Murty, B. S. *High-entropy alloys* (Butterworth-Heinemann, 2014).
- [58] Cantor, B., Chang, I. T., Knight, P. & Vincent, A. J. Microstructural development in equiatomic multicomponent alloys. *Materials Science and Engineering A* **375–377**, 213–218 (2004).
- [59] Miracle, D. B. & Senkov, O. N. A critical review of high entropy alloys and related concepts. *Acta Materialia* **122**, 448–511 (2017).
- [60] Mu, S., Pei, Z., Liu, X. & Stocks, G. M. Electronic transport and phonon properties of maximally disordered alloys: From binaries to high-entropy alloys. *Journal of Materials Research* 1–24 (2018).
- [61] Jin, K. *et al.* Tailoring the physical properties of Ni-based single-phase equiatomic alloys by modifying the chemical complexity. *Scientific Reports* **6**, 1–10 (2016).

-
- [62] Zhang, Y., Zuo, T., Cheng, Y. & Liaw, P. K. High-entropy alloys with high saturation magnetization, electrical resistivity, and malleability. *Scientific Reports* **3**, 1–7 (2013).
- [63] Chou, H. P., Chang, Y. S., Chen, S. K. & Yeh, J. W. Microstructure, thermophysical and electrical properties in $\text{Al}_x\text{CoCrFeNi}$ ($0 < x < 2$) high-entropy alloys. *Materials Science and Engineering B: Solid-State Materials for Advanced Technology* **163**, 184–189 (2009).
- [64] Shafeie, S. *et al.* High-entropy alloys as high-temperature thermoelectric materials. *Journal of Applied Physics* **118** (2015).
- [65] Körmann, F., Ikeda, Y., Grabowski, B. & Sluiter, M. H. Phonon broadening in high entropy alloys. *npj Computational Materials* **3**, 1–8 (2017).
- [66] Scherrer, P. Bestimmung der Größe und der inneren Struktur von Kolloidteilchen mittels Röntgenstrahlen. *Nachrichten von der Gesellschaft der Wissenschaften zu Göttingen, Mathematisch-Physikalische Klasse* **1918**, 98–100 (1918).
- [67] Aus, M. J. *et al.* Electrical resistivity of bulk nanocrystalline nickel. *Journal of Applied Physics* **75**, 3632–3634 (1994).
- [68] Craig, P. P., Goldberg, W. I., Kitchens, T. A. & Budnick, J. I. Transport properties at critical points: The resistivity of nickel. *Physical Review Letters* **19**, 1334–1337 (1967).
- [69] Campbell, A. F. & A, I. Electrical resistivity of ferromagnetic nickel and iron based alloys. *Journal of Physics F: Metal Physics* **6**, 849 (1976).
- [70] White, G. K. & Tainsh, R. J. Electron scattering in nickel at low temperatures. *Physical Review Letters* **19**, 165–166 (1967).
- [71] Mooij, J. H. Electrical conduction in concentrated disordered transition metal alloys. *Physica Status Solidi (a)* **17**, 521–530 (1973).
- [72] Hussey, N. E., Takenaka, K. & Takagi, H. Universality of the Mott-Ioffe-Regel limit in metals. *Philosophical Magazine* **84**, 2847–2864 (2004).
- [73] Ciuchi, S., Di Sante, D., Dobrosavljević, V. & Fratini, S. The origin of Mooij correlations in disordered metals. *npj Quantum Materials* **3**, 44 (2018).
- [74] Ledbetter, H. M. & Reed, R. P. Elastic Properties of Metals and Alloys, I. Iron, Nickel, and Iron-Nickel Alloys. *Journal of Physical and Chemical Reference Data* **2**, 531–618 (1973).
- [75] Coutu, L., Chaput, L. & Waeckerle, T. 50.50 FeNi permalloy with Ti and Cr additions for improved hardness and corrosion resistance. *Journal of Magnetism and Magnetic Materials* **215-216**, 237–239 (2000).
- [76] Larsen, L., Roy-Poulsen, H., Roy-Poulsen, N. O., Vistisen, L. & Knudsen, J. M. Order-Disorder Transitions in Iron-Nickel (50%-50%) Alloys from Iron Meteorites as Studied by Mössbauer Spectroscopy. *Physical Review Letters* **48**, 1054–1056 (1982).

Bibliography

- [77] Dubrovinsky, L. *et al.* Body-Centered Cubic Iron-Nickel Alloy in Earth's Core. *Science* **316**, 1880–1883 (2007).
- [78] Van Schilfgaarde, M., Abrikosov, I. A. & Johansson, B. Origin of the invar effect in iron-nickel alloys. *Nature* **400**, 46–49 (1999).
- [79] Swartzendruber, L. J., Rivlin, V. P. & Alcock, C. B. The Fe-Ni (Iron-Nickel) system. *Bulletin of Alloy Phase Diagrams* **2**, 102 (1981).
- [80] Zumsteg, F. C. & Parks, R. D. Electrical resistivity of nickel near the Curie point. *Physical Review Letters* **24**, 520–524 (1970).
- [81] Hatherly, M. *et al.* Spin wave energies and exchange parameters in iron-nickel alloys. *Proceedings of the Physical Society* **84**, 55–62 (1964).
- [82] Abrikosov, I. A. *et al.* Competition between magnetic structures in the Fe rich fcc FeNi alloys. *Physical Review B - Condensed Matter and Materials Physics* **76**, 1–14 (2007).
- [83] Chamberod, A., Laugier, J. & Penisson, J. Electron irradiation effects on Iron-Nickel Invar alloys. *Journal of Magnetism and Magnetic Materials* **10**, 139–144 (1979).
- [84] Farrell, T. & Greig, D. The thermoelectric power of nickel and its alloys. *Journal of Physics C: Solid State Physics* **3**, 138–146 (2001).
- [85] Lovas, A. the Contribution of Chemical Composition and the Phase Relation in the Thermopower of Fe-Ni. In *27th International Colloquium of Advanced Manufacturing and Repair Technologies in Vehicle Industry*, vol. VI, 181–188 (2011).
- [86] Babcsán, N., Leitmeier, D. & Banhart, J. Metal foams—high temperature colloids. *Colloids and Surfaces A: Physicochemical and Engineering Aspects* **261**, 123–130 (2005).
- [87] García-Moreno, F. Commercial applications of metal foams: Their properties and production. *Materials* **9**, 20–24 (2016).
- [88] Baumeister, J., Weise, J. & Dukhan, N. *Metal Foams: Fundamentals and Applications* (DEStech Publications, Inc., Lancaster, Pennsylvania 17602, 2013).
- [89] Davis, J. Aluminum and Aluminum Alloys. *Light Metals and alloys* 66 (2001).
- [90] Babcsán, N., Leitmeier, D. & Degischer, H. P. Foamability of Particle Reinforced Aluminium Melt **34**, 22–29 (2003).
- [91] Ip, S. W., Wang, Y. & Toguri, J. M. Aluminum foam stabilization by solid particles. *Canadian Metallurgical Quarterly* **38**, 81–92 (1999).
- [92] Binks, B. P. Particles as surfactants - Similarities and differences. *Current Opinion in Colloid and Interface Science* **7**, 21–41 (2002).

-
- [93] Al Sadat, W. I. & Archer, L. A. The O₂-assisted Al/CO₂ electrochemical cell: A system for CO₂ capture/conversion and electric power generation. *Science Advances* **2**, e1600968–e1600968 (2016).
- [94] Gibson, L. J. & Ashby, M. F. *Cellular Solids* (Cambridge University Press, Cambridge, 1997).
- [95] Kirkpatrick, S. Percolation and Conduction. *Reviews of Modern Physics* **45**, 574–588 (1973).
- [96] Kim, A., Hasan, M. A., Nahm, S. H. & Cho, S. S. Evaluation of compressive mechanical properties of Al-foams using electrical conductivity. *Composite Structures* **71**, 191–198 (2005).
- [97] Ranut, P. On the effective thermal conductivity of aluminum metal foams: Review and improvement of the available empirical and analytical models. *Applied Thermal Engineering* **101**, 496–524 (2016).
- [98] Cuevas, F. G., Montes, J. M., Cintas, J. & Urban, P. Electrical conductivity and porosity relationship in metal foams. *Journal of Porous Materials* **16**, 675–681 (2009).
- [99] Feng, Y., Zheng, H., Zhu, Z. & Zu, F. The microstructure and electrical conductivity of aluminum alloy foams. *Materials Chemistry and Physics* **78**, 196–201 (2002).
- [100] Kováčik, J. & Simancik, F. Aluminium foam-modulus of elasticity and electrical conductivity according to percolation theory. *Scripta Materialia* **39**, 239–246 (1998).
- [101] Chang, K.-S. & Lemlich, R. A study of the electrical conductivity of foam. *Journal of Colloid and Interface Science* **73**, 224–232 (1980).
- [102] McLachlan, D. S., Blaszkiewicz, M. & Newnham, R. E. Electrical Resistivity of Composites. *Journal of the American Ceramic Society* **73**, 2187–2203 (1990).
- [103] Močko, W. & Kowalewski, Z. L. Mechanical Properties of A359/SiCp Metal Matrix Composites at Wide Range of Strain Rates. *Applied Mechanics and Materials* **82**, 166–171 (2011).
- [104] Cabrini, M. *et al.* Evaluation of corrosion resistance of Al-10Si-Mg alloy obtained by means of Direct Metal Laser Sintering. *Journal of Materials Processing Technology* **231**, 326–335 (2016).
- [105] Inoue, A., Bizen, Y., Kimura, H. M., Masumoto, T. & Sakamoto, M. Compositional range, thermal stability, hardness and electrical resistivity of amorphous alloys in Al-Si (or Ge)-transition metal systems. *Journal of Materials Science* **23**, 3640–3647 (1988).
- [106] Kumar, A., Lal, S. & Kumar, S. Fabrication and characterization of A359/Al₂O₃ metal matrix composite using electromagnetic stir casting method. *Journal of Materials Research and Technology* **2**, 250–254 (2013).

Bibliography

- [107] Nair, S. V., Tien, J. K. & Bates, R. C. SiC-reinforced aluminium metal matrix composites. *International Metals Reviews* **30**, 275–290 (1985).
- [108] Dai, Z., Nawaz, K., Park, Y. G., Bock, J. & Jacobi, A. M. Correcting and extending the Boomsma-Poulikakos effective thermal conductivity model for three-dimensional, fluid-saturated metal foams. *International Communications in Heat and Mass Transfer* **37**, 575–580 (2010).
- [109] Paek, J. W., Kang, B. H., Kim, S. Y. & Hyun, J. M. Effective thermal conductivity and permeability of aluminum foam materials. *International Journal of Thermophysics* **21**, 453–464 (2000).
- [110] Babcsán, N., Meszaros, I. & Hegman, N. Thermal and Electrical Conductivity Measurements on Aluminum Foams. *Materials Science and Engineering Technology* **34**, 391–394 (2003).
- [111] Babcsán, N., Banhart, J. & Leitmeyer, D. Metal Foams – Manufacture and Physics of Foaming. *Wire* 5–15 (2003).
- [112] Babcsan, N. *et al.* ALUHAB — The Superior Aluminium Foam. In *ICAA13 Pittsburgh*, 1005–1010 (Springer International Publishing, Cham, 2012).
- [113] Wang, G., Sathe, M., Mitra, S., Jameson, G. J. & Evans, G. M. Detachment of a bubble anchored to a vertical cylindrical surface in quiescent liquid and grid generated turbulence. *Canadian Journal of Chemical Engineering* **92**, 2067–2077 (2014).
- [114] Rossing, T. D. *Handbook of Acoustics*, vol. 77 (2009).
- [115] Kuttruff, H. *Acoustics : an introduction* (Taylor & Francis, 2007).
- [116] Poirier, D. R. & Geiger, G. H. *Transport phenomena in materials processing* (Minerals, Metals & Materials Society, Warrendale, 1994).
- [117] Babcsán, N. Unpublished data courtesy of N. Babcsán (2017).
- [118] Patterson, A. L. The scherrer formula for X-ray particle size determination. *Physical Review* **56**, 978–982 (1939).
- [119] Pawlek, F. & Rogalla, D. The electrical resistivity of silver, copper, aluminium, and zinc as a function of purity in the range 4-298° K. *Cryogenics* **6**, 14–20 (1966).
- [120] Chevrier, J., Pavuna, D. & Cyrot-Lackmann, F. Electronic properties and superconductivity of rapidly quenched Al-Si alloys. *Physical Review B* **36**, 9115–9121 (1987).
- [121] Woodcraft, A. L. Recommended values for the thermal conductivity of aluminium of different purities in the cryogenic to room temperature range, and a comparison with copper. *Cryogenics* **45**, 626–636 (2005).

-
- [122] White, G. & Woods, S. The lattice thermal conductivity of dilute copper alloys at low temperatures. *The London, Edinburgh, and Dublin Philosophical Magazine and Journal of Science* **45**, 1343–1345 (1954).
- [123] Klemens, P. G. & Williams, R. K. Thermal conductivity of metals and alloys. *International Metals Reviews* **31**, 197–215 (1986).
- [124] Gripshover, R. J., VanZytveld, J. B. & Bass, J. Thermopower of Pure Aluminum. *Physical Review* **163**, 598–603 (1967).
- [125] Kittel, C. *Introduction to Solid State Physics* (Wiley, New Caldonia, 2005), 8th edn.
- [126] Tan, X. J. *et al.* Acoustic phonon softening and reduced thermal conductivity in Mg₂Si_{1-x}Sn_x solid solutions. *Applied Physics Letters* **110**, 143903 (2017).
- [127] Xie, W. *et al.* Recent Advances in Nanostructured Thermoelectric Half-Heusler Compounds. *Nanomaterials* **2**, 379–412 (2012).
- [128] U.S. Geological Survey. Mineral Commodities Summaries 2017. Tech. Rep. (2017). arXiv:1011.1669v3.
- [129] Chen, X. & Mao, S. S. Titanium Dioxide Nanomaterials: Synthesis, Properties, Modifications, and Applications. *Chemical Reviews* **107**, 2891–2959 (2007).
- [130] Szirmai, P. *et al.* Cyan titania nanowires: Spectroscopic study of the origin of the self-doping enhanced photocatalytic activity. *Catalysis Today* **284**, 52–58 (2017).
- [131] Heidenau, F. *et al.* A novel antibacterial titania coating: Metal ion toxicity and in vitro surface colonization. *Journal of Materials Science: Materials in Medicine* **16**, 883–888 (2005).
- [132] Pavlovic, M. *et al.* Dendrimer-Stabilized Titanate Nanowire Dispersions as Potential Nanocarriers. *The Journal of Physical Chemistry C* **119**, 24919–24926 (2015).
- [133] Kamegawa, T., Shimizu, Y. & Yamashita, H. Superhydrophobic Surfaces with Photocatalytic Self-Cleaning Properties by Nanocomposite Coating of TiO₂ and Polytetrafluoroethylene. *Advanced Materials* **24**, 3697–3700 (2012).
- [134] Horváth, E., Szilágyi, I., Forró, L. & Magrez, A. Probing titanate nanowire surface acidity through methylene blue adsorption in colloidal suspension and on thin films. *Journal of Colloid and Interface Science* **416**, 190–197 (2014).
- [135] Tétreault, N. *et al.* High-Efficiency Solid-State Dye-Sensitized Solar Cells: Fast Charge Extraction through Self-Assembled 3D Fibrous Network of Crystalline TiO₂ Nanowires. *ACS Nano* **4**, 7644–7650 (2010).
- [136] Jaćimović, J. *et al.* Low temperature resistivity, thermoelectricity, and power factor of Nb doped anatase TiO₂. *Applied Physics Letters* **102**, 013901 (2013).

Bibliography

- [137] Horváth, E., Ribič, P. R., Hashemi, E., Forró, L. & Magrez, A. Dye metachromasy on titanate nanowires: sensing humidity with reversible molecular dimerization. *Journal of Materials Chemistry* **22**, 8778 (2012).
- [138] Byrne, M. T. *et al.* Chemical functionalisation of titania nanotubes and their utilisation for the fabrication of reinforced polystyrene composites. *Journal of Materials Chemistry* **17**, 2351 (2007).
- [139] Yang, J. J. *et al.* Memristive switching mechanism for metal/oxide/metal nanodevices. *Nature Nanotechnology* **3**, 429–433 (2008).
- [140] Moser, S. *et al.* Tunable Polaronic Conduction in Anatase TiO₂. *Physical Review Letters* **110**, 196403 (2013).
- [141] Jaćimović, J. *et al.* From nanotubes to single crystals: Co doped TiO₂. *APL Materials* **1**, 032111 (2013).
- [142] Sekiya, T. *et al.* Defects in Anatase TiO₂ Single Crystal Controlled by Heat Treatments. *Journal of the Physical Society of Japan* **73**, 703–710 (2004).
- [143] Jaćimović, J. *et al.* High-Pressure Study of Anatase TiO₂. *Materials* **3**, 1509–1514 (2010).
- [144] Jaćimović, J. *et al.* Pressure dependence of the large-polaron transport in anatase TiO₂ single crystals. *EPL (Europhysics Letters)* **99**, 57005 (2012).
- [145] Tóth, S. *et al.* Stability and electronic properties of magnetic peapods. *Physica Status Solidi (B) Basic Research* **245**, 2034–2037 (2008).
- [146] Konarev, D. V. *et al.* Supramolecular Approach to the Synthesis of [60]Fullerene-Metal Dithiocarbamate Complexes, {(MII(R₂dtc)₂)_x·L}·C₆₀ (M = Zn, Cd, Hg, Fe, and Mn; x = 1 and 2). The Study of Magnetic Properties and Photoconductivity. *Crystal Growth & Design* **8**, 1161–1172 (2008).
- [147] Szirmai, P. *et al.* Observation of conduction electron spin resonance in boron-doped diamond. *Physical Review B - Condensed Matter and Materials Physics* **87**, 1–5 (2013).
- [148] Zuo, F. *et al.* Self-Doped Ti³⁺ Enhanced Photocatalyst for Hydrogen Production under Visible Light. *Journal of the American Chemical Society* **132**, 11856–11857 (2010).
- [149] Rajh, T., Ostafin, A. E., Micic, O. I., Tiede, D. M. & Thurnauer, M. C. Surface Modification of Small Particle TiO₂ Colloids with Cysteine for Enhanced Photochemical Reduction: An EPR Study. *The Journal of Physical Chemistry* **100**, 4538–4545 (1996).
- [150] Kumar, C. P., Gopal, N. O., Wang, T. C., Wong, M. S. & Ke, S. C. EPR investigation of TiO₂ nanoparticles with temperature-dependent properties. *Journal of Physical Chemistry B* **110**, 5223–5229 (2006).

- [151] Chiesa, M., Paganini, M. C., Livraghi, S. & Giamello, E. Charge trapping in TiO₂ polymorphs as seen by Electron Paramagnetic Resonance spectroscopy. *Physical Chemistry Chemical Physics* **15**, 9435 (2013).
- [152] Livraghi, S., Chiesa, M., Paganini, M. C. & Giamello, E. On the nature of reduced states in titanium dioxide as monitored by electron paramagnetic resonance. I: The anatase case. *Journal of Physical Chemistry C* **115**, 25413–25421 (2011).
- [153] Jaćimović, J. *et al.* Enhanced low-temperature thermoelectrical properties of BiTeCl grown by topotactic method. *Scripta Materialia* **76**, 69–72 (2014).
- [154] Shojaei, E. & Mohammadizadeh, M. R. First-principles elastic and thermal properties of TiO₂: a phonon approach. *Journal of Physics: Condensed Matter* **22**, 015401 (2010).
- [155] Polanco, C. A. & Lindsay, L. Thermal conductivity of InN with point defects from first principles. *Physical Review B* **98**, 014306 (2018).
- [156] Stern, R., Wang, T., Carrete, J., Mingo, N. & Madsen, G. K. Influence of point defects on the thermal conductivity in FeSi. *Physical Review B* **97**, 1–6 (2018).
- [157] Katre, A., Carrete, J., Dongre, B., Madsen, G. K. & Mingo, N. Exceptionally Strong Phonon Scattering by B Substitution in Cubic SiC. *Physical Review Letters* **119**, 1–6 (2017).
- [158] Katcho, N. A., Carrete, J., Li, W. & Mingo, N. Effect of nitrogen and vacancy defects on the thermal conductivity of diamond: An *ab initio* Green's function approach. *Physical Review B* **90**, 094117 (2014).
- [159] Asahi, R., Taga, Y., Mannstadt, W. & Freeman, A. J. Electronic and optical properties of anatase TiO₂. *Physical Review B* **61**, 7459–7465 (2000).
- [160] Landmann, M., Rauls, E. & Schmidt, W. G. The electronic structure and optical response of rutile, anatase and brookite TiO₂. *Journal of Physics: Condensed Matter* **24**, 195503 (2012).
- [161] Gonzalez, R. J., Zallen, R. & Berger, H. Infrared reflectivity and lattice fundamentals in anatase TiO₂. *Physical Review B* **55**, 7014–7017 (1997).
- [162] Mahan, G. D. *Many-Particle Physics* (Springer US, Boston, MA, 2000).
- [163] Setvin, M. *et al.* Direct view at excess electrons in TiO₂ rutile and anatase. *Physical Review Letters* **113**, 086402 (2014).
- [164] Baldini, E. *et al.* Strongly bound excitons in anatase TiO₂ single crystals and nanoparticles. *Nature Communications* **8**, 13 (2017).
- [165] Henderson, M. A. & Lyubinetsky, I. Molecular-level insights into photocatalysis from scanning probe microscopy studies on TiO₂(110). *Chemical Reviews* **113**, 4428–4455 (2013).

Bibliography

- [166] Pang, C. L., Lindsay, R. & Thornton, G. Structure of clean and adsorbate-covered single-crystal rutile TiO₂ surfaces. *Chemical Reviews* **113**, 3887–3948 (2013).
- [167] De Angelis, F., Di Valentin, C., Fantacci, S., Vittadini, A. & Selloni, A. Theoretical studies on anatase and less common TiO₂ phases: Bulk, surfaces, and nanomaterials. *Chemical Reviews* **114**, 9708–9753 (2014).
- [168] Mattioli, G., Alippi, P., Filippone, F., Caminiti, R. & Amore Bonapasta, A. Deep versus shallow behavior of intrinsic defects in rutile and anatase TiO₂ polymorphs. *Journal of Physical Chemistry C* **114**, 21694–21704 (2010).
- [169] Ganduglia-Pirovano, M. V., Hofmann, A. & Sauer, J. Oxygen vacancies in transition metal and rare earth oxides: Current state of understanding and remaining challenges. *Surface Science Reports* **62**, 219–270 (2007).
- [170] Di Valentin, C. & Selloni, A. Bulk and surface polarons in photoexcited anatase TiO₂. *Journal of Physical Chemistry Letters* **2**, 2223–2228 (2011).
- [171] Gerosa, M. *et al.* Defect calculations in semiconductors through a dielectric-dependent hybrid DFT functional: The case of oxygen vacancies in metal oxides. *The Journal of Chemical Physics* **143**, 134702 (2015).
- [172] Moser, S. *et al.* Electron-Phonon Coupling in the Bulk of Anatase TiO₂ Measured by Resonant Inelastic X-Ray Spectroscopy. *Physical Review Letters* **115**, 096404 (2015).
- [173] Finazzi, E., Di Valentin, C., Pacchioni, G. & Selloni, A. Excess electron states in reduced bulk anatase TiO₂: Comparison of standard GGA, GGA+U, and hybrid DFT calculations. *Journal of Chemical Physics* **129** (2008).
- [174] Mattioli, G., Filippone, F., Alippi, P. & Amore Bonapasta, A. Ab initio study of the electronic states induced by oxygen vacancies in rutile and anatase TiO₂. *Physical Review B* **78**, 241201 (2008).
- [175] Barišić, O. S. & Barišić, S. Phase diagram of the Holstein polaron in one dimension. *The European Physical Journal B* **64**, 1–18 (2008).
- [176] Tang, H., Berger, H., Schmid, P. E., Lévy, F. & Burri, G. Photoluminescence in TiO₂ anatase single crystals. *Solid State Communications* **87**, 847–850 (1993).
- [177] Joshi, Y. P. Resonant Scattering of Phonons by Two-Level Impurities. *physica status solidi (b)* **65**, 823–831 (1974).
- [178] Kwok, P. C. Acoustic Attenuation by Neutral Donor Impurity Atoms in Germanium. *Physical Review* **149**, 666–674 (1966).
- [179] Wagner, M. Influence of Localized Modes on Thermal Conductivity. *Physical Review* **131**, 1443–1455 (1963).

- [180] Langenberg, E. *et al.* Analysis of the temperature dependence of the thermal conductivity of insulating single crystal oxides. *APL Materials* **4**, 104815 (2016).
- [181] Di Valentin, C., Pacchioni, G. & Selloni, A. Reduced and n-Type Doped TiO₂: Nature of Ti³⁺ Species. *The Journal of Physical Chemistry C* **113**, 20543–20552 (2009).
- [182] Tosoni, S., Lamiet-Garcia, O., Fernandez Hevia, D., Doña, J. M. & Illas, F. Electronic structure of f-doped bulk rutile, anatase, and brookite polymorphs of TiO₂. *Journal of Physical Chemistry C* **116**, 12738–12746 (2012).
- [183] Morgan, B. J., Scanlon, D. O. & Watson, G. W. Small polarons in Nb- and Ta-doped rutile and anatase TiO₂. *Journal of Materials Chemistry* **19**, 5175–5178 (2009).
- [184] Jaćimović, J. *Nature of the charge carriers and conduction mechanism in anatase TiO₂*. Ph.D. thesis, Ecole Polytechnique Fédérale de Lausanne (2012).
- [185] Lu, X. *et al.* Thermal conductivity of monolithic organic aerogels. *Science (New York, N.Y.)* **255**, 971–2 (1992).
- [186] Allen, P. B. Nanocrystalline Nanowires: 2. Phonons. *Nano Letters* **7**, 11–14 (2007).
- [187] Cahill, D. G. *et al.* Nanoscale thermal transport. II. 2003–2012. *Applied Physics Reviews* **1**, 1–45 (2014).
- [188] Matsuishi, S. *et al.* High-Density Electron Anions in a Nanoporous Single Crystal: [Ca₂₄Al₂₈O₆₄]⁴⁺(4e⁻). *Science* **301**, 626–629 (2003).
- [189] Lacerda, M., Irvine, J. T., Glasser, F. P. & West, A. R. High oxide ion conductivity in Ca₁₂Al₁₄O₃₃ (1988).
- [190] Boysen, H., Lerch, M., Stys, A. & Senyshyn, A. Structure and oxygen mobility in mayenite (Ca₁₂Al₁₄O₃₃): a high-temperature neutron powder diffraction study. *Acta Crystallographica Section B Structural Science* **63**, 675–682 (2007).
- [191] McLeod, J. A. *et al.* Spectroscopic characterization of a multiband complex oxide: Insulating and conducting cement 12CaO•7Al₂O₃. *Physical Review B - Condensed Matter and Materials Physics* **85**, 1–8 (2012).
- [192] Rand, L. P. & Williams, J. D. A calcium aluminate electride hollow cathode. *IEEE Transactions on Plasma Science* **43**, 190–194 (2015).
- [193] Ye, T. N., Li, J., Kitano, M. & Hosono, H. Unique nanocages of 12CaO•7Al₂O₃ boost heterolytic hydrogen activation and selective hydrogenation of heteroarenes over ruthenium catalyst. *Green Chemistry* **19**, 749–756 (2017).
- [194] Toda, Y. *et al.* Rattling of Oxygen Ions in a Sub-Nanometer-Sized Cage Converts Terahertz Radiation to Visible Light. *ACS Nano* **11**, 12358–12364 (2017).

Bibliography

- [195] Sushko, P. V., Shluger, A. L., Hirano, M. & Hosono, H. From insulator to electride: A theoretical model of nanoporous oxide $12\text{CaO}\cdot 7\text{Al}_2\text{O}_3$. *Journal of the American Chemical Society* **129**, 942–951 (2007).
- [196] Kim, S. W. *et al.* Metallic State in a Lime-Alumina Compound with Nanoporous Structure. *Nano Letters* **7**, 1138–1143 (2007).
- [197] Hayashi, K., Matsuishi, S., Kamiya, T., Hirano, M. & Hosono, H. Light-induced conversion of an insulating refractory oxide into a persistent electronic conductor. *Nature* **419**, 462–465 (2002).
- [198] Miyakawa, M. *et al.* Superconductivity in an inorganic electride $12\text{CaO}\cdot 7\text{Al}_2\text{O}_3\cdot e^-$. *Journal of the American Chemical Society* **129**, 7270–7271 (2007).
- [199] Huang, J., Valenzano, L. & Sant, G. Framework and Channel Modifications in Mayenite ($12\text{CaO}\cdot 7\text{Al}_2\text{O}_3$) Nanocages by Cationic Doping. *Chemistry of Materials* **27**, 4731–4741 (2015).
- [200] Bonnickson, K. R. High temperature heat contents of aluminates of calcium and magnesium. *Journal of Physical Chemistry* **59**, 220–221 (1955).
- [201] Feizi, E. & Ray, A. K. High temperature optical absorption investigation into the electronic transitions in sol–gel derived C12A7 thin films. *Journal of Materials Science: Materials in Electronics* **26**, 4691–4697 (2015).
- [202] Kitagawa, J., Ishizaka, M., Kadoya, Y., Matsuishi, S. & Hosono, H. Possible polaron effect in complex terahertz conductivity of electron-doped nanoporous crystal $12\text{CaO}\cdot 7\text{Al}_2\text{O}_3$. *Journal of the Physical Society of Japan* **75**, 1–6 (2006).
- [203] Kim, H. P. *et al.* High-Efficiency, Blue, Green, and Near-Infrared Light-Emitting Diodes Based on Triple Cation Perovskite. *Advanced Optical Materials* 1600920 (2017).
- [204] NREL. NREL Research Cell Efficiency Record (2015). URL <https://www.nrel.gov/pv/assets/pdfs/pv-efficiencies-07-17-2018.pdf>.
- [205] Snaith, H. J. & Hacke, P. Enabling reliability assessments of pre-commercial perovskite photovoltaics with lessons learned from industrial standards. *Nature Energy* **3**, 459–465 (2018).
- [206] Kojima, A., Teshima, K., Shirai, Y. & Miyasaka, T. Organometal Halide Perovskites as Visible-Light Sensitizers for Photovoltaic Cells. *Journal of the American Chemical Society* **131**, 6050–6051 (2009).
- [207] Wells, H. L. Über die Cäsium- und Kalium-Bleihalogenide. *Zeitschrift für anorganische Chemie* **3**, 195–210 (1893).
- [208] Eames, C. *et al.* Ionic transport in hybrid lead iodide perovskite solar cells. *Nature Communications* **6**, 7497 (2015).

- [209] Wangyang, P. *et al.* Recent Advances in Halide Perovskite Photodetectors Based on Different Dimensional Materials. *Advanced Optical Materials* **6**, 1–30 (2018).
- [210] Liu, X., Yu, D., Song, X. & Zeng, H. Metal Halide Perovskites: Synthesis, Ion Migration, and Application in Field-Effect Transistors. *Small* **14**, 1801460 (2018).
- [211] Jiang, P. *et al.* Fully printable perovskite solar cells with highly-conductive, low-temperature, perovskite-compatible carbon electrode. *Carbon* **129**, 830–836 (2018).
- [212] Spina, M. *et al.* Controlled growth of CH₃NH₃PbI₃ nanowires in arrays of open nanofluidic channels. *Scientific Reports* **6**, 19834 (2016).
- [213] Mitzi, D. B. Synthesis, structure, and properties of organic-inorganic perovskites and related materials. In *Progress in Inorganic Chemistry*, vol. 48, 1–121 (Wiley-Blackwell, 2007). URL <http://doi.wiley.com/10.1002/9780470166499.ch1>.
- [214] Zhang, F. *et al.* Brightly Luminescent and Color-Tunable Colloidal CH₃NH₃PbX₃ (X = Br, I, Cl) Quantum Dots: Potential Alternatives for Display Technology. *ACS Nano* **9**, 4533–4542 (2015).
- [215] Arakcheeva, A., Chernyshov, D., Spina, M., Forró, L. & Horváth, E. CH₃NH₃PbI₃: Precise structural consequences of water absorption at ambient conditions. *Acta Crystallographica Section B: Structural Science, Crystal Engineering and Materials* **72**, 716–722 (2016).
- [216] Whitfield, P. S. *et al.* Structures, Phase Transitions and Tricritical Behavior of the Hybrid Perovskite Methyl Ammonium Lead Iodide. *Scientific Reports* **6**, 1–16 (2016).
- [217] Fu, Q. *et al.* Recent Progress on the Long-Term Stability of Perovskite Solar Cells. *Advanced Science* **5** (2018).
- [218] Zheng, F., Saldana-Greco, D., Liu, S. & Rappe, A. M. Material Innovation in Advancing Organometal Halide Perovskite Functionality. *Journal of Physical Chemistry Letters* **6**, 4862–4872 (2015).
- [219] Kim, H., Han, J. S., Choi, J., Kim, S. Y. & Jang, H. W. Halide Perovskites for Applications beyond Photovoltaics. *Small Methods* **2**, 1700310 (2018).
- [220] Spina, M. *et al.* Microengineered CH₃NH₃PbI₃ Nanowire/Graphene Phototransistor for Low-Intensity Light Detection at Room Temperature. *Small* **11**, 4824–4828 (2015).
- [221] Spina, M. *et al.* Photodiode Response in a CH₃NH₃PbI₃/CH₃NH₃SnI₃ Heterojunction. *ACS Applied Materials and Interfaces* **9**, 10198–10202 (2017).
- [222] Tian, W., Zhou, H. & Li, L. Hybrid Organic-Inorganic Perovskite Photodetectors. *Small* **1702107**, 1702107 (2017).

Bibliography

- [223] Andričević, P. *et al.* Three-Dimensionally Enlarged Photoelectrodes by a Protogenetic Inclusion of Vertically Aligned Carbon Nanotubes into $\text{CH}_3\text{NH}_3\text{PbBr}_3$ Single Crystals. *The Journal of Physical Chemistry C* **121**, 13549–13556 (2017).
- [224] Yakunin, S. *et al.* Detection of X-ray photons by solution-processed lead halide perovskites. *Nature Photonics* **9**, 444–449 (2015).
- [225] Wei, H. *et al.* Sensitive X-ray detectors made of methylammonium lead tribromide perovskite single crystals. *Nature Photonics* **10**, 333–339 (2016).
- [226] Andričević, P. *et al.* Light-Emitting Electrochemical Cells of Photovoltaic Perovskite with Vertically Aligned Carbon Nanotubes Contacts. *Submitted* (2018).
- [227] Xing, G. *et al.* Low-temperature solution-processed wavelength-tunable perovskites for lasing. *Nature Materials* **13**, 476–480 (2014).
- [228] Jin, M. L. *et al.* Superconductivity Bordering Rashba Type Topological Transition. *Scientific Reports* **7**, 39699 (2017).
- [229] Zhang, X. *et al.* Promising Thermoelectric $\text{Ag}(\text{5-d})\text{Te}_3$ with Intrinsic Low Lattice Thermal Conductivity. *ACS Energy Letters* **2**, 2470–2477 (2017).
- [230] Mettan, X. *et al.* Tuning of the Thermoelectric Figure of Merit of $\text{CH}_3\text{NH}_3\text{MI}_3$ ($\text{M}=\text{Pb}, \text{Sn}$) Photovoltaic Perovskites. *The Journal of Physical Chemistry C* **119**, 11506–11510 (2015).
- [231] Pisoni, A. *et al.* Metallicity and conductivity crossover in white light illuminated $\text{CH}_3\text{NH}_3\text{PbI}_3$ perovskite 1–18 (2016).
- [232] Takahashi, Y. *et al.* Charge-transport in tin-iodide perovskite $\text{CH}_3\text{NH}_3\text{SnI}_3$: origin of high conductivity. *Dalton transactions (Cambridge, England : 2003)* **40**, 5563–5568 (2011).
- [233] Stoumpos, C. C., Malliakas, C. D. & Kanatzidis, M. G. Semiconducting tin and lead iodide perovskites with organic cations: Phase transitions, high mobilities, and near-infrared photoluminescent properties. *Inorganic Chemistry* **52**, 9019–9038 (2013).
- [234] Takahashi, Y., Hasegawa, H., Takahashi, Y. & Inabe, T. Hall mobility in tin iodide perovskite $\text{CH}_3\text{NH}_3\text{SnI}_3$: Evidence for a doped semiconductor. *Journal of Solid State Chemistry* **205**, 39–43 (2013).
- [235] Pantelides, S. The electronic structure of impurities and other point defects in semiconductors. *Reviews of Modern Physics* **50**, 797–858 (1978).
- [236] Hao, F., Stoumpos, C. C., Cao, D. H., Chang, R. P. H. & Kanatzidis, M. G. Lead-free solid-state organic–inorganic halide perovskite solar cells. *Nature Photonics* **8**, 489–494 (2014).

- [237] Staub, F. *et al.* Beyond Bulk Lifetimes: Insights into Lead Halide Perovskite Films from Time-Resolved Photoluminescence. *Physical Review Applied* **6**, 044017 (2016).
- [238] Caddeo, C. *et al.* Tuning the thermal conductivity of methylammonium lead halide by the molecular substructure. *Physical Chemistry Chemical Physics* **18**, 24318–24324 (2016).
- [239] Whalley, L. D., Skelton, J. M., Frost, J. M. & Walsh, A. Phonon anharmonicity, lifetimes, and thermal transport in CH₃NH₃PbI₃ from many-body perturbation theory. *Physical Review B* **94**, 1–5 (2016).
- [240] Chen, T. *et al.* Rotational dynamics of organic cations in the CH₃NH₃PbI₃ perovskite. *Phys. Chem. Chem. Phys.* **17**, 31278–31286 (2015).
- [241] Leguy, A. M. A. *et al.* The dynamics of methylammonium ions in hybrid organic–inorganic perovskite solar cells. *Nature Communications* **6**, 7124 (2015).
- [242] Wang, M. & Lin, S. Anisotropic and Ultralow Phonon Thermal Transport in Organic–Inorganic Hybrid Perovskites: Atomistic Insights into Solar Cell Thermal Management and Thermoelectric Energy Conversion Efficiency. *Advanced Functional Materials* **26**, 5297–5306 (2016).
- [243] Miyata, K., Atallah, T. L. & Zhu, X.-Y. Lead halide perovskites: Crystal-liquid duality, phonon glass electron crystals, and large polaron formation. *Science Advances* **3**, e1701469 (2017).
- [244] Wang, Y. *et al.* Cation Dynamics Governed Thermal Properties of Lead Halide Perovskite Nanowires. *Nano Letters* **18**, 2772–2779 (2018).
- [245] Heiderhoff, R. *et al.* Thermal Conductivity of Methylammonium Lead Halide Perovskite Single Crystals and Thin Films – A Comparative Study. *The Journal of Physical Chemistry C* **120**, 28472–28479 (2016).
- [246] Yi, H. T., Wu, X., Zhu, X. & Podzorov, V. Intrinsic Charge Transport across Phase Transitions in Hybrid Organo-Inorganic Perovskites. *Advanced Materials* **28**, 6509–6514 (2016).
- [247] Filippetti, A., Caddeo, C., Delugas, P. & Mattoni, A. Appealing Perspectives of Hybrid Lead-Iodide Perovskites as Thermoelectric Materials. *Journal of Physical Chemistry C* **120**, 28472–28479 (2016).
- [248] Lee, C., Hong, J., Stroppa, A., Whangbo, M.-h. & Shim, J. H. Organic–inorganic hybrid perovskites ABX₃ (A = CH₃NH₃, NH₂CHNH₂; B = Sn, Pb) as potential thermoelectric materials: a density functional evaluation. *RSC Adv.* **5**, 78701–78707 (2015).
- [249] Emin, D. Enhanced Seebeck coefficient from carrier-induced vibrational softening. *Physical Review B* **59**, 6205–6210 (1999).

Bibliography

- [250] Devic, T. *et al.* Single crystalline commensurate metallic assemblages of pi-slabs and CdI₂-type layers: synthesis and properties of beta-(EDT-TTF-I₂)₂[Pb_{5/6} square 1/6I₂](3) and beta-(EDT-TTF-I₂)₂[Pb_{2/3}+xAg_{1/3}-2x square xI₂]₃, x = 0.05. *Journal of the American Chemical Society* **125**, 3295–301 (2003).
- [251] Ye, T. *et al.* Ultra-high Seebeck coefficient and low thermal conductivity of a centimeter-sized perovskite single crystal acquired by a modified fast growth method. *Journal of Materials Chemistry C* **5**, 1255–1260 (2017).
- [252] Hasegawa, H., Kobayashi, K., Takahashi, Y., Harada, J. & Inabe, T. Effective Band Gap Tuning by Foreign Metal Doping in Hybrid Tin Iodide Perovskites. *J. Mater. Chem. C* (2017).
- [253] Hasegawa, H. & Inabe, T. Electrical properties of organic-inorganic hybrid tin bromide cubic perovskites: Hole-doping and iodide substitution effects. *New Journal of Chemistry* **40**, 7043–7047 (2016).
- [254] Kraemer, D. & Chen, G. A simple differential steady-state method to measure the thermal conductivity of solid bulk materials with high accuracy A simple differential steady-state method to measure the thermal conductivity of solid bulk materials with high accuracy **025108**, 1–7 (2014).
- [255] Kraemer, D. *et al.* High thermoelectric conversion efficiency of MgAgSb-based material with hot-pressed contacts. *Energy Environ. Sci.* **8**, 1299–1308 (2015).
- [256] Bandiello, E. *et al.* Influence of mobile ions on the electroluminescence characteristics of methylammonium lead iodide perovskite diodes. *J. Mater. Chem. A* **4**, 18614–18620 (2016).
- [257] Frost, J. M. & Walsh, A. What Is Moving in Hybrid Halide Perovskite Solar Cells? *Accounts of Chemical Research* **49**, 528–535 (2016).
- [258] Chen, Y.-F. *et al.* Evidence of band bending induced by hole trapping at MAPbI₃ perovskite/metal interface. *J. Mater. Chem. A* **131**, 6050 (2016).
- [259] Bi, E. *et al.* Diffusion engineering of ions and charge carriers for stable efficient perovskite solar cells. *Nature Communications* **8**, 1–7 (2017).
- [260] Neukirch, A. J. *et al.* Polaron stabilization by cooperative lattice distortion and cation rotations in hybrid perovskite materials. *Nano Letters* **16**, 3809–3816 (2016).
- [261] Bonn, M., Miyata, K., Hendry, E. & Zhu, X.-Y. On the role of dielectric drag in polaron mobility in lead halide perovskites. *ACS Energy Letters* 2555–2562 (2017).
- [262] Wang, J., Wang, L.-L. & Kovnir, K. Phonon glass behavior beyond traditional cage structures: synthesis, crystal and electronic structure, and properties of KMg₄Sb₃. *Journal of Materials Chemistry A* (2018).

-
- [263] Jiang, H. *et al.* Low Temperature Fabrication for High Performance Flexible CsPbI₂ Br Perovskite Solar Cells. *Advanced Science* **1801117**, 1801117 (2018).
- [264] Yan, J., Qiu, W., Wu, G., Heremans, P. & Chen, H. Recent progress in 2D/quasi-2D layered metal halide perovskites for solar cells. *Journal of Materials Chemistry A* **6**, 11063–11077 (2018).
- [265] Leonov, V., Gyselinckx, B. & Hoof, C. Wearable self-powered wireless devices with thermoelectric energy scavengers. In *Integration Issues of Miniaturized Systems - MOMS, MOEMS, ICS and Electronic Components (SSI), 2008 2nd European Conference & Exhibition on*, 1 – 8 (2008). URL http://ieeexplore.ieee.org/xpls/abs/_all.jsp?arnumber=5760521.
- [266] Jin Kim, S. *et al.* High-Performance Flexible Thermoelectric Power Generator Using Laser Multiscanning Lift-Off Process. *ACS Nano* **10**, 10851–10857 (2016).
- [267] Pustovalov, A. Nuclear thermoelectric power units in Russia, USA and European space agency research programs. In *XVI ICT '97. Proceedings ICT'97. 16th International Conference on Thermoelectrics (Cat. No.97TH8291)*, 559–562 (IEEE, 1997). URL http://ieeexplore.ieee.org/xpl/freeabs/_all.jsp?arnumber=667591<http://ieeexplore.ieee.org/document/667591/>.
- [268] Altenkirch, E. Über den Nutzeffekt der Thermosäule. *Physikalische Zeitschrift* **10**, 560–568 (1909).
- [269] Kim, H. S., Liu, W., Chen, G., Chu, C.-W. & Ren, Z. Relationship between thermoelectric figure of merit and energy conversion efficiency. *Proceedings of the National Academy of Sciences* **112**, 8205–8210 (2015).
- [270] Kaptay, G. The chemical (not mechanical) paradigm of thermodynamics of colloid and interface science. *Advances in Colloid and Interface Science* **256**, 163–192 (2018).

Xavier METTAN

+4179 265 27 04
xavier.mettan@epfl.ch

Route Neuve 85
CH-1024 Ecublens

07.01.1990
Swiss/French



Education

- **Swiss Federal Institute of Technology (EPFL), Lausanne, CH**
 - └ PhD at the Laboratory of Physics of Complex Matter (Prof. László Forró), 10/2014 - 03/2019
 - └ Master of Science in Applied Physics (solid-state and statistical physics) 09/2012 - 08/2014
 - └ Bachelor of Science in Physics 09/2009 - 07/2012
- **Humboldt Universität, Berlin, DE** Erasmus exchange year 08/2011 - 07/2012
- **Lycée-Collège de la Planta, Sion, CH** High school diploma, scientific option 08/2005 - 06/2009

Work experiences

- **Laboratory of Complex Matter Physics (LPMC), EPFL, CH** PhD 10/2014 - 03/2019
 - └ Exploration of the thermal and electronic properties of complex materials: Discovery and modelling of a new mechanism reducing the thermal conductivity of anatase TiO_2 . Investigations on the role of structural disorder on the thermal and electronic transport (aluminum foam, high-entropy alloys). Design and assembly of experimental setups and implementation of corresponding softwares.
 - └ Initiation and supervision of the negotiations for the acquisition of scientific equipment (> 80 kCHF). Definition and tutoring of undergraduate students' projects; teaching physics to (> 500) medicine students. Communication of scientific achievements (posters, talks, publications) to international audiences.
- **Oxide Molecular Beam Epitaxy Group, BNL, NY, USA** Master Thesis 02/2014 - 08/2014
 - └ Chemical cleaning of adsorbates on the surface of LaAlO_3 and Al_2O_3 atomically-smooth surfaces. Establishment of a thermal treatment leading to perfectly smooth terraces on sapphire substrates.
 - └ Synthesis of epitaxial lead iodide thin-films by thermal evaporation.
- **NTN-SNR Bearings, R&D department, Annecy, FR** Internship 07/2013 - 02/2014
 - └ Development of a novel absolute-angle-measurement technology: Implementation of an algorithm generating position-encoding patterns, simulation of the magnetic fields (IES Amperes) near the magnetic encoders, bench-tests and prototyping of magnetic encoders.
 - └ Improvement of the accuracy (< 50 μm) of a linear-positioning system.

Skills

- **Materials synthesis** Thermal evaporation, sputtering, sintering.
- **Materials characterisation** Ultra-low current and voltage DC/AC measurements, ultra-high vacuum techniques, electronic packaging, atomic-force microscopy (AFM), scanning-electron microscopy (SEM), energy-dispersive X-ray spectroscopy (EDX), X-ray diffraction.
- **Cleanroom processes** Layout preparation, Ebeam- and photo- lithography, dry and wet etching.
- **IT - Modelling, control and automation** Matlab, NI LabView, C++, Python
- **IT - CAD and graphic design** SolidWorks, Scribus, Inkscape, Blender

Volunteering and awards

- Head of fundraising for the EPFL Students Chamber Orchestra (OChE) (08/2014-09/2017)
- *EES* Poster Prize, 1st Internat. Conf. on Perovskite Solar Cells & Optoelectronics, Lausanne, CH (09/2015)
- Winning team of the International Physicist Tournament (IPT) 2013, Lausanne, CH (04/2013)

Interests

- Leading the 2nd violin section in EPFL Orchestra (OChE)
- Tasting wines from the World
- Hiking around Lake Geneva and across the Swiss Alps

Languages

- English: C1 European level
- German: B2 European level
- French: mother language

List of publications

- > Csaba Forró, Xavier Mettan and Thibaud Humair, Spectral color or how to turn green laser light red, *Eur. J. Phys.*, **35** (6), 064004 (2014).
- > Jaćim Jaćimović, Xavier Mettan, Andrea Pisoni, Richar Gaál, Sergiy Katrych, László Demko, Ana Akrap, László Forró, Helmuth Berger, Philippe Bugnon and Arnaud Magrez, Enhanced low-temperature thermoelectrical properties of BiTeCl grown by topotactic method, *Scripta Materialia*, **76**, 69–72 (2014).
- > Xavier Mettan, Ricardo Pisoni, Péter Matus, Andrea Pisoni, Jaćim Jaćimović, Balint Náfrádi, Massimo Spina, Davor Pavuna, László Forró, and Endre Horváth, Tuning of the Thermoelectric Figure of Merit of $\text{CH}_3\text{NH}_3\text{MI}_3$ (M=Pb,Sn) Photovoltaic Perovskites, *J. Phys. Chem. C*, **119** (21), 11506–11510 (2015).
- > Pavao Andričević, Márton Kollár, Xavier Mettan, Bálint Náfrádi, Andrzej Sienkiewicz, Dóra Fejes, Klara Hernadi, László Forró and Endre Horváth, 3-Dimensionally Enlarged Photoelectrodes by a Protogenetic Inclusion of Vertically Aligned Carbon Nanotubes into $\text{CH}_3\text{NH}_3\text{PbBr}_3$ Single Crystals, *The Journal of Physical Chemistry C*, **121** (25), 13549–13556 (2017).
- > Bálint Náfrádi, Péter Szirmai, Massimo Spina, Andrea Pisoni, Xavier Mettan, Norbert Nemes, László Forró, Endre Horváth, Tuning Ferromagnetism at Room Temperature by Visible Light, *Nature Communications*, *in review*.
- > Xavier Mettan, Jaćim Jaćimović, Andrea Pisoni, Osor S. Barišić, Ivo Batistić, Endre Horváth, Samuel Brown, Lidia Rossi, Péter Szirmai, Helmuth Berger, and László Forró, Tailoring thermal conductivity of anatase TiO_2 : from bulk crystals to foams, *in preparation*.
- > Sergiy Katrych, Xavier Mettan, Flavio M. Mor, Andrea Pisoni, Andrzej Sienkiewicz, Richard Gaal, Alla Arakcheeva, Arnaud Magrez, Ivica Zivkovic, Ayat Karimi, Balint Nafradi, Zsolt Revay, Sylvia Jeney, Janusz A. Karpinski and László Forró, Structure and properties of $\text{Ln}_7\text{O}_4(\text{BO}_3)_4$ (Ln=Pr,Nd) grown at high pressure, *in preparation*.

Oral presentations

- > “Thermoelectric Figures of Merit of Novel Thermoelectric Materials”, *EMN Meeting on Thermoelectric Materials*, Orlando, USA, 21-25 February 2015 (invited).
- > Presentation “Trends in the research for efficient thermoelectric materials”, *Friday Afternoon Discourse (FAD)*, EPFL Lausanne, 18 March 2016 (invited).
- > “Perspectives on new thermoelectric materials”, *Swiss-Hungarian science workshop*, EPFL Lausanne, 4 November 2016 (invited).

- > “Hybrid halide perovskites and thermoelectricity: perspectives”, *3^e Journées des Perovskites Hybrides*, Angers FR, 10 May 2017 (contributed).
- > “Hybrid halide perovskites and thermoelectricity: perspectives”, *AMBER-EPFL joint workshop*, Trinity College Dublin, 26 April 2018 (invited).
- > “Tailoring thermal conductivity of anatase TiO₂: from bulk crystals to foams”, *Swiss Workshop on Materials with Novel Electronic Properties 2018*, Les Diablerets, 31 August 2018 (contributed).

Poster presentations

- > “Tuning of the Thermoelectric Figure of Merit of CH₃NH₃MI₃ (M=Pb,Sn) Photovoltaic Perovskites”, *1st International Conference on Perovskite Solar Cells and Optoelectronics (PSCO)*, Lausanne, 27–29 September 2015. Award of RSC *Energy & Environmental Science* for the best poster.
- > “Tuning of the Thermoelectric Figure of Merit of CH₃NH₃MI₃ (M=Pb,Sn) Photovoltaic Perovskites” *MaNEP Swiss Workshop on Materials with Novel Electronic Properties*, Les Diablerets, 6–8 July 2016.
- > “Thermoelectric properties of hybrid halide perovskites”, *International Research School: Electronic States and Phases Induced by Electric or Optical Impacts IMPACT 2016*, Cargèse FR, 23 August – 2 September 2016.
- > “Thermoelectric properties of hybrid halide perovskites”, *Physics Day EPFL*, EPFL Lausanne, 16 October 2017.
- > “Thermoelectric properties of hybrid halide perovskites”, *International Conference on Hybrid and Organic Photovoltaics (HOPV) 2017*, Lausanne, 21–24 May 2017.

